Design and Implementation of the Real-Time Control System for an Open Trapped Ion Quantum Computing Platform

by

Collin Joseph Cunningham Epstein

A thesis
presented to the University of Waterloo
in fulfillment of the
thesis requirement for the degree of
Master of Science
in
Physics (Quantum Information)

Waterloo, Ontario, Canada, 2023

Author's Declaration

I hereby declare that I am the sole author of this thesis. This is a true copy of the thesis, including any required final revisions, as accepted by my examiners.

I understand that my thesis may be made electronically available to the public.

Abstract

Trapped atomic ions are a promising platform for the implementation of quantum bits and quantum information processors due to advantageous inherent physical properties as well as exquisite experimental control. Trapped ion quantum computers are composed of many independent systems which must be controlled and coordinated with sub-microsecond time resolution to perform quantum operations. This thesis describes the design and construction of the electrical infrastructure and real-time control hardware and software for an open source, open access trapped ion quantum computing platform. It presents the physical requirements for the trapped ion quantum information processor, how those requirements translate into design specifications for the electrical and control systems, and the progress on assembling and integrating those systems into an operational ion trap apparatus.

Acknowledgements

A scientific and engineering enterprise on the scale of a quantum computer requires the steadfast efforts of many people in many ways. This work is deeply indebted to the labor of others, to whom I am sincerely grateful.

Thank you to my supervisor, Dr. Crystal Senko, for inviting me into this exciting project. Her guidance and patience as I come up to speed on a vast work-in-progress is unending and remarkable. I am particularly grateful for her support during a difficult transition back to school.

Additional thanks to Dr. Rajibul Islam as co-lead of the QuantumIon Project and to Dr. Alan Jamison and Dr. Jonathan Baugh as members of my supervisory committee for keeping me on track. I learn more with every conversation!

I have been fortunate to work with and learn from a wonderful group of collaborators. My thanks to the QuantumIon team of Noah Greenberg, Elijah Durso-Sabina, Ali Binai-Motlagh, Hawking Tan, and Dr. Akbar Jahangiri Jozani with whom I have worked closely. I also appreciate the efforts of previous members of the team: Dr. Matt Day, Dr. Virginia Frey, Dr. Mahmood Sabooni, Rich Rademacher, and Nikolay Videnov.

One of the great privileges of my role in this project has been the opportunity to supervise fabulously talented undergraduate coop students. Great thanks for your contributions to the hardware team: Kelly Lu, Elizabeth Wong, Dean Smith, Jason Gao, Sherry Xiao, Lucy Yandeng, Jacky Lim, Steven Del Grosso Milek, Mark Elliot Wallace, and Johan Alant; and the software team: Samuel Burke, Kevin Chen, Dean Smith, Alex Liu, and Aryan Modgil. They all brought skills and perspectives that I lack and I am grateful to have learned from them and had their help.

My work has been supported in many ways by a fantastic set of collaborators, internal and external. At the University of Waterloo, thank you to the Qudit Lab: Brendan White, Pei Jiang Low, Yvette De Sereville, and Nicholas Zutt; and the QITI Lab: Sainath Motlakunta, Gilbert Shih, Nikhil Kotibhaskar, Lewis Hahn, Monica Zhu, Monica Zhu, and Sakshee Patil for discussions and advice. I also appreciate current collaborators Benjamin McLellan, Yi Hong Teo, Roger Luo, Sasan Vosoogh-Grayli, and Roger Melko, and look forward to continuing our quantum controls collaboration.

Thanks as well to Melissa Revelle, Susan Clark, Jay Van Der Wall, Jon Sterk, Dan Stick, and the rest of the microfabricated ion trap team(s) of Sandia National Laboratories for their support, including provision of the Phoenix trap, advice on its usage, and generously inviting me to dip my toes into this field in the first place. My thanks to Leo Reisebos, Filip

Mazurek, and Brad Bondurant of Duke University for advice on usage of DAX and more generally on building the software infrastructure for a trapped ion quantum computer. Thank you as well to rest of the DAX team for a wonderful tool. I am also grateful to Mateusz Wójcik of M-Labs for helping to stand up our Sinara hardware and ARTIQ control system.

I appreciate the deep support that this project and my own education has received from Transformative Quantum Technologies, the Institute for Quantum Computing, and the Department of Physics and Astronomy at the University of Waterloo. My deep, heartfelt thanks to David Cory, Don Carkner, Tarra Webber, Sara Clark, Peter Sprenger, and Alex Mitrovic of TQT for technical and administrative support; Tim Laslavic, Shona Magill, Penny Stumpf, Dalton Scott, Lirong Liu, Trevor Beatson of UW Procurement and Central Stores for helping purchase and track down the truly overwhelming supplies required for our laboratory and apparatus; Matt Cooper and Steve Weiss for IT support; and Chris Dietrich, Michele Roche, and Kayla Sutton for helping me navigate the University and stay on track.

Thank you to the mentors and advisors who got me as far as graduate school in the first place: Dr. Amber Dagel, Kyle Thompson, Dr. Dan Boye, Dr. Tim Gfroerer, and Dr. Tabitha Peck.

Thank you to my parents, Dorothy Cunningham and Larry Epstein, and my brother, Evan Epstein, for their unending support.

And finally, I thank my wife, Hannah Epstein, without whom nothing at all would have been possible.

Dedication

To my wife, Hannah Epstein.

Table of Contents

List of Figures

List of Tables

List of Listings

Chapter 1

Introduction

Quantum computing (QC) is a computing paradigm that leverages some of the more peculiar features of quantum mechanics, such as superposition and entanglement, as resources for performing certain kinds of computational tasks more quickly than *classical computers* [84, 113]. *Quantum computers* were first proposed to accelerate simulation of quantum mechanical systems [41, 69, 73], but have generated more widespread interest in the wake of proofs demonstrating that quantum computation is universal [36], capable of accelerating important non-physics computations such as prime number factorization and calculating discrete logarithms [104] and unstructured search [48], and (in principle) able to overcome operational errors to perform arbitrarily long algorithms [44, 90, 105, 112].

Quantum computers manipulate quantum bits (*qubits*) to perform quantum computation. Qubits are discrete two-level systems, like classical bits, but are implemented on physical systems that exhibit quantum mechanical behavior. Trapped atomic ions are one such system that has harnessed for quantum information processing (QIP) experiments. Ions have natural advantages as qubits, including identical structures and advanced control techniques.

Individual quantum systems are difficult to isolate and control. Even more difficult is the task of scaling up the creation and control of qubits to the numbers required for useful computation tasks. This thesis concerns the development of the electrical infrastructure and control system required to operate a sophisticated trapped ion quantum computer (TIQC).

1.1 The QuantumIon Project

The work for this thesis was done as part of the QuantumIon Project at the Institute for Quantum Computing at the University of Waterloo[1]. Access to high quality quantum hardware is a major limiting factor in current quantum information research. The QuantumIon Project aims to provide an open-source, open-access quantum information processor with 16 trapped ion qubits for the wider academic community. The apparatus will be an exciting research tool that exposes more implementation and experimental detail than currently available quantum platforms. Our goal is for the apparatus to accelerate research at the University of Waterloo and our collaborators while democratizing access to and education about quantum information sciences as a user service center. For more details on the design of the QuantumIon apparatus, see [10, 47, 91, 120].

Our apparatus also demonstrates several important research and technical advances. Specifically, we aim to trap and employ multiple isotopes of barium as qubits in a microfabricated surface ion trap. We are primarily trapping singly-ionized barium-133 ($^{133}Ba^{+}$), which should make an excellent quantum bit because of its optical energy transitions, long-lived metastable states, simple energy level structure, and ability to encode quantum computational basis states in energy levels insensitive to magnetic field noise [24, 25, 52]. Unfortunately, $^{133}Ba^{+}$ is a radioisotope with no natural abundance, which introduces complications in apparatus design, engineering, and assembly. We also target other isotopes of barium ($^{137}Ba^{+}$, $^{138}Ba^{+}$) to support multi-species experiments and architectures.

Microfabricated surface ion traps leverage mature microfabrication technologies to build ion traps that are built more reliably to better tolerances than alternative trap form factors. They are also smaller and can be designed with tiny features such as many individually controllable electrodes for sculpting custom, dynamic confining electric potential wells. We are using a Phoenix surface ion trap developed and delivered by Sandia National Laboratories [93].

Additionally, we are developing a full stack quantum control framework to control our apparatus. Access to high-quality quantum hardware is a limiting factor in QIP research. We aim to improve access my developing a control system that can be operated remotely by users with multiple levels of skill and that can be easily deployed to TIQC prototypes with a variety of capabilities.

In the course of building a cutting-edge apparatus, our group has made additional technical advances. Achievements include development of a flexible individual laser ad-

[1] https://tqt.uwaterloo.ca/project-details/quantumion-an-open-access-quantum-computing-platform/

dressing system [9], robust atomic source preparation [45], improved loading rates using autoionization resonances [46], and a proposal for a novel quantum control language [43].

1.2 Trapped Ion Quantum Computing

Atomic ions are individual ions with one or more electrons added to or removed from the atom, resulting in a particle with net electric charge. The net charge enables the ions to be isolated and trapped in localized regions of space with electromagnetic fields [32, 87]. The properties of the ions can then be probed and its dynamics affected with lasers. Measurements of the light scattered by the ions yields significant information about the ions' behavior [65]. Ion traps have also been used to implement exciting technologies such as atomic clocks [15, 33] and quantum information processor prototypes.

Experiments on trapped ions as a platform for QIP date to the proposal of the first entangling gate on trapped ions proposed by Cirac and Zoller [26], with demonstration of the gate soon following [79]. Mølmer and Sørenson later proposed an entangling gate for ions more robust to thermal noise which has become the standard entangling operation in the field [77, 108, 109]. The entangling gate combined with additional techniques for manipulating the state of individual ions suffice for trapped ions to satisfy the DiVincenzo criteria as a platform for universal quantum computation [39].

The field of TIQC has since blossomed with many demonstrations of ions trapped as rudimentary quantum computers [18, 54, 49, 113, 125] and quantum simulators [11, 80, 127]. Proposals for scaling TIQC up to larger and larger numbers of qubits include the quantum charge-coupled device [60] and photonic interconnect platforms [81]. Compact technologies to fit a TIQC into a standard computing rack have even been demonstrated [89].

1.3 Thesis Overview

TIQCs are complex apparatuses composed of numerous technologies, all working at their cutting edge and coordinated with sub-microsecond precision. Significant electrical infrastructure and sophisticated real-time quantum control systems are required to assemble and operate TIQCs. This thesis describes the electrical control circuits and real-time control system designed and implemented for the QuantumIon Project, building upon previous control system development [91].

The current stage of the QuantumIon Project is focused on integrating optical, electrical, vacuum, and control technologies to trap the first ions in the apparatus. Our first experiments are set up to trap $^{138}Ba^{+}$ so that we can tune the system with a species that has no hyperfine splitting and is not radioactive, simplifying the demands on our technology and safety protocols. Once we successfully trap $^{138}Ba^{+}$, we will proceed to trapping $^{133}Ba^{+}$.

This thesis begins with a review of ion trapping physics in Chapter 2. Chapter 3 describes the electrical components of the apparatus and the circuits required to deliver real-time and non-real-time signals to the correct components. In Chapter 4, we present the quantum control hardware and software systems. Finally, Chapter 5 reviews the remaining work ahead to implement a full TIQC as a user service platform.

Chapter 2

Ion Trapping Physics

This chapter presents the key physics of trapping atomic ions. The physics determines the requirements of the performance of the ion trap, which in turn informs the design decisions for the electrical infrastructure described in Chapter 3 and the control hardware and software detailed in Chapter 4. The discussion will include how ion trapping physics apply to trapping barium ions in the QuantumIon system.

First, we explore the properties of singly-ionized barium-133 ($^{133}Ba^{+}$), the ion species used in this apparatus, in Section 2.1. Section 2.2 discusses methods of producing the ions to be trapped from atomic sources. Section 2.3 explains how charged atomic ions are spatially confined, or trapped, with electric fields. Cooling ions with laser light so the ions can be observed and used in quantum experiments is discussed in Section 2.4. Section 2.5 demonstrates how quantum state preparation and measurement (SPAM) are implemented on trapped atomic ions. Section 2.5.3 explains how the energy level transitions used in laser cooling and SPAM lead to the choice of modulation frequencies for generating laser sidebands to target the necessary transitions. Finally, Section 2.6 concludes with a brief description of quantum gates in trapped ion quantum information processors.

2.1 Barium-133 Ion Qubit

Singly-ionized barium-133 ($^{133}Ba^{+}$) has several advantageous properties that make it an exceptionally promising ion for quantum information processing. These properties are its two valence shell electronics, nuclear spin of $I = 1/2$, long-lived metastable states, and optical wavelength energy level transitions. Together, the aforementioned properties

combine to produce a positive ion with an energy level structure that can be exploited to produce a high-performance qubit [10, 14, 24, 25, 47, 52, 91, 120].

2.1.1 Advantages

Barium is an alkaline earth metal, a category of element that has two valence electrons [1]. When barium is ionized by stripping one of the valence shell electrons away, the result is a *hydrogen-like* ion with a single shell electron (Figures 2.1). The net electric charge of $+e$ allows the ion to be trapped with electric fields (Section 2.3) and the single valence shell electron results in a simple electronic energy level structure compared to atoms and ions with multiple valence electrons. Elements chosen for trapped ion quantum computing experiments, while not all alkaline earth metals, all have this electron shell structure [18, 30, 49, 54, 65, 110].

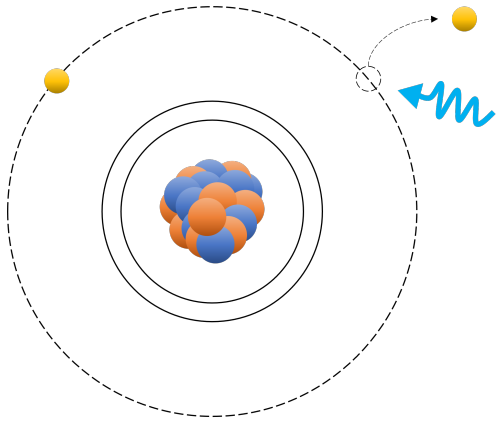

Figure 2.1: Diagram of the photoionization of an atom with two valence shell electrons (not to scale). After one electron is stripped from the atom, the resulting positive ion has one electron in its valence shell.

The nuclear spin of $^{133}Ba^{+}$ is $I = 1/2$, which limits the number of hyperfine states in the ion [14]. The small number of available states makes the energy levels of $^{133}Ba^{+}$ simple to determine and sufficiently distinguishable to target individually during quantum operations [25, 52]. Some of the hyperfine states are degenerate, which introduces the possibility of coherent dark states. Coherent dark states are superpositions of degenerate hyperfine states that eliminate the probability of absorbing photons that would usually drive a transition to another energy level. The ion does not respond to those photons until

it naturally exits the superposition state. We apply a magnetic field to take advantage of Zeeman splitting of the hyperfine states and prevent coherent dark states.

The presence of the long-lived metastable D states enables high-fidelity state preparation and measurement and multiple possible qubit encoding schemes, making $^{133}Ba^{+}$ a flexible isotope suitable for multiple qubit implementations and system architectures [2]. We target the ground, or hyperfine *clock-state* qubit encoding. The computational basis states are encoded in hyperfine energy levels of the ground state $^2S_{1/2}$: $|0\rangle = |F = 0; m_f = 0\rangle$, $|1\rangle = |F = 1; m_f = 0\rangle$ [25, 52]. Since the projection of the total atomic angular momentum along the *quantization axis* quantum number $m_f = 0$ for both states, their energy difference is not coupled to the magnetic field of the environment, making the qubit insensitive to magnetic field noise. Alternatively, a metastable qubit could be encoded between hyperfine levels of the long-lived $^2D_{5/2}$ state, similar to the encoding in hyperfine split of the ground state. Finally, an optical qubit could be encoded between the ground state and the metastable state. Figure 2.2 displays potential optical, metastable, and ground state qubit encoding schemes for $^{133}Ba^{+}$.

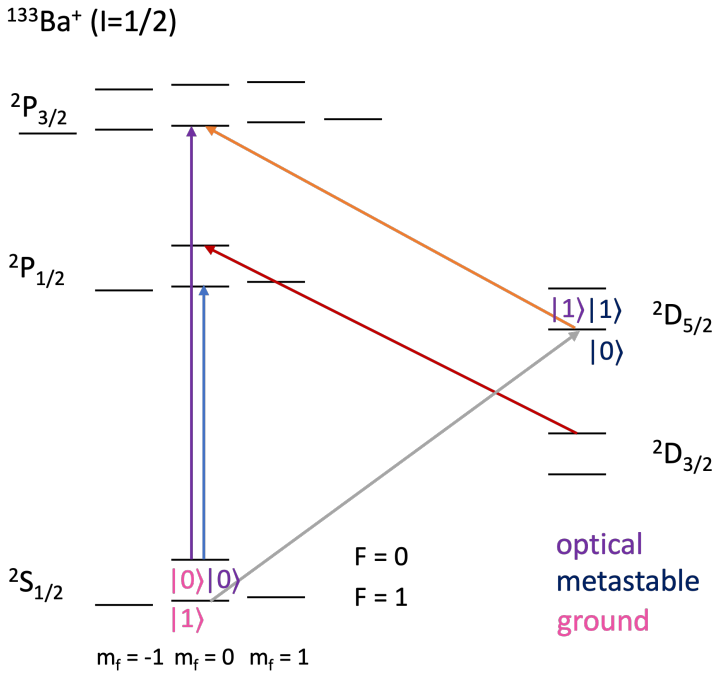

Figure 2.2: Energy level diagram of $^{133}Ba^{+}$ displaying potential encoding schemes for an optical, metastable, or ground state qubit (not to scale).

The energy levels of $^{133}Ba^{+}$ relevant for basic quantum operations are all separated by energies that correspond to visible wavelengths of light (Figure 2.3). Other elements commonly used in quantum information processing that have all have at least one essential transition in the ultraviolet and/or infrared spectra [24, 110]. Using visible light allows us to use to high-performance and commercially-available lasers, free space and fiber optics, and waveguides. Lasers tuned to drive transitions between energy levels are used for cooling the ions (Section 2.4) and state preparation and measurement (Section 2.5), as well as coherent quantum operations beyond the scope of this thesis. The highest fidelity state preparation and measurement of any trapped ion qubit have been demonstrated on $^{133}Ba^{+}$ [25].

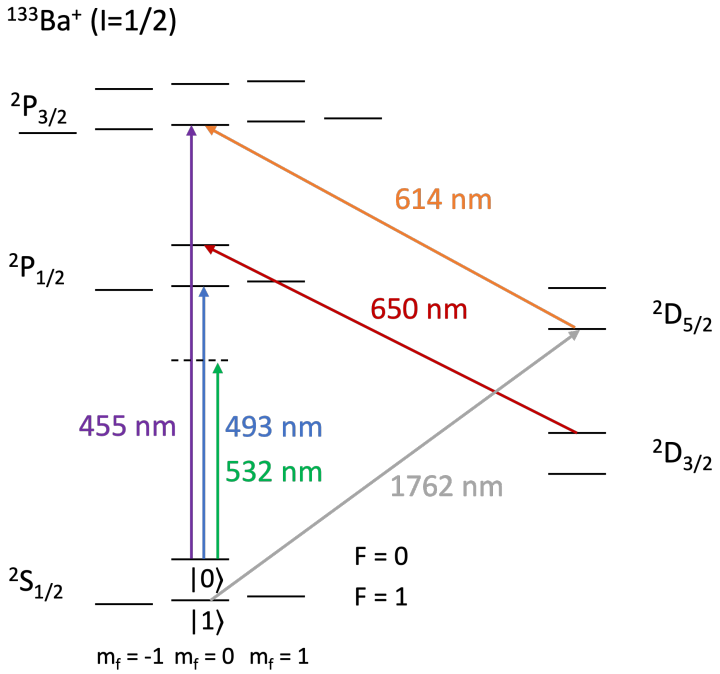

Figure 2.3: Energy level diagram of $^{133}Ba^{+}$ displaying laser wavelengths that drive transitions between the electronic energy levels of the ion [25, 52] (not to scale). Since all of the transitions (except the 1762 nm shelving transition) are in the visible spectrum, apparatuses using $^{133}Ba^{+}$ can take advantage of visible wavelength optics. These transitions make $^{133}Ba^{+}$ the prettiest ion!

Finally, barium has multiple isotopes that make good candidates for qubits. In addition to $^{133}Ba^{+}$, singly-ionized barium-137 ($^{137}Ba^{+}$) and singly-ionized barium-138 ($^{138}Ba^{+}$) are

actively under investigation for use as qubits and, in the case of $^{137}Ba^{+}$, even $d > 2$-level qu$d$its [10, 14, 31, 47, 38, 71, 103, 129]. Multiple isotopes that make good qubits with distinct transition energies but similar masses presents opportunities for implementing larger quantum information processors that leverage advanced techniques such as multi-species encoding [31, 42, 53, 88, 122], and sympathetic cooling [59, 63, 128].

2.1.2 Disadvantages

Unfortunately, $^{133}Ba^{+}$ has a minor downside as a qubit. It is an entirely synthetic radioactive isotope with a half-life of $\tau = 10.5$ years [25, 52]. The radiation emitted from $^{133}Ba^{+}$ introduces some difficulty in procurement and atomic source preparation and requires our lab to implement radiation safety and protection protocols. The primary design consequences are the decisions to minimize the total amount of $^{133}Ba^{+}$ in our atomic source and to remotely control as much of the system as possible.

The disadvantages of $^{133}Ba^{+}$ are straightforward to overcome. We procure $^{133}Ba^{+}$ as a $BaCl_2$ salt in solution [24, 31, 25, 52, 103] and prepare atomic source targets ourselves (Section 2.2.3). Remote operation is reasonably simple to implement and aligns with the design goal of a high-up-time, remotely-operable user center and platform as discussed in Section 1.1. Radiation protection is achieved by minimizing the amount of $^{133}Ba^{+}$ in the apparatus to ≤ 0.5 mCi (microgram quantities), installing extensive lead shielding around the vacuum chamber, and radiation monitoring and dosimetry. Thus, the benefits of using $^{133}Ba^{+}$ to implement a qubit in a trapped ion system far outweigh the risks.

2.2 Ion Production

Gaseous ions must be present in the trapping region in order for them to be trapped by the apparatus. The procedure is to produce a vapor of ions from a reservoir of solid material. Traditionally, ion production is accomplished by heating a bulk metal sample of the desired element in an oven until neutral atoms are emitted [100]. The atoms are then photoionized with laser beams. A subset of the newly produced ions are captured in a trapping potential (discussed in Section 2.3), while the remaining ions and neutral atoms are pumped out of the chamber (discussed in Section 3.5).

Use of a radioactive ion such as $^{133}Ba^{+}$ dictates that a minimal amount of the radioactive material be present in the sample (Section 2.1.2). The minimal material requirement renders the fabrication and use of ovens difficult [99, 101]. Additionally, ovens are highly

inefficient in terms of the ratio of atoms liberated from the sample to ions actually trapped, which is not ideal for our small amount of material. Instead, we implement laser ablation in the QuantumIon apparatus.

2.2.1 Laser Ablation

Laser ablation produces ions from a solid material by blasting the material with a powerful laser which creates a plasma plume [123]. The plume contains a variety of particles, including neutral and ionized atoms and molecules, depending on the composition of the target material and intensity of the ablating laser. The plume of fast-moving particles then propagates through space into the region where they may be trapped.

Laser ablation is a more efficient process of generating ions than oven heating. It produces less material in a more localized region, which is advantageous for efficient use of our small $^{133}Ba^{+}$ source. Laser ablation also enables greater control over the experiment. We can produce atom plumes on-demand with precise timing control by triggering the ablation laser, compared to the bulk atom production ovens achieve when slowly heating and cooling. Additional loading techniques, such as direct ion loading, are available by modifying the intensity of the ablation laser.

Unfortunately, laser ablation produces particles of any type that is present in the atomic source. Therefore, we favor techniques that enable selective ionization of only the specific ion species we wish to trap.

Direct Ionization

Laser ablation produces a mixture of forms of the materials present in a sample. The ratio of neutral vs. ionized atoms and molecules depends on the intensity of the ablation laser. At low laser intensity, mostly neutral atoms are produced. Above a certain power threshold, ablation produces mostly ions and less neutral atoms [123]. The produced ions may then be trapped without requiring a photoionization step (Section 2.3.4).

Direct ionization is not preferred because it is not an isotope-selective loading technique and the production of excessive charged particles in the vacuum chamber may lead to electrical charging of the trap, reducing trap performance [47].

2.2.2 Photoionization

Any neutral atoms produced during ablation may be photoionized by shining lasers of certain wavelengths on the neutral atoms [35]. One or more photons are absorbed, exciting a valence electron with at least the ionization energy of the element and stripping it from the atom. Photoionization may be a single- or multi-stage process.

Direct Ionization

An atom may be ionized directly from the ground state with a single high-energy photon (Figure 2.4). The ionization energy for $^{133}Ba^{+}$ is $E_i = 5.21$ eV [10, 14, 66, 98]. By the Planck relation:

$$E = \frac{hc}{\lambda} \tag{2.1}$$

where h is the Planck constant and c is the speed of light, the ionization energy corresponds to an ultraviolet photon with wavelength $\lambda_i \leq 238$ nm. Ultraviolet lasers are expensive and difficult to use. Additionally, single-photon ionization is not isotope selective. Therefore, we do not use the direct ionization method.

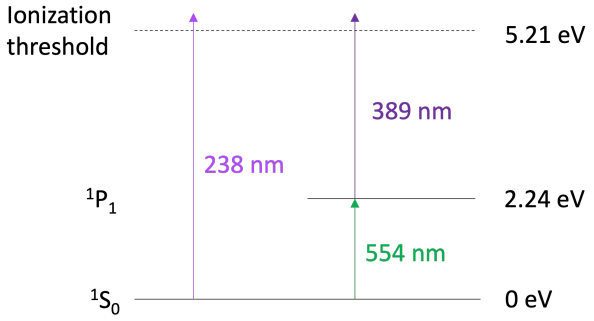

Figure 2.4: Energy level diagram for barium atom ionization techniques (not to scale). Left: direct ionization with a single photon with wavelength $\lambda_i \leq 238$ nm. Right: resonance-enhanced multi-photon ionization with an isotope selective first excitation step with wavelength $\lambda_e = 554$ nm and a second ionization step with wavelength $\lambda_i = 389$ nm.

Resonance-Enhanced Multi-Photon Ionization

Resonance-enhanced multi-photon ionization (REMPI) is a technique for ionizing atoms in multiple steps [4]. The QuantumIon apparatus implements a two-step ionization scheme. First, a valence electron in a neutral atom is photoexcited into a higher energy level. Then, the excited atom absorbs an additional photon with sufficient energy for the excited valence electron to escape the confining potential binding it to the atom.

The primary advantage of the REMPI technique is that it is isotope selective. The first excitation state is at an energy that is specific to a single isotope of barium and can be targeted with a narrow linewidth laser. The photoexcitation laser can be modulated to select the desired isotope. Therefore, only that isotope gets ionized and trapped.

In the apparatus, ionization of $^{133}Ba^{+}$ is achieved with a 554 nm laser for the first excitation stage and a 389 nm laser for the second excitation stage (Figure 2.4). The 389 nm laser excites two electrons into an excited state in the free electron continuum, causing autoionization of one electron and relaxation of the other, resulting in a single electron ionization [50, 55, 124]. Autoionization achieves higher ionization and trapping rates due to the increased cross-section of the 389 nm transition [46].

2.2.3 Target Preparation

Preparing the solid atomic source of $^{133}Ba^{+}$ is challenging given that it has no natural abundance and a microgram amount of material must be used for radiation safety compliance. We procure $^{133}Ba^{+}$ as a high isotopic purity $BaCl_2$ salt in solution and deposit it on a metal substrate [45, 123]. The resulting component is known as the ablation *target*. The target is installed inside the vacuum chamber near the trap.

2.3 Trapping with Electric Fields

Ions have a net charge. Therefore, they can be trapped with electric force fields. Unfortunately, static confinement of a charge in three dimensions cannot be achieved with solely static electric fields according to the laws of electrostatics. For a point charge to remain stationary in a static electric field, it must reach a local electric potential minimum where all of the electric field lines in the region lead to a single point. At that point, the electric force on the charge (Equation 2.2) due to the electric field is zero because there

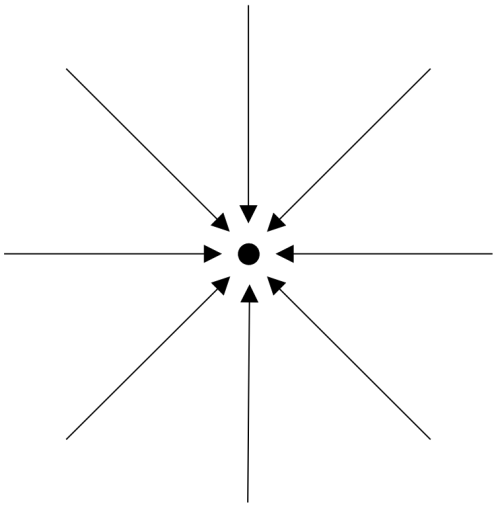

Figure 2.5: For static electric fields to confine an electric charge in three dimensions, the fields must produce a sink with a negative divergence: $\boldsymbol{\nabla} \cdot \mathbf{E} \leq 0$. This is not possible, as stated in Earnshaw's Theorem [40].

is no electric potential gradient (Equation 2.3). That point would then be a sink with a negative divergence (Figure 2.5):

$$\mathbf{F_E} = q\mathbf{E} \tag{2.2}$$

$$\mathbf{E} = -\boldsymbol{\nabla} \cdot \mathbf{V} \tag{2.3}$$

However, Gauss' Law (Equation 2.4) states that the divergence of an electric field in free space (no charge present, $\rho = 0$) must be zero and obey the Laplace equation (Equation 2.5). Thus, the electric field force is also divergenceless and no local force minimum is possible with static electric fields (Equation 2.6). This result is known as Earnshaw's Theorem [40].

$$\boldsymbol{\nabla} \cdot \mathbf{E} = \frac{\rho}{\epsilon_0} \tag{2.4}$$

$$\nabla^2 f = 0 \tag{2.5}$$

$$\begin{aligned}\boldsymbol{\nabla}\cdot\mathbf{F_E} &= \boldsymbol{\nabla}\cdot q\mathbf{E}\\ &= q\boldsymbol{\nabla}\cdot(-\boldsymbol{\nabla}\cdot\mathbf{V})\\ &= -q\nabla^2\mathbf{V}\\ &= 0\end{aligned} \tag{2.6}$$

To overcome this problem, we use another type of field in at least one dimension. Solutions include apparatuses using radio frequency (RF) electric fields known as *Paul traps* [87] or magnetic fields known as *Penning traps* [32]. The QuantumIon apparatus uses a variant of the RF Paul trap.

2.3.1 Trapping with Radio Frequency Electric Fields

Radio frequency (RF) Paul traps are composed of RF and ground electrodes oriented in space and driven such that the electric field produced by the electrodes form a quadrupole potential. The most common construction of Paul trap is the *four-rod trap* [92] which uses four cylindrical rods oriented axially parallel and arranged such that they form a square when viewed from an axial perspective (Figure 2.6). The rods form pairs across the diagonal of the square where two rods are grounded and the other have the same oscillating RF potential $V \propto \cos(\Omega_{rf}t)$ applied to them, where $\Omega_{rf} = 2\pi f_{rf}$ is the angular frequency of the field driven by an electrical RF signal with frequency f_{rf} and t is time since the beginning of the experiment. The resulting electric field behaves like a rapidly spinning saddle point with an effective minimum in the center of the square formed by the rods.

The electric potential generated by RF Paul traps is a three-dimensional quadrupole potential. Quadrupole potentials have the advantages of being relatively simple to generate and of causing the the motion of the ion in the trap to behave in all three spatial dimensions as a simple harmonic oscillator, a well-known physical model. Confinement along one of the axes is usually made much weaker than along the other two axes. In this thesis, the x and y axes will be the strong confinement axes and the z axis will be the weak confinement axis. The x and y axes may also be collectively referred to as the *radial* dimensions and z as the *axial* dimension, referencing the cylindrical symmetry of the system. The weaker confinement in z corresponds to a lower oscillation frequency: $\omega_x, \omega_y \gg \omega_z$. The asymmetry in confinement strength causes the ions to fall into a linear chain along the axial dimension of the trap.

The confining electric potential from an ideal RF Paul trap with hyperbolic electrodes three dimensions is

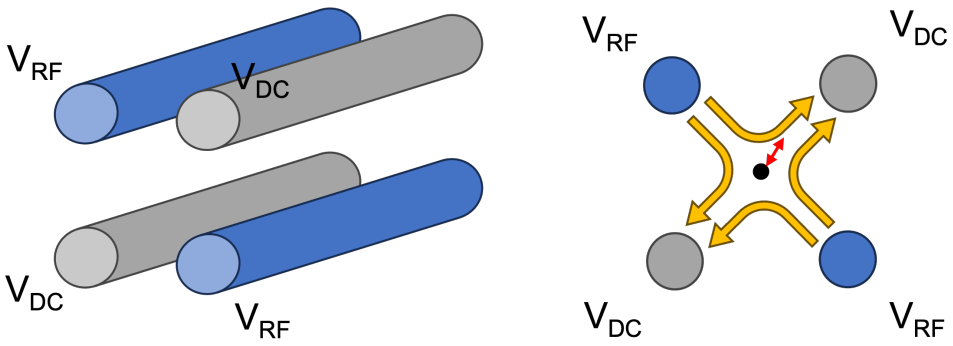

Figure 2.6: Diagram of a four-rod RF Paul trap (not to scale). Only rods for radial RF confinement are shown. Rods labelled V_{RF} have an RF electrical signal applied to them, while rods labelled V_{DC} are grounded. The rods generate a quadrupole pseudopotential with a minimum (known as the *RF null* in the center of the square (indicated with a small black circle). Any stray electric fields that displace the DC potential minimum (*DC null*) from the RF null can cause excess micromotion. End-cap electrodes for axial DC confinement are omitted. Left: oblique angle view. Four cylindrical rods are arranged in space. Right: end-on view. The rods form a square with electrical pairs across the diagonal of a square.

$$\phi = \frac{U}{2}(\alpha x^2 + \beta y^2 + \gamma z^2) + \frac{V}{2}(\alpha' x^2 + \beta' y^2 + \gamma' z^2)\cos(\Omega_{rf} t) \tag{2.7}$$

where α, β, and γ are geometric factors that depend on the size, shape, and relative location of the electrodes generating the confining potential. The geometric terms must satisfy $\alpha + \beta + \gamma = \alpha' + \beta' + \gamma' = 0$ for the confining potential ϕ to satisfy the Laplace equation (Equation 2.5). The potential thus has a static DC component (the U term) and an oscillatory RF component (the V term) that is caused by the oscillating electric field. Confinement in three dimensions can be accomplished with purely RF fields, but in practice the axial confinement is performed with a static field for simplicity. The ideal forms of DC and RF electric potentials are

$$U = U_0 \left(\frac{z^2}{z_0^2} - \frac{x^2 + y^2}{2z_0^2} \right) \tag{2.8}$$

$$V = \frac{V_0}{2} \left(\frac{x^2 - y^2}{r_0^2} \right) \cos(\Omega_{rf} t) \tag{2.9}$$

where U_0 is the DC electrode voltage, V_0 is the RF electrode voltage, z_0 is the axial center of the trap, and r_0 is the radial distance from the center of the trap (DC/RF null) to the electrodes.

We must solve the classical equations of motion for the confining potential to determine the regime in which the motion of the charge is stable and locally confined. Outside of the stable regime, the ion is propelled out of the potential well generated by the trap. The motion along all three axes are independent For simplicity, we consider the motion of a single ion along the x axis. The argument generalizes to all three spatial dimensions.

Applying Newton's Second Law (Equation 2.10) to the equations previously shown for force on a particle of mass m and charge q in an electric potential (Equations 2.2 and 2.3), we obtain:

$$F_x = m\ddot{x} \tag{2.10}$$

$$\begin{aligned} \ddot{x} &= \frac{q}{m} E_x \\ &= -\frac{q}{m}\frac{\partial \phi}{\partial x} \\ &= -\frac{q}{m}(U\alpha + V\alpha' \cos(\Omega_T t))x \end{aligned} \tag{2.11}$$

Under a change of variables (Equation 2.12), the equation of motion takes the form of the Mathieu equation (Equation 2.13) [71, 85], a differential equation with a well-known solution:

$$\begin{aligned} \zeta &= \frac{\Omega_{rf} t}{2} \\ a_x &= \frac{4q}{m}\frac{U\alpha}{\Omega_{rf}^2} \\ q_x &= \frac{2q}{m}\frac{V\alpha'}{\Omega_{rf}^2} \end{aligned} \tag{2.12}$$

$$\frac{\partial^2 x}{\partial \zeta^2} + (a_x + 2q_x \cos(2\zeta))x = 0 \tag{2.13}$$

The a_x and q_x terms are stability parameters that dictate whether the motion of the ion is localized to a certain region of space for all time in a stable trajectory. Under the

condition that $|a_x|, q_x^2 \ll 1$, the ion trajectory is stable and can be approximated using the Floquet Theorem [85] as

$$\begin{aligned} x(t) &\approx 2AC_0 \cos\left(\beta_x \frac{\Omega_{rf}}{2} t\right)(1 - \frac{q_x}{2}\cos(\Omega_{rf} t)) \\ \beta_x &\approx \sqrt{a_x + \frac{q_x}{2}} \end{aligned} \tag{2.14}$$

where $2AC_0$ is a constant that depends on the initial conditions of the ion motion. The result is an approximate simple harmonic oscillator at a *secular frequency* ω_s (Equation 2.15). Some *micromotion* at the trap RF drive frequency Ω_{rf} is superimposed upon the ion trajectory. The magnitude of the micromotion may be minimized by ensuring that no electric fields in the environment displace the DC field null from the RF field null (Figure 2.6), but the micromotion itself can never be eliminated [8].

$$\omega_s = \beta_x \frac{\Omega_{rf}}{2} \tag{2.15}$$

When the oscillating RF potential V (Equation 2.9) is averaged over the period of the RF drive signal oscillation, the potential may be expressed as $V = V_0/2r_0^2$ for an ideal hyperbolic electrode. Under normal trap operating conditions, the stability parameter $a_x \approx 0$ and the charge of $^{133}Ba^+$ is $q = +e$. With $2AC_0 \coloneqq 1$ for simplicity, the equation of motion may be re-expressed as

$$\begin{aligned} x(t) &\approx \cos(\omega_s t)(1 - \frac{q_x^2}{2}\cos(\Omega_{rf} t) \\ \omega_s &= \frac{eV_0}{mr_0^2 \Omega_{rf}\sqrt{2}} \\ q_x &= \frac{2\sqrt{2}\omega_s}{\Omega_{rf}} \end{aligned} \tag{2.16}$$

An example of an ion trajectory along the x axis according to the Equation 2.16 is shown in Figure 2.7. The parameters used for the calculation are given in Table 2.1. A similar trajectory is followed in all three spatial dimensions, though we expect the exact trajectories to differ slightly due to the fact that we are using a surface trap, not an idealized hyperbolic electrode trap.

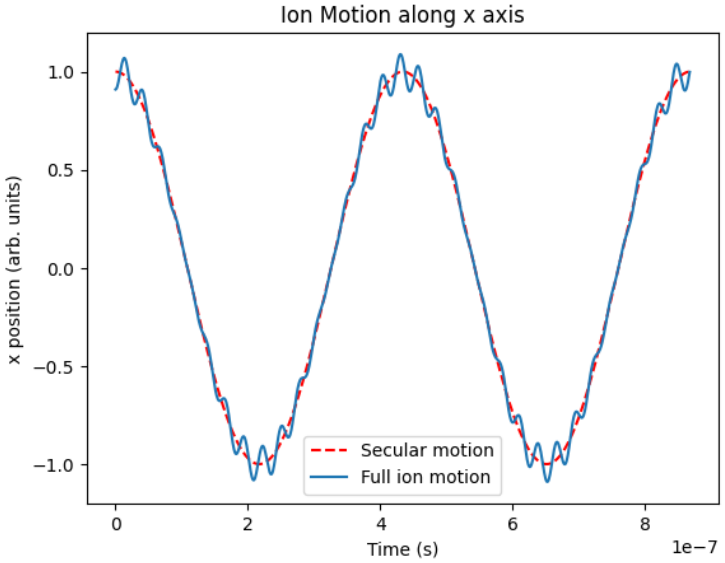

Figure 2.7: Plot of the simulated motion of a single $^{133}Ba^{+}$ ion in an idealized RF Paul trap along the x direction. The ion oscillates in the potential well at the secular frequency $\omega_s = 2\pi \times 2.3$ MHz with micromotion at the trap RF drive frequency $\Omega_{rf} = 2\pi \times 36$ MHz.

The *trap depth* is the potential energy of the confining electric potential well, which corresponds to the maximum kinetic energy that an ion can have when intersecting with the electric potential generated by the trap and be captured. The trap depth is given by

$$d = \frac{1}{2}\alpha m \omega_s^2 r_0^2 \tag{2.17}$$

where α is a geometric factor that is specific to the trap [93].

Axial confinement is achieved with two end-cap electrodes with static DC electric potentials on either end of the trap. The magnitude of the axial DC potential on the end-caps creates an axial harmonic well and defines the axial equilibrium positions and spacing of ions in the trap.

Multiple ions may be loaded into a single trap. As they have the same charge, they repel each other through Coulomb force. The vibrations of multiple ions mediate entanglement in ion traps and are used to implement coherent entangling quantum operations [117]. Multiple ion interactions are beyond the scope of this thesis.

2.3.2 Surface Traps

For QIS applications, elongated Paul traps that trap multiple ions in linear chains are the most popular because they trap relatively large numbers of ions with enough optical access to permit individual laser addressing to each ion. Linear Paul traps have been implemented as four-rod traps, blade traps, and microfabricated traps with one or more layers [106, 114]. In the QuantumIon apparatus, we use a variant of a Paul trap known as a microfabricated *surface* trap [23].

In a surface trap, the RF and ground electrodes are flat, rectangular, and planar, and reside in parallel on the same surface, as though a four-rod trap had been unrolled and pressed flat (Figure 2.8). Crucially, the RF and ground electrodes must alternate so that each RF electrode is adjacent to only ground electrodes, not the other RF electrode. The alternating arrangement creates a quadrupole electric potential that is displaced from the surface of the trap (Figure 2.8). The equations for the electric potential generated by the trap and the equations of motion for an ion in that potential discussed in Section 2.3.1 still apply with only modifications to the boundary conditions of the electric potential.

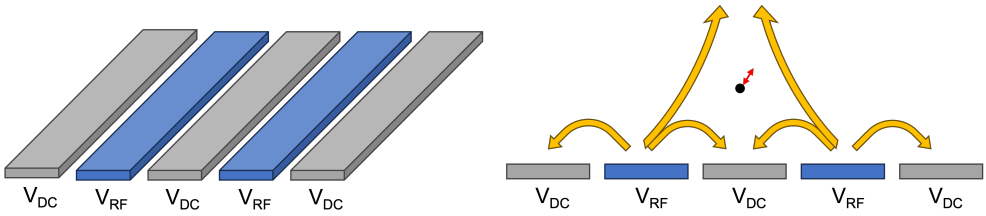

Figure 2.8: Diagram of the RF and DC electrodes in a surface ion trap (not to scale). Electrodes labelled V_{RF} have an RF electrical signal applied to them, while electrodes labelled V_{DC} are grounded. The RF and DC electrodes alternate. RF and DC electrodes alternating creates a quadrupole potential well above the surface of trap (black dot). If the DC null is displaced from the RF null (red arrow), excess micromotion can occur. Left: oblique angle view of the electrodes in a plane. Right: end-on view. The electric field lines generated from the electric potentials on the RF electrodes.

Advantages

Microfabricated surface traps have some advantages over other forms of linear traps. The planar nature of surface traps and the materials they are composed of allow manufacturers to use the same mature microfabrication technologies and techniques used to create computer chips and other microfabricated metal devices. These techniques enable the design

and fabrication of smaller ion traps with finer features and greater tolerance than other forms of traps, which are often handmade. Greater tolerance increases confidence in the trap by increasing the likelihood that the trap is built and performs as designed.

Building surface traps using microfabrication techniques also could help scale up ion trap quantum information processors to many qubits. Microfabrication is highly repeatable, enabling mass manufacturing of traps. Additionally, some surface trap designs feature multiple DC electrodes arrayed along the axis of the trap rather than just two end-cap electrodes at the end of the trap [75, 93]. In designs where each DC electrode can be individually controlled, custom axial confining electric potentials may be applied to the ions in the trap. Proposals for alternate confining potentials include quartic axial potentials for uniform ion spacing [6, 67] and time-varying axial potentials to ion shuttling to different regions of the trap [76, 86, 88, 121].

Disadvantages

Surface traps also introduce some challenges into ion trap apparatuses. The electric potentials wells generated by surface traps are typically shallower than other trap designs, which weakens confinement [23]. Surface traps also introduce engineering difficulties into assembly of the ion trap apparatus. The traps are an extended flat surface, so laser beams must pass over the surface of the trap. Some trap designs may include apertures to allow laser beams to pass through the trap surface. In both cases, laser beams must be shaped and aligned with care to avoid clipping the trap, which could deform the beam, scatter light, and impart electrical charge on to the trap. Large numbers of controllable DC electrodes introduce more electrical channels that must be designed, assembled, and controlled, introducing complexity into the apparatus.

The surface traps themselves may also be difficult to fabricate, with known issues including low fabrication yields and production of gold-aluminum intermetallic alloy known as *purple plague* during vacuum chamber bake-out processes [22]. Successfully fabricated traps are also small and fragile, which can make them hard to handle when installing in the apparatus.

The potential for scaling ion trap processors and investigating the advantages of shuttling processes makes surface traps well worth the challenges of using them. Multiple fabrication facilities design, build, and ship surface traps [23, 75, 93, 103] and surface traps have been used to successfully trap several ion species, demonstrate shuttling, and implement simple trapped ion quantum information processors [27, 88, 102].

2.3.3 Application to the Apparatus

We designed the QuantumIon apparatus for the novel capability of trapping barium ions, particularly $^{133}Ba^{+}$ ions, in a surface trap. The apparatus uses a Phoenix ion trap designed and fabricated by Sandia National Laboratories [93]. The target RF trap parameters for the apparatus are shown in Table 2.1. Values for the trap radius r_0, trap depth geometry factor α, and safe RF drive voltage V_0 are specific to the Phoenix trap. The choice of trap RF drive frequency is a balancing act between maximizing the secular frequency to accelerate entangling operations and keeping the stability parameter q_x within a tolerable range (ideally $q_x < 0.1$). The final trap RF drive frequency is determined by the resonance frequency of the as-built resonator (Section 3.1.1). Note that exact parameter values may vary due to changes in the apparatus and tuning during experiments.

Parameter	**Value**
$^{133}Ba^{+}$ mass m	133 amu
Trap characteristic radius r_0	140 μm
Trap depth constant α	0.028
RF drive frequency Ω_{rf}	$2\pi \times 36$ MHz
RF drive voltage V_0	250 V
Secular frequency ω_s	$2\pi \times 2.3$ MHz
Stability parameter q_x	0.18
Trap depth d	0.08 eV
RF null position R	68 μm

Table 2.1: Summary of input and calculated parameters for calculation of the trajectory of a single $^{133}Ba^{+}$ ion in an idealized hyperbolic electrode RF Paul trap according to Phoenix trap parameters [93]. The micromotion frequency is equal to the trap RF drive frequency. The stability parameter value $q_x^2 \ll 1$ indicates that these parameters should produce a stable trapping potential.

Calculating voltages for DC electrodes to produce the axial confining potential remains an open research question while attempting to trap our first ion. Initial attempts at trapping $^{138}Ba^{+}$ have used simple voltages on a subset of the available electrodes. The minimal mass difference between $^{133}Ba^{+}$ and $^{138}Ba^{+}$ means the trapping parameters calculated previously should work effectively for $^{138}Ba^{+}$

2.3.4 Trapping Techniques

Our first attempts to trap ions have included two different trapping techniques. We refer to the techniques as *direct ion loading* and *photoionization*. We have not yet succeeded in trapping barium ions with either technique.

Direct Ion Loading

For direct ion loading, we set the voltages on the DC electrodes of the trap and turn off the RF drive signal. We operate the ablation laser at high power to produce ions directly from the atomic source (Section 2.2.1). After waiting for the ion plume to pass into the trapping region, we turn on the RF drive signal. The cooling and repump lasers remain on for the entire procedure, cooling ions in the trapping region and scattering photons for detection (Section 2.4.1).

The main advantage of direct ion loading is that the optical instrumentation required is relatively simple, since no photoionization is required (Section 2.2.2). The only components that must be actively controlled are the ablation laser trigger and trap RF drive signal. Thus, direct ion loading is an attractive technique when trying to demonstrate initial trapping capability while assembling a new apparatus.

Direct ion loading has some disadvantages. It is not an isotope-selective technique, since ions of any elements and molecules present in the atomic source are likely to be ionized. The presence of so many species may crowd out the desired species from the trap. Additionally, because direct ion production from ablation only occurs at high laser intensities, the ions produced are likely to have high kinetic energy. The high kinetic energy of ions makes them more difficult to trap, especially when using surface traps with lower trap depths. Finally, direct ion loading requires real-time capabilities in the control system, since the RF trapping signal must be turned on and ramped up in amplitude at the precise moment that ions are in the trapping region to avoid *anti*-trapping the ions and forcing them out of the trapping region.

Photoionization

The photoionization loading technique uses lasers to photoionize neutral atoms once they pass into the trapping region. For photoionization loading, the RF and DC electric fields are always on, as are the REMPI ionization, cooling, and repump lasers. The ablation laser operates at lower power, producing a plume of mostly neutral atoms. The plume propagates

into the trapping region since the neutral atoms are not deflected by the electric trapping potential. The ionization lasers ionize just the desired isotope of barium in the trapping region. Once ionized, the ions are confined by the electric trapping potential. All other atomic and molecular species propagate out of the trapping region.

The advantages of photoionization loading are improved loading physics and simpler control system requirements. Using REMPI lasers means that the loading procedure is isotope selective. Operating the ablation laser at lower intensity means that less atomic and molecular species are ionized and compete with the target isotope. Additionally, the average kinetic energy of the atom plume is lower, increasing the proportion of ions that can be captured for a given trap depth. The fact that all electric signals and lasers are always active removes the requirement for real-time controls.

The disadvantage of photoionization loading is that the technique moves the complexity of the procedure to the optical portion of the ion trap apparatus. Additional lasers must be installed, frequency locked, and aligned compared to direct ion loading.

2.4 Laser Cooling

When ablated neutral atoms or ions encounter the trapping region, they are *hot*; they are moving very quickly and have high kinetic energy. A minority of the ions (whether ionized during ablation or photoionized) will be moving slowly enough to have kinetic energy less than the trap depth and be confined by the trapping potential. Even once trapped, the ions will have too much energy to operate as qubits or even remain sufficiently localized in the center of potential well to be imaged. When ions become sufficiently cold, their oscillatory motion in the confining potential behaves as a quantum harmonic oscillator. Cooling the ions to close to the motional ground state is necessary to operate the ions as qubits and image them. The cooling operation is performed with lasers.

Laser cooling leverages the momentum of photons and conservation of momentum to remove energy from the ions by scattering light off the ions. The cooling pipeline leverages three separate techniques: *Doppler cooling* [83, 126], *(quenched) resolved sideband cooling* (RSC) [37, 74, 78], and *electromagnetically induced transparency* (EIT) cooling [3, 64]. Doppler cooling is the simplest cooling technique, but cannot cool ions all the way to the ground state as is required for quantum information experiments.

This section will focus on Doppler cooling as it is the primary technique required for initial trapping experiments. For additional information on laser cooling in the QuantumIon apparatus, especially using RSC and EIT cooling, see [120].

2.4.1 Doppler Cooling

Photons have momentum proportional to their energy:

$$\mathbf{p} = \hbar\mathbf{k} \tag{2.18}$$

where $\hbar$ is the reduced Planck constant, and $\mathbf{k}$ is the wave vector of the photon. When an atom absorbs a photon, the atom is excited into a higher energy level and its momentum is changed equivalent to the momentum of the absorbed photon. Similarly, when the atom relaxes back to a lower energy state by emitting a photon, the atom's momentum is changed equal and opposite to that of the emitted photon (Figure 2.9).

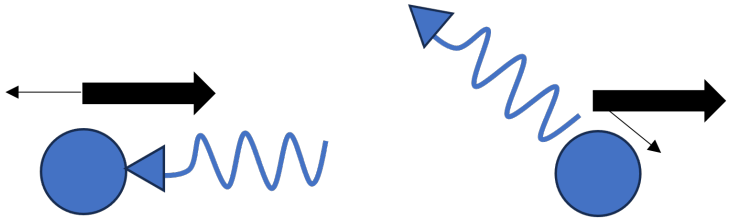

Figure 2.9: Diagram of a photon scattering from an atom (not to scale). Left: when the atom absorbs the photon, its momentum changes. Right: when the atom emits the photon, its momentum changes as well. Since the direction of photon emission is random, the net change of momentum due to photon emission averages to zero, while the change in momentum due to preferential absorption of photons from a single direction may be significant. The black arrows represent the momentum of the atom, with the large arrow indicating the motion of direction of the atom and the small vector showing the change of momentum due to scattering events with the photon.

Doppler cooling leverages two key phenomena: the direction of photon absorption can be controlled while the direction of photon emission is random, and that atoms (or any observer) moving at high speed observe a Doppler shift in the frequency of light in the direction of motion.

We control the direction in which photons interact with an ion in motion by carefully choosing the orientation of the lasers in the apparatus. On the other hand, light emitted by an ion due to spontaneous emission is emitted in a random direction. Therefore, when averaging over a large number of scattering events, the change of momentum in the ion due to photon emission averages to zero, while the change of momentum in the ion due to photon absorption in a sepcific direction accumulates. The repeated scattering events thus

result in net removal of momentum from the ion, provided that a sufficiently large number of scattering events occur.

The Doppler effect is the physical phenomena where relative motion between the source and observer of a wave causes the observer to detect a change in the frequency of the wave. Relative motion towards the source results in an increase in the apparent wave frequency while relative motion away from the source causes a decrease in the apparent frequency. In light, the increase in frequency due to the Doppler effect is called a *blue-shift* and the decrease in frequency is known as a *red-shift* (Figure 2.10).

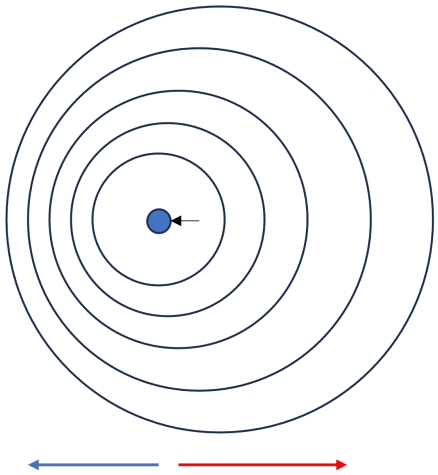

Figure 2.10: Diagram of the Doppler effect. The frequency of a wave appears to increase in the direction of relative motion of the wave source and observer (blue-shift) and decrease in the opposite direction (red-shift). No apparent change in frequency is observed orthogonal to the direction of relative motion.

For laser cooling to work, the ion must interact only with the laser light when moving in one direction. If it also absorbs photons when moving in the opposite direction, momentum will be removed from the ion when moving in one direction only for the momentum to be added back when the ion moves the other way in oscillatory motion in the trap. We leverage the Doppler effect to ensure that the ion only interacts with the laser light when moving towards the laser by red-shifting the cooling laser relative to the transition energy of the ion. When the ion moves towards the laser, it experiences the photons as blue-shifted back into resonance with an atomic transition and scatters photons. When it moves away from the laser, it experiences the photons as red-shifted even further out of resonance and does not scatter them. The cooling laser *must not* be blue-shifted relative to the ion transition frequency; this would heat up the ion!

The ion scatters photons preferentially in a single direction, resulting in net removal of energy from the ion. Thus, the Doppler effect and the ion trap itself ensure that enough scattering events occur to cool the ion significantly. Ions confined in a trap engage in oscillatory motion in a confined space, guaranteeing that the ions can repeatedly interact with the laser beam. Careful selection of the orientation of the cooling laser propagation direction relative to the ion trap axes enables the laser to perform Doppler cooling on all three axes of ion motion within the trap simultaneously.

2.4.2 Energy Levels in Doppler Cooling

Effective Doppler cooling requires a closed-loop scattering interaction such that the transition can be driven repeatedly and rapidly. The laser light used to interact with the $^{133}Ba^{+}$ ion should be carefully chosen such that when the ion is excited, it quickly relaxes back into an energy state such that it can readily be excited again. Additionally, since $^{133}Ba^{+}$ has a nuclear spin of $I = 1/2$, consideration must be paid to the hyperfine splitting of the energy levels to drive the appropriate transitions.

Doppler cooling $^{133}Ba^{+}$ primarily engages the transition between the ground state ($^2S_{1/2}$) and first excited state ($^2P_{1/2}$). That transition is resonant with 493 nm light, so we use a laser at that wavelength (Section 3.2). Both states have hyperfine splitting into the states with $F = 0$ and $F = 1$ total atomic angular momentum. Further, the $F = 1$ levels have three degenerate hyperfine states each. A $B = 5$ G magnetic field oriented parallel to the trap surface a perpendicular to the trap axis establishes the quantization axis (Section 3.4) and creates Zeeman splitting between the $F = 1$ states so that they can be addressed and to prevent the the ion from falling into a coherent dark state [47].

During Doppler cooling, ions must be excited when in either the $F = 0$ or $F = 1$ states in the ground state. The targeted transitions are $|S; F = 0\rangle \rightarrow |P; F = 1\rangle$ and $|S; F = 1\rangle \rightarrow |P; F = 0\rangle$ because of the selection rule that prohibits $\Delta J = 0 = \Delta m_f = m_f = 0$ transitions. π-polarized light is required for transitions where $\Delta m_f = 0$ and $\sigma_{\pm}$-polarized light is required for transitions where $\Delta m_f = \pm 1$. The linewidth of the 493 nm laser exceeds the Zeeman splitting of the $F = 1$ states ($w_Z \approx 5$ MHz) but is less than the linewidth of the excited state transition ($\Gamma = 1/\tau \approx 2\pi \times 20$ MHz for state lifetime $\tau_e \approx 8$ ns) [47]. The hyperfine splitting for the ground and excited states are $\Delta\omega_g \approx 9.9$ GHz and $\Delta\omega_e \approx 1.8$ GHz, respectively, both much larger than the transition linewidth. Therefore, the laser can drive transitions to and from the $F = 1$ degenerate states simultaneously, but cannot target transitions from states with different total atomic angular momenta F simultaneously.

The excited state has a short lifetime of $\tau_e \approx 8$ ns, which is beneficial for rapid cooling. Unfortunately, the excited state does not deterministically relax to the ground state. The excited state has a $3:1$ branching ratio between the ground state and a metastable $^2D_{3/2}$ state. About 25% of the time, the excited ion relaxes in to the metastable state. The metastable state earns its name with a relatively long lifetime of $\tau_m \approx 30$ s. While in the metastable state, the ion does not interact with the 493 nm laser and cannot be cooled. Rather than wait for the ion to relax on its own, we *repump* the ion out of the metastable state back into the excited state. The transition between the metastable state and excited state is resonant with a 650 nm laser. The repump operation closes the loop on the cooling interactions and allows the $^{133}Ba^+$ ion to be rapidly cooled.

The metastable state also has hyperfine split states at $F = 1$ and $F = 2$. Similar to the cooling transition between the ground and excited states, the repump transition frequencies must drive transitions from both hyperfine states while obeying selection rules and avoiding driving undesirable transitions. Figure 2.11 shows the energy level diagram of $^{133}Ba^+$ with the transitions driven for Doppler cooling.

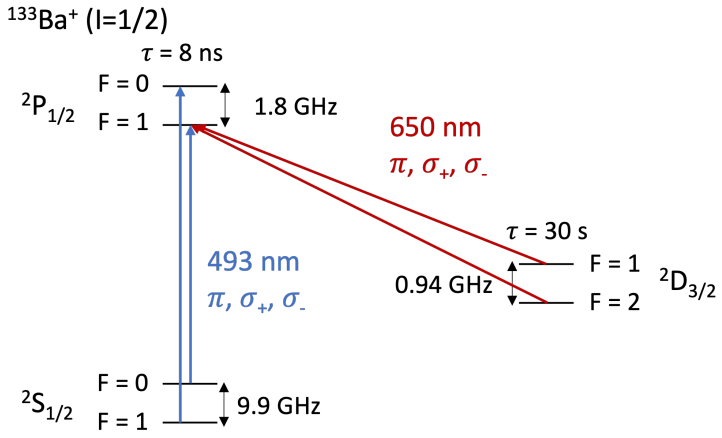

Figure 2.11: Energy level diagram for $^{133}Ba^+$ with the transitions required for Doppler cooling shown (not to scale). The 493 nm transition between the ground and excited states performs the cooling. The 650 nm transition between the metastable and excited state repumps the ion out of the metastable state to resume cooling. Degenerate hyperfine states are omitted.

2.4.3 The Doppler Limit

Doppler cooling unfortunately cannot cool an ion all the way to the motional ground state [20]. The minimum temperature that can be reached with Doppler cooling is the *Doppler limit*

$$T_D = \frac{\hbar\Gamma}{2k_B} \tag{2.19}$$

where Γ is the transition linewidth and k_B is the Boltzmann constant. The transition linewidth is the inverse of the transition lifetime ($\Gamma = 1/\tau$). In terms of laser parameters, the steady-state temperature that can be reached using Doppler cooling is given by [65]

$$\begin{aligned} T_D &= \frac{\hbar\Gamma}{8k_b}(1+\zeta)\left((1+s)\frac{\Gamma}{2|\Delta|} + \frac{2|\Delta|}{\Gamma}\right) \\ s &= \frac{I/I_{sat}}{1+4\Delta^2/\Gamma} \approx \frac{I}{I_{sat}} \\ \Delta &= -\frac{\Gamma\sqrt{1+s}}{2} \end{aligned} \tag{2.20}$$

where ζ is the momentum change from spontaneous emission, s is the saturation parameter, I is the laser intensity, I_{sat} is the saturation intensity of the transition, and Δ is the laser detuning from the transition frequency. Equation 2.20 is valid for $\Delta < 0$. Otherwise, the laser would be blue-shifted and would heat up the ion!

In the QuantumIon system, the Doppler limit is expected to be on the order of $\bar{n} \approx 2-10$ motional quanta [47, 120]. Cooling to the motional ground state ($\bar{n} = 1$) requires other techniques as discussed in [120].

2.5 State Preparation and Measurement

The most basic quantum operations are state preparation and measurement (SPAM). State preparation is the act of putting the qubit into a known initial state, usually $|0\rangle$. Measurement in this case is a global destructive measurement of the quantum state which collapses the qubit to a computational basis state.

The SPAM operations are performed with lasers. The lasers that perform SPAM are the same 493 nm and 650 nm lasers used for Doppler cooling modulated to target transitions between different hyperfine levels.

2.5.1 State Preparation

State preparation for trapped ions is achieved with a technique called *optical pumping*. A set of transitions between the hyperfine split levels of the ground and excited states are chosen such that the ions must eventually be driven into a single known hyperfine energy level. Crucially, no transition wavelength can be allowed to excite the ion out of the chosen final energy state. The ion is exposed to the laser light until it stops scattering photons, at which point it is dark and known to be in the chosen state.

In the $^{133}Ba^{+}$ qubit, the final energy state after optical pumping should be the $|0\rangle = |S; F = 0\rangle$ state. The 493 nm laser is modulated to excite the ion from the $|S; F = 1\rangle$ states to the $|P; F = 1\rangle$ states, from which the ion can relax into the $|S; F = 0\rangle$ state. The laser *must* avoid exciting the ion from the $|S; F = 0\rangle$ state.

Just as with Doppler cooling, the ion can relax to the metastable state instead of the ground state during optical pumping. The 650 nm repump laser must be applied to continue optical pumping without waiting for the ion to relax from the metastable state to the ground state. Figure 2.12 shows the energy level diagram of $^{133}Ba^{+}$ with the transitions required for state preparation.

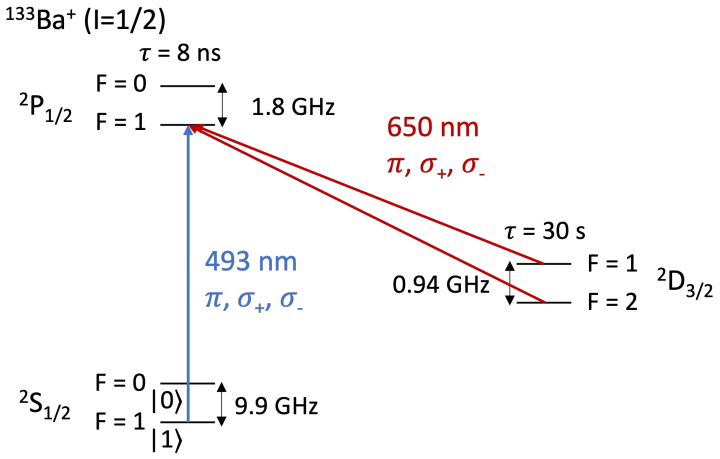

Figure 2.12: Energy level diagram of $^{133}Ba^{+}$ with the transitions for state preparation shown (not to scale). After optical pumping, the ion will be in the $|0\rangle = |S; F = 0\rangle$ state. Degenerate hyperfine states are omitted.

2.5.2 Measurement

The goal of the measurement procedure is to drive a set of closed-loop transitions (similar to Doppler cooling in Section 2.4) where the ion continually fluoresces if it is in one quantum computational basis state and remains dark if it is in the other. The measurement collapses any superposition of computational basis states such that the readout continues with the ion staying in the same state after it collapses so sufficient photons can be collected to determine the ion state. In the QuantumIon apparatus, the $|0\rangle$ of $^{133}Ba^{+}$ is defined as the dark state and $|1\rangle$ is the bright state.

The transitions selected for measurement are nearly the inverse of those used in state preparation (Section 2.5.1). The ion must not be excited out of the $|S; F = 0\rangle$ state so that the $|0\rangle$ state remains dark. However, we also want to prevent ions that were not previously in that state from relaxing into it. Therefore, the $|S; F = 1\rangle$ states are all excited to exclusively the $|P; F = 0\rangle$ state, which is prohibited from relaxing into the $|S; F = 0\rangle$ state by the selection rule that prohibits $\Delta J = \Delta m_f = m_f = 0$ transitions. Thus, the ion can only relax back to $|S; F = 1\rangle$ states and be continually excited in a cycle.

Just as with Doppler cooling (Section 2.4.1) and state preparation (Section 2.5.2), the excited state may relax to the metastable state. The 650 nm repump laser again excites the ion out of the metastable state to the excited state to continue the closed detection excitation loop. Figure 2.13 shows the energy level diagram of $^{133}Ba^{+}$ with the transitions required for state measurement.

2.5.3 Laser Frequency Modulation

In order to target multiple energy level transitions between different hyperfine levels in the ground, excited, and metastable stables, the laser light for the given transition may be modulated or multiple lasers may be employed. Multiple-laser implementations are expensive and technically challenging, so we implement optical light modulation for all lasers that drive quantum operations in the QuantumIon apparatus.

We use electro-optical modulators (EOMs) to modulate the light emitted from the continuous wave (CW) lasers in the QuantumIon apparatus (Section 3.2.4). EOMs emit *sidebands* of light with modulated frequencies along the same beam path as unmodulated *carrier* frequencies. The emitted frequencies are ω_c and $\omega_{sb} = \omega_c \pm \omega_{rf}$ where ω_c is the carrier frequency, ω_{sb} is the sideband frequency, and $\omega_{rf} = 2\pi f_{rf}$ is the modulation frequency due to an RF signal at cyclical frequency f_{rf} input into the EOM. Thus, three frequencies of light are always emitted from an EOM when modulating the frequency of a laser beam.

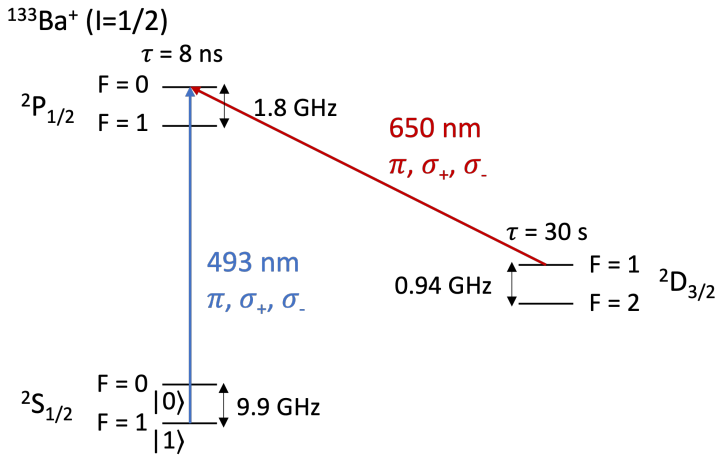

Figure 2.13: Energy level diagram of $^{133}Ba^{+}$ with the transitions for state measurement shown (not to scale). The ion collapses from any superposition of computational basis states to either the $|0\rangle$ or $|1\rangle$. It continually scatters light if in the $|1\rangle$ state and otherwise remains dark. Degenerate hyperfine states are omitted.

The frequencies of light that are emitted by the EOM for laser operations must correspond to the hyperfine splitting of the ground, excited, and metastable states and avoid resonance with undesirable transitions. Since three frequencies are always emitted when modulating light with an EOM, the RF frequencies that drive the EOM must be chosen carefully. Modulation frequencies may be selected such that the carrier frequency and/or the sidebands are resonant with a transition of interest. Additional considerations include the fact that the carrier wavelength often has higher power than the sidebands and drives transitions faster, and that frequencies blue-shifted relative to a transition frequency risk heating the ion (via the Doppler effect!).

A typical procedure for choosing modulation frequencies is to tune the laser (carrier) to the frequency required for state measurement (Section 2.5.2) because that operation requires a single frequency. Modulation frequencies then may be chosen to target the state preparation (Section 2.5.1) and Doppler cooling frequencies. One must then consider whether any of the generated sidebands drive undesirable transitions (for the given operation) or whether any sidebands are blue-shifted relative to a transition and may heat the ion and modify the choice of modulation frequencies accordingly.

The modulation frequencies chosen for the 493 nm laser in the QuantumIon apparatus use sidebands to drive the transitions for Doppler cooling and SPAM. If the carrier (unmod-

ulated laser tuned to a specific frequency) drives the measurement transition, the frequency spanned by the hyperfine splitting is $\Delta\omega > 11$ GHz, which demands a wider bandwidth than most commercially available EOMs support. Therefore, we select a frequency for the carrier that is between the frequencies resonant with the measurement transition and the optical pumping transition and modulate the laser. The carrier must be closer to the optical pumping transition than the measurement transition because otherwise the alternate sideband generated when driving the measurement transition becomes too near one of the Doppler cooling transitions on the blue-shifted side, risking driving Doppler *heating*! The carrier and remaining sidebands are sufficiently detuned from transition frequencies that they will not have any effect on the ion. Additional minor optimizations to allow cooperation with other species of barium ions contribute to the selected modulation frequencies. Figure 2.14 shows the transitions between the ground and excited state, how they relate in frequency space, and how the selection of the carrier and modulation frequencies drives all the necessary transitions for Doppler cooling and SPAM for the 493 nm laser.

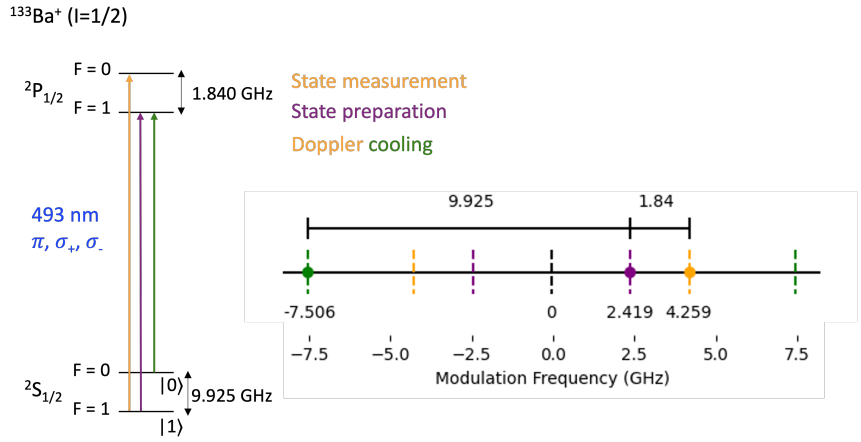

Figure 2.14: Diagrams and plots of the modulation frequencies for the 493 nm laser and how they related to ionic energy level transitions in $^{133}Ba^{+}$ (not to scale). Left: simplified energy level diagram showing the transitions between hyperfine levels for Doppler cooling and SPAM. Right: plot showing how the carrier and modulation frequencies relate in frequency space. The origin is defined as the carrier frequency so that the modulation frequencies are shown directly. Dots represent transition frequencies and vertical dotted lines represent laser sideband frequencies. Sidebands drive all the energy level transitions. The carrier and sidebands that are not resonant with transitions are sufficiently detuned from transitions as to not effect the ion. The differences between carrier frequencies correspond to the hyperfine splitting between the ground and excited state.

We perform a similar frequency analysis to select modulation frequencies for the 650 nm repump laser. Fortunately, this is a much simpler task. The hyperfine splitting of the metastable is much smaller than the hyperfine splitting of the ground state. Therefore, we tune the carrier to the measurement repump transition and drive the Doppler cooling and optical pumping transitions with sidebands. The carrier then drives an undesired transition during optical pumping since an ion in the $|P; F = 0\rangle$ state cannot relax into the $|S; F = 0\rangle = |0\rangle$ because of the selection rule $\Delta J = \Delta m_f = m_f = 0$. This transition is of little consequence because the lifetime of the excited state is so small that the optical pumping routine will be able to quickly continue and the ion will stop responding to light once it is prepared in the $|0\rangle$ state. The carrier will also drive an acceptable transition during Doppler cooling. The sidebands that are not tuned to atomic transition are detuned sufficiently to not effect the ion. Figure 2.15 shows the transitions between the metastable and excited state, how they relate in frequency space, and how the selection of the carrier and modulation frequencies drive all the necessary transitions for Doppler cooling and SPAM for the 650 nm laser.

The modulation frequencies for the 493 nm and 650 nm lasers that drive Doppler cooling and SPAM transitions are reported in Table 2.2. Additional frequencies chosen by a similar process for the 614 nm shelving repump laser are shown for completeness. The shelving operation is outside the scope of this thesis. Section 3.2.4 describes how laser light modulation is accomplished in the QuantumIon apparatus.

Laser (nm)	**Cooling (GHz)**	**Preparation (GHz)**	**Measurement (GHz)**
493	7506, 4259	2419	4259
650	903, 1840	903, 1840	0
614	217	217	217

Table 2.2: Summary of the modulation frequencies required for Doppler cooling and SPAM for $^{133}Ba^{+}$. The frequencies depend on the locked frequency for each laser. The 614 nm is used for shelving repump, an operation which is beyond the scope of this thesis.

Similar arguments hold for selecting the modulation frequencies for other isotopes of barium ions. $^{137}Ba^{+}$ requires different modulation frequencies, while $^{138}Ba^{+}$ requires no modulation at all because it has no nuclear spin ($I = 0$), and therefore no hyperfine split levels.

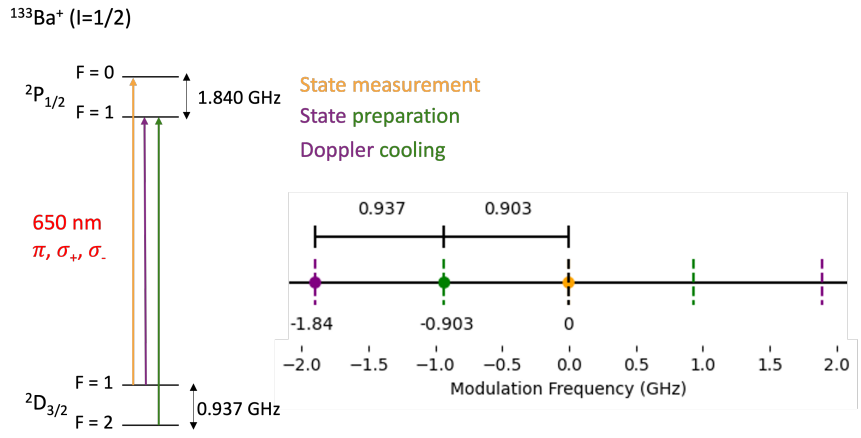

Figure 2.15: Diagrams and plots of the modulation frequencies for the 650 nm laser and how they relate to ionic energy level transitions in $^{133}Ba^{+}$ (not to scale). Left: simplified energy level diagram showing the transitions between hyperfine levels for Doppler cooling and SPAM. Right: plot showing how the carrier and modulation frequencies relate in frequency space. The origin is defined as the carrier frequency so that the modulation frequencies are shown directly. Dots represent transition frequencies and vertical dotted lines represent laser frequencies. The carrier is tuned to the frequency resonant with the measurement transition. Therefore, that frequency is present and drives transitions in all operations. Sidebands are the primary driver of optical pumping and Doppler cooling transitions. The sidebands that are not resonant with transitions are sufficiently detuned from transitions as to not effect the ion. The differences between carrier frequencies correspond to the hyperfine splitting between the ground and excited state.

2.6 Quantum Gates

Quantum gates are required to complete the implementation of a trapped ion qubit. For completeness, a brief description of trapped ion quantum gates follows. Full quantum gate design and implementation are beyond the scope of this thesis.

2.6.1 Single-Qubit Gates

Single-qubit gates are manipulations of the quantum state of a single qubit independent of the behavior of any other qubit. Trapped ion systems using hyperfine clock states qubits can implement single-qubit gates with two methods: microwave gates and laser gates.

Microwave Gates

Microwave gates use microwave radiation at the qubit transition frequency to directly drive a transition between the computational basis states encoded in the ground state of the ion [16]. Microwave gates are simple to implement, but can only be used for single-qubit gates. The large wavelength of microwaves also results in driving gates in multiple ions at a time unless the ions are separated by relatively large distances.

Laser Gates

Laser gates implement transitions between the computational basis states with lasers through a Raman interaction. Two lasers tuned to virtual state transition frequencies create a beat note frequency (difference between the frequencies of the lasers) equal to the qubit transition frequency [12]. The virtual state is never populated. An energy level diagram indicating the relevant transitions for $^{133}Ba^{+}$ is shown in Figure 2.16.

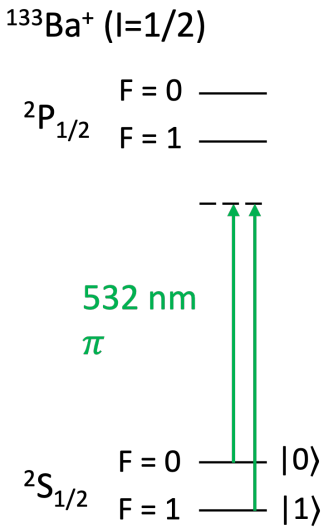

Figure 2.16: Simplified energy level diagram for the two-photon stimulated Raman transition in $^{133}Ba^{+}$. The beat note frequency between the transitions from $|0\rangle$ and $|1\rangle$ to a virtual energy level are equal to the qubit transition frequency.

Laser gates have multiple advantages over microwave gates. Lasers can be tightly spatially focused, enabling individually addressed gates that only act on single ions, leaving

neighboring ions undisturbed. The tight focus of the laser light creates a denser electric field, enabling faster gates than microwave gates.

2.6.2 Multi-Qubit Gates

Multi-qubit gates build on single-qubit laser gates by shining lasers on two (or more) ions in a chain in a single trap. Raman interactions driven with individually addressed lasers implement the multi-qubit gates [5]. The laser light is modulated to create spin-dependent forces on the ions which are exposed to the lasers. The affected ions then vibrate in common motional modes which mediate entanglement between the targeted ions.

Chapter 3

Electrical System

Many of the components of an ion trap must be controlled by electrical signals. This chapter describes the electrical components in the QuantumIon system and the electrical systems designed and implemented to drive them. The performance requirements for each component and circuit for trapping $^{133}Ba^{+}$ are also presented. Electrical control signals for real-time operation of the ion trap are generated by the control hardware described in detail in Chapter 4. The remaining signals are generated by auxiliary non-real-time hardware.

In order to isolate the ion trap apparatus from the environmental, the trap and optics are housed inside an air handling unit (AHU) that controls the temperature, pressure, and humidity of the air around the apparatus (Figure 3.1a). Optical components are located on the optics table that holds the vacuum chamber containing the ion trap or in drawers in an adjacent computing hardware rack called the *optics rack* to spare space on the table. Electrical components that produce heat and vibration are housed outside in computing hardware racks called the *electrical racks*. We built the racks reduce the apparatus footprint, increase modularity, isolate the ion trap from heat and vibration produced by the electrical components, and keep the components without entering the AHU to minimize potential radiation exposure (Figure 3.1b). A system of *patch panels* and cable assemblies provides the interface and connections between the control system, electrical subsystems in the racks, and the components in the AHU (Figures 3.1c, 3.1d). Signals are tapped and routed back to the control station as much as possible to allow performance monitoring in the near term and real-time stabilization in the long term. Generally, electrical control signals originate in electrical rack 1, are modified in electrical rack 2, then pass through the patch panels in the AHU wall to the component of interest housed either in the optics rack or on the optics table (Figure 3.2). The systems described

in this chapter are designed and assembled to conform with this pattern, with the exception of some standalone systems.

(a) AHU2.

(b) Electrical racks.

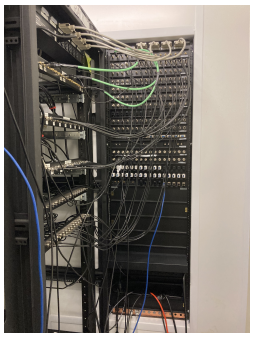

(c) AHU, external.

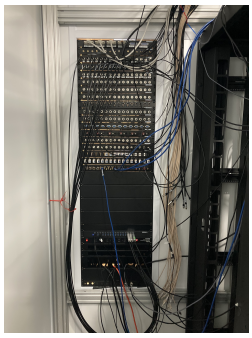

(d) AHU, internal.

Figure 3.1: Photographs of the physical infrastructure for the apparatus. 3.1a The optics table, optics rack, and vacuum chamber are held in the AHU. 3.1b Electrical circuits for the control system are largely held in server racks. 3.1c Patch panels in the AHU wall and electrical racks provide a modular interface between different sections of the electrical circuits. 3.1d Patch panel interface inside the AHU wall. Cables lead to components in the optics rack or optics table.

We use custom breakout printed circuit boards (PCBs) in multiple electrical subsystems in the QuantumIon apparatus. Custom PCBs have multiple attractive properties. For simple circuits, they are easy and cheap to design, fabricate, and assemble. They can be built to our precise requirements, and can implement circuits reliably and compactly.

Section 3.1 describes the radio frequency and direct current channels for controlling the Phoenix surface trap [93]. The lasers and circuits driving the active optics and controllers for passive optics are detailed in Section 3.2. Section 3.3 concerns the circuits for the ion detection systems. The circuits connecting the current source to the magnetic field coils and a summary of the vacuum chamber system are presented in Sections 3.4 and 3.5, respectively. Finally, Section 3.6 reports the current assembly status of the electrical subsystems

3.1 Ion Trap

The ion trap is the component that produces the electric potential well that spatially confines the atomic ions as described in Section 2.3. It is housed inside the vacuum chamber

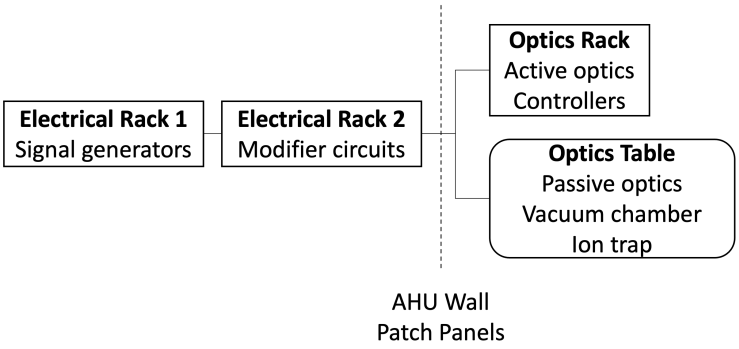

Figure 3.2: Diagram of the general form of electrical control circuits in the QuantumIon apparatus (not to scale). Signals are generated in electrical rack 1, modified in electrical rack 2, pass through the patch panels in the AHU wall, then connect to components in the optics rack or on the optics table (left to right on the diagram). Each rack contains drawers with patch panel interfaces.

(Section 3.5). Our apparatus uses the Phoenix trap [93], a microfabricated surface trap designed and fabricated by Sandia National Laboratories[1]. The trap produces radial confinement with an radio-frequency (RF) electric pseudopotential produced by large RF rail electrodes and axial confinement with direct current (DC) potentials generated by a set of small electrodes arrayed along the trap axis (Figure 3.3).

3.1.1 RF Pseudopotential Circuit

As discussed in Section 2.3, a charged particle cannot be confined in 3D space with solely static fields. The Phoenix trap radially confines ions with a rapidly alternating electric field, which generates a time-averaged confining potential, known as a pseudopotential, that traps the ion with some residual micromotion. The radial confinement is much stronger than the axial confinement, resulting in a linear chain of ions.

The frequency of the pseudopotential chosen to trap $^{133}Ba^{+}$ is $\omega_{rf} \approx 2\pi \times 44$ MHz, which is in the RF spectrum. The Phoenix trap is a capacitive load for both RF and DC, which means the driving signals should have minimal current while hitting the target frequency and voltage. The trap can tolerate an RF signal with up to $V_{max} \approx 250$ V voltage amplitude. We select a voltage of $V_{rf} = 200$ V to operate at 80% of the traps maximal rating, giving adequate room for safety. Finally, the signals should have minimal frequency

[1] https://www.sandia.gov/quantum/trapped-ions/

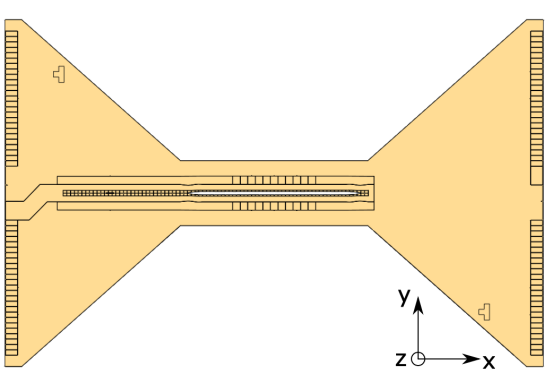

(a) Diagram of the Phoenix trap [93].

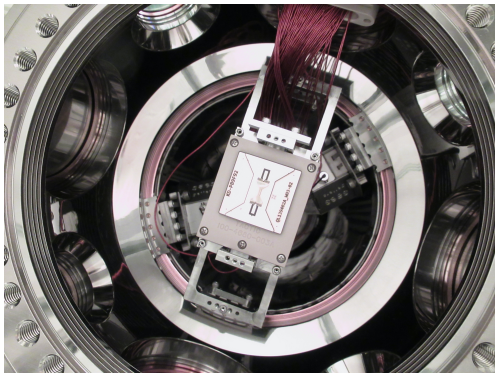

(b) Trap in the vacuum chamber.

Figure 3.3: Diagram (left) and photograph (right) of the Phoenix trap. The small rectangles on the horizontal axis of the trap are individual DC electrodes. The RF and ground rails run between the smaller inner DC electrodes and the larger outer DC electrodes.

noise to avoid unintentional deformations of the trapping potential and perturbations of the ion motion. The performance requirements of the RF pseudopotential driving signal are summarized in Table 3.1.

Parameter	**Value**
Trapping frequency (f_t)	≈ 44 MHz
Drive voltage (V_{amp})	200 V

Table 3.1: Parameters for the RF signal driving the radial trapping pseudopotential.

The RF electrical signal driving the circuit is generated by Sinara 4410 DDS "Urukul" card from M-Labs[2] [56, 61] as part of our real-time control hardware system (Section 4.1). The card is a four-channel direct digital synthesizer (DDS) that generates a single pure sinusoidal electrical RF signal with real-time frequency, power, and phase control per channel. It generates frequencies in the range $f = 1 - 400$ MHz with maximum power $P_{max} = 10$ dBm. The circuit that connects the DDS to the trap must avoid introducing frequency noise, prevent damage to all components in the circuit (especially the trap!), and be housed in an electrical rack drawer or shelf with a modular patch panel system.

The trap RF drive circuit is composed of an RF amplifier, a bidirectional coupler, a power supply unit (PSU), RF power attenuators, and a resonator, all connected by low-loss

[2] https://github.com/sinara-hw/Urukul/wiki

RF cable assemblies and connector adapters. All components and cable assemblies use subminiature version A (SMA)[3], Bayonet Neill–Concelman (BNC)[4], or type-N connectors[5], all of which are appropriate for the trap RF drive frequency. The amplifier, bidirectional coupler, PSU, and attenuator all reside in an electrical rack drawer with circuits driving the acousto-optic modulators (AOMs) (Section 3.2.4). The resonator is located on the optical table inside the AHU directly adjacent to the vacuum chamber. Figure 3.4 shows a diagram of the trap RF drive circuit and Figure 3.5 is a photograph of the as-built circuit. A component manifest for the trap RF drive circuit is presented in Table 3.2.

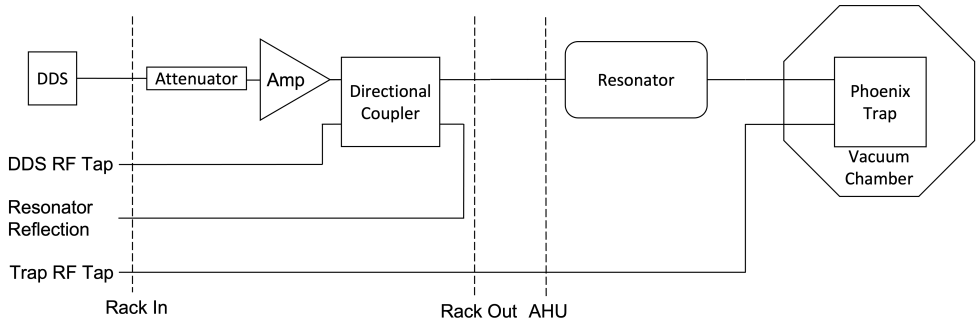

Figure 3.4: Diagram of the trap RF drive electrical circuit (not to scale). The drive signal passes from left to right, while the tapped signals pass from right to left. Vertical dotted lines represent patch panels. A full electrical schematic of the circuit can be found in Appendix E.

The Urukul DDS is housed in an electrical rack outside of the AHU. Over 6 m of cable is required to connect the DDS to the resonator. Even with low-loss RF cables, the RF signal must be amplified to reach the trap at the required power. The Mini-Circuits ZHL-5W-1+ RF power amplifier[6] provides 40 dB of amplification and draws $P \approx 80$ W of power from the PSU. It is fan-cooled.

The Mini-Circuits ZFBDC20-62HP-S+ bidirectional coupler[7] taps a fraction (-20 dB) of both the signal emitted from the amplifier and the signal back-reflected from the resonator. Tapping both signals is necessary to monitor the performance of the input RF signal and the resonator itself. Both tapped signals are routed back to the patch panel on the front of the electrical rack.

[3] https://www.amphenolrf.com/connectors/sma-connectors.html
[4] https://www.amphenolrf.com/connectors/bnc-connectors.html
[5] https://www.amphenolrf.com/connectors/n-type-connectors.html
[6] https://www.minicircuits.com/WebStore/dashboard.html?model=ZHL-5W-1%2B
[7] https://www.minicircuits.com/WebStore/dashboard.html?model=ZFBDC20-62HP-S%2B

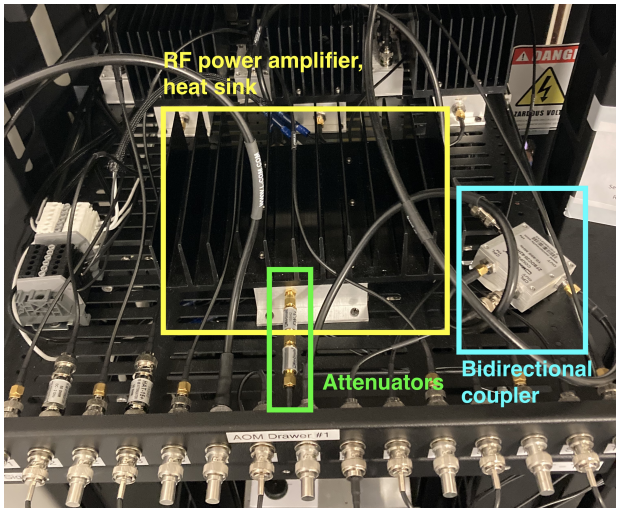

Figure 3.5: Photograph of the as-built electrical circuit carrying the RF signal for the trapping RF pseudopotential to the trap. The drawer also contains RF circuits for driving the AOMs (Section 3.2.4).

The Acopian Model W24GT50 PSU[8] (Figure 3.6) provides DC power to the RF amplifier. It supplies up to $I = 50\ A$ of current at $V_{DC} = 24$ V. It is a switching PSU that risks introducing some switching noise into the signal. The benefit of a switching PSU is that it is smaller than the alternative, a linear PSU. Choosing a smaller PSU allows us to place the PSU in a rack drawer and simplify power routing. We have found that the PSU introduces minimal noise and that the resonator filters the signal adequately.

The Mini-Circuits FW-3+[9] and FW-10+ RF power attenuators[10] limit the RF power in the circuit to avoid component damage. They protect all components against the maximum power output from the Urukul and the amplifier. Excessive power can damage circuit components. Components vulnerable to damage are the amplifier, bidirectional coupler, resonator, and trap. The amplifier has no power control and operates at full strength when powered, but the Urukul DDS has power control. The attenuator is situated between the Urukul DDS and the RF power amplifier to limit the input power to the amplifier and attenuate the signal at lower input power to preserve the RF power attenuator.

Low-loss RF coaxial cable assemblies are used to connect all components in the circuit.

[8] https://www.acopian.com/store/productdetail.aspx?q=i1363
[9] https://www.minicircuits.com/WebStore/dashboard.html?model=FW-3%2B
[10] https://www.minicircuits.com/WebStore/dashboard.html?model=FW-10%2B

Component	Gain (dB)	Insertion Loss (dB)
ZHL-5W-1+ RF power amplifier	40	-
ZFBDC20-62HP-S+ bidirectional coupler	-	0.1
FW-10+ RF power attenuator	-	10
FW-3+ RF power attenuator	-	3
Resonator (custom)	≈ 30	-
SMA connector	-	0.2
BNC connector	-	0.27
Type-N connector	-	0.15
LMR-100A cable	-	5.1 (per 100 ft.)
LMR-195 cable	-	2.5 (per 100 ft.)
LMR-240 cable	-	1.5 (per 100 ft.)

Table 3.2: RF power performance of the components in the circuits for driving the trap RF drive circuit at ≈ 44 MHz.

The cable assemblies used are LMR-100A[11], LMR-195[12], and LMR-240[13] from Times Microwave Systems, in descending order of lossiness. The lower-loss cable assemblies are used for longer cable runs.

Resonator

The resonator is a curious device akin to a transformer that acts as a combination high *slew rate* voltage amplifier and low bandwidth band-pass filter [34, 72, 107]. Ion traps require high voltage, low current RF signals to produce RF pseudopotentials. Traditional RF power amplifiers do not provide sufficient voltage slew rates and often emit excessive current. The resonator amplifies the voltage of the resonant frequency of the device while suppressing all other frequencies. This has the advantage of passing a pure tone RF signal to the trap, which improves trap performance.

The resonator in this apparatus is a copper helical resonator (Figure 3.7). It consists of small input copper coil and a larger output copper coil, both grounded to a cylindrical copper shell. The input coil is connected to the RF circuit described above. The output coil is connected directly to the Phoenix trap RF input via the vacuum chamber feedthrough (Figure 3.7d).

[11] https://timesmicrowave.com/cables/lmr-100-pur-coax-cable/
[12] https://timesmicrowave.com/cables/lmr-195-coax-cable/
[13] https://timesmicrowave.com/cables/lmr-240-coax-cable/

Figure 3.6: The PSU for the trap RF drive circuit power amplifier. The same PSU also supplies power for the AOM RF drive circuit power amplifiers (Section 3.2.4).

Resonators are not commercially available components. The resonator used in the lab was custom designed and assembled in-house. It has an as-measured loaded resonant frequency of $f_{res} \approx 36$ MHz, which does not match our target drive frequency of $f_{rf} \approx 44$ MHz. Therefore, we intend to redesign and rebuild the resonator to achieve the desired resonant frequency. The resonator design and performance parameters are summarized Table 3.3. For more discussion of the resonator in this apparatus, see [10] (note that the resonator has been slightly modified since the writing of that thesis).

Parameter	**As-Designed**	**As-Built**
Resonant frequency, loaded f_{res}	≈ 44 MHz	≈ 36 MHz
Resonant frequency, unloaded f_u	≈ 80 MHz	≈ 46 MHz
Q-factor (loaded) Q	-	200

Table 3.3: Summary of as-designed and as-built resonator performance.

3.1.2 DC Confinement Circuits

DC electrodes provide axial confinement to ions in the trap by generating a static electric potential well. Traditional RF Paul traps use two end-cap electrodes, one at each end of the trap, for bulk control over the potential well. The Phoenix trap, however, has 96 individual electrodes: 74 inner confinement electrodes, each 70 μm wide, and 22 outer compensation electrodes, each 140 μm wide. The electrodes are arrayed along the axis of the trap [93]. Each electrode can have a different voltage individually applied to it, enabling

(a) Assembled.

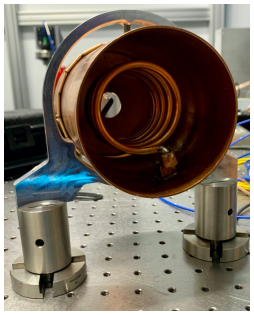

(b) Main chamber with large coil.

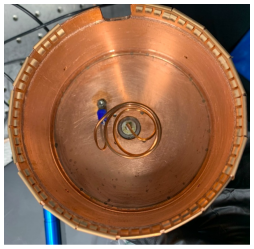

(c) Resonator end-cap with small coil.

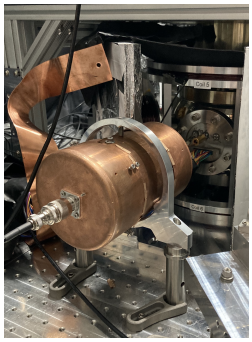

(d) Connected to vacuum chamber.

Figure 3.7: Photographs of the as-built resonator for the trap RF drive electrical circuit.

fine control over the shape and depth of the axial electric potential well. This feature provides additional capability to the ion trap such as sculpting anharmonic potentials [51, 68] and shuttling ions to different spatial regions of the trap [76, 86, 88].

The electrodes are a capacitive load with a $\Delta V_{max} = 20$ V voltage limit between electrodes before risking arcing. Thus, the maximum voltage allowed on each electrode is $V_{max} = \pm 10$ V. Suppressing frequency noise improves the performance of trapping, shuttling, and quantum operations. A lower filter limit would increase signal stability, but limits the shuttling speed. The requirements for the circuits driving the trap DC electrodes are summarized in Table 3.4.

Parameter	**Value**
Maximum voltage V_{max}	± 10 V
Frequency noise threshold w_{RC}	<= 125 kHz

Table 3.4: Parameters for the DC signals driving the trapping axial confirming potential.

The DC electrical signals driving the electrode circuits are generated by three Sinara 5432 DAC "Zotino" cards from M-Labs[14] [61] as part of the real-time control hardware system (Section 4.1.1). The card is a 32-channel digital-to-analog converter (DAC). It generates voltages in the range $V = \pm 10$ V. Thus, the DC circuits that connect the Zotino card to the Phoenix trap must deliver the generated voltages without introducing frequency noise and while preventing damage to the trap. The circuit must also be housed in an electrical rack drawer or shelf with a modular patch panel system.

[14] https://github.com/sinara-hw/Zotino/wiki

The Zotino DAC card uses an unusual high-density connector, the high-density 68-pin (HD68) connector typically used in Small Computer System Interface (SCSI) systems. The vacuum chamber feedthrough uses a different, but also unusual, D-sub-miniature double density 100-pin (DD100) connector. Both connectors accommodate the large number of individual DC electrodes on the Phoenix trap. Since the two connectors are incompatible, conversion between the two connector types is required. We chose to convert to an intermediate connector type, D-sub-miniature 25-pin (DB25), to take advantage of reliable, commercially available cable assemblies and panel-mount connectors that use that connector form factor for the long cable run between the RF signal source and the trap. Therefore, we designed breakout PCBs to convert between the three types of connectors.

The components of the circuits that deliver DC signals to the Phoenix trap electrodes are a custom PCB that converts from HD68 to DB25 connectors, a custom PCB that converts from DB25 to DD100 connectors and implements low-pass filters and voltage limiters, the vacuum feedthrough, and the wire harness and zero insertion force (ZIF) socket inside the vacuum chamber that connect to the ceramic pin-grid array package (CPGA) that holds the Phoenix trap. The circuit components are connected by several HD68 cable assemblies, DB25 cable assemblies, and a DD100 cable assembly. See Figure 3.8 for a diagram of the trap DC electrodes circuits.

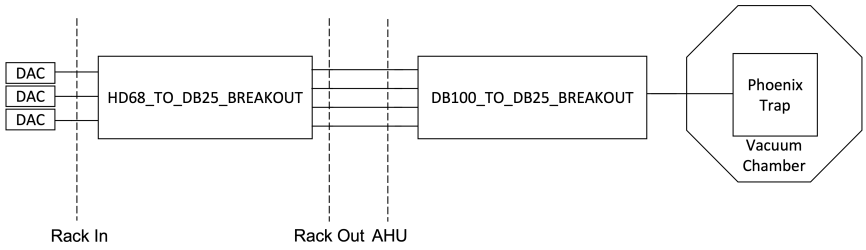

Figure 3.8: Diagram of the trap DC electrodes electrical circuit (not to scale). The drive signal passes from left to right. A full electrical schematic of the circuit can be found in Appendix E.

HD68_TO_DB25_BREAKOUT PCB

Commercially available long cable assemblies (> 6 m) and panel-mount connectors for the HD68 connector are not readily available. Additionally, since the Zotino DAC emits 32 voltages as single-ended voltages from just 32 pins on the connector, the HD68 connector is not appropriate for the fully circuit connecting the Zotino DAC to the Phoenix trap DC

electrodes. An alternative connector, the DB25, has long cable assemblies and panel-mount connectors commercially available. Thus, we selected an collection of four DB25 cables to carry the voltages to the trap. Each cable carries 24 signal channels and one ground channel for a total of 96 signal channels and four ground channels, exactly as required for the Phoenix trap.

We designed and assembled a custom breakout PCB that converts from three HD68 connectors to four DB25 connectors (Figure 3.9). The unused pins in the HD68 connector are connected to ground. No other circuit elements are present in the circuit because it simply converts from one connector form factor to another without modifying the signals. We call this PCB the *HD68_TO_DB25_BREAKOUT* board.

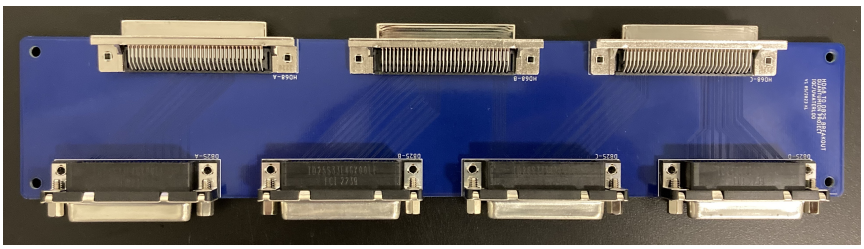

Figure 3.9: Photograph of the *HD68_TO_DB25_BREAKOUT* PCB. The three connectors at the top are HD68 connectors. The four connectors at the bottom are DB25 connectors. No other components are in the circuit. A full drawing for this PCB may be found in Appendix F.

DD100_TO_DB25_BREAKOUT PCB

Similar to the case of the HD68 connector described previously, cable assemblies and panel-mount connectors using the DD100 form factor are not readily commercially available. This contributes to the choice to use the intermediate DB25 connectors and cable assemblies for the long cable run between the real-time control system and the vacuum chamber. Therefore, another PCB is required to convert between the DB25 and DD100 connectors.

The custom PCB that performs this conversion also includes low-pass filters and voltage limiter circuits on each channel to reduce electrical field noise and protect the trap from damage from excessive voltage. We call this PCB the *DD100_TO_DB25_BREAKOUT* board.

Frequency noise on the trap electrodes introduces noise into the confining electric potential. The noise can cause ions to heat up, reducing the performance of quantum operations

and potentially exciting the ion out of the confining potential altogether. Low-pass filter circuits and a common-mode choke (CMC) remove noise from circuits.

However, shuttling ions between different regions of the trap requires changing the voltages on the electrodes. Fast shuttling can require quick changes to the voltages. Thus, an excessively strict low-pass filter can limit the ability to shuttle ions. The current goal of the project is to trap the first ions in static confinement. Shuttling is a future goal. Therefore, designing the filter to permit future shuttling performance is desirable, but not required.

The current design of the *DD100_TO_DB25_BREAKOUT* PCB borrows from the Zotino DAC. It implements low-pass filters with a cutoff frequency of $\omega = 125$ kHz using a simple resistor-capacitor (RC) circuit. A CMC with inductance $L = 6.5$ MH protects against electromagnetic noise.

As stated previously, voltage difference of $\Delta V_{max} = 20$ V between electrodes can damage the trap. Therefore, the *DD100_TO_DB25_BREAKOUT* board implements voltage limiters limiting each channel to $V_{max} = \pm 10$ V. A voltage limiter is a circuit that limits the output of the circuit to a voltage below a threshold value. The voltage limiters on the *DD100_TO_DB25_BREAKOUT* PCB are implemented with Zener diodes with cutoff voltages of $V_Z = 9.1$ V. The diodes permit signals with voltage of the cutoff voltage plus some bias voltage amount to propagate through. With a bias voltage of $V_{bias} = 0.7$ V, signals with voltages up to $V = \pm(V_Z + V_{bias}) = \pm(9.1\ V + 0.7\ V) = \pm 9.8$ V pass through to the trap DC electrodes. Signals with higher voltages are suppressed. The *DD100_TO_DB25_BREAKOUT* board has 96 low-pass filter and voltage limiter circuits, one per signal channel. The ground channels do not have any circuit elements. See Figure 3.10 for a schematic of the circuits on the *DD100_TO_DB25_BREAKOUT* PCB. The design of the PCB is still under development.

Connection to the Trap

A feedthrough system in the vacuum chamber connects the RF and DC circuits to the circuits connecting to the trap inside of the vacuum chamber (Figure 3.11). The feedthrough consists of a DD100 connector and three sets of four conducting pins. An internal wiring harness connects the pins from the DD100 connector and two of the conducting pins to a set of 102 wires connected to a ZIF socket. The ZIF socket connects to the CPGA package that carries the Phoenix trap [93]. 96 of the wires carry the DC trapping voltages and four are ground wires from the DD100 connector. Of the remaining two wires, one carries the

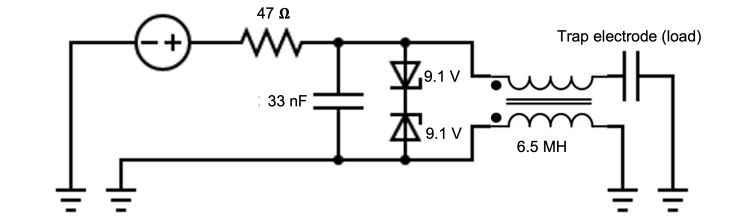

Figure 3.10: Diagram of the electrical circuits on the *DD100_TO_DB25_BREAKOUT* PCB (not to scale). From left to right: voltage source, low-pass filter, voltage limiter, CMC, and load elements. The low-pass filter is implemented as an RC circuit with cutoff frequency $\omega = 1/2\pi RC = 125$ kHz. The voltage limiter is implemented with Zener diodes in both positive and negative voltage orientations. The CMC protects against electromagnetic noise. 96 of the above circuit are on the *DD100_TO_DB25_BREAKOUT* PCB, one for each trap DC electrode channel.

RF trapping signal and one carries the RF pick-off from the trap back to the feedthrough for monitoring.

3.2 Lasers

As discussed in Sections 2.4 and 2.5, operations on trapped ion qubits are accomplished by exposing the trapped ions to laser light with precisely controlled frequencies, intensities, and phases for exact periods of time. Additionally, we use laser light to ablate an atomic source and photoionize the resulting plume of atoms to produce ions to trap. The laser light is generated and modified by components that are operated and controlled by electric hardware and circuits. The lasers currently implemented in the QuantumIon apparatus are 532 nm for ablation, 389 nm and 554 nm for REMPI, 493 nm for Doppler cooling and SPAM, and 650 nm for repumping.

The orientation of the laser beams in the apparatus relative to the trap and magnetic field are displayed in Figure 3.12. The 493 nm beam used for Doppler cooling and measurement laser and 650 nm repump laser are aligned on the same beam path. The optical pumping beam is orthogonal to the cooling and measurement beam. Both beam paths are orientated at angles to the magnetic field in the apparatus that provide photons with π, σ_+, and σ_- polarization components required to drive transitions from all of the necessary

Figure 3.11: Photograph of the electrical feedthrough in the vacuum chamber. The feedthrough is in the place of an optical viewport. The DD100 connector connects to the wires leading to the Phoenix trap DC electrode signal and ground pins. A barrel connector (not shown) on an unoccupied pin connects the resonator to the trap RF circuit. The pin connected to the alligator clip connects to the trap RF pick-off that enables monitoring of the RF signal on the trap.

degenerate states in the $F = 1$ and $F = 2$ energy levels of the ground and metastable states.

Implementation of quantum information processing capabilities will require additional lasers at different frequencies. 1762 nm and 614 nm CW lasers will be used for shelving and shelving repump transitions, respectively. Single- and multi-qubit quantum operations will be implemented with a pulsed 532 nm laser. These lasers and the transitions they drive are beyond the scope of this thesis. For more discussion of the optical design of the apparatus, see [10, 47, 120].

3.2.1 Generation and Control

The devices that emit narrow bandwidth coherent laser light are called laser *heads*. Laser heads are often paired with *controllers* that monitor and tune the head to control the precise frequency of the emitted light.

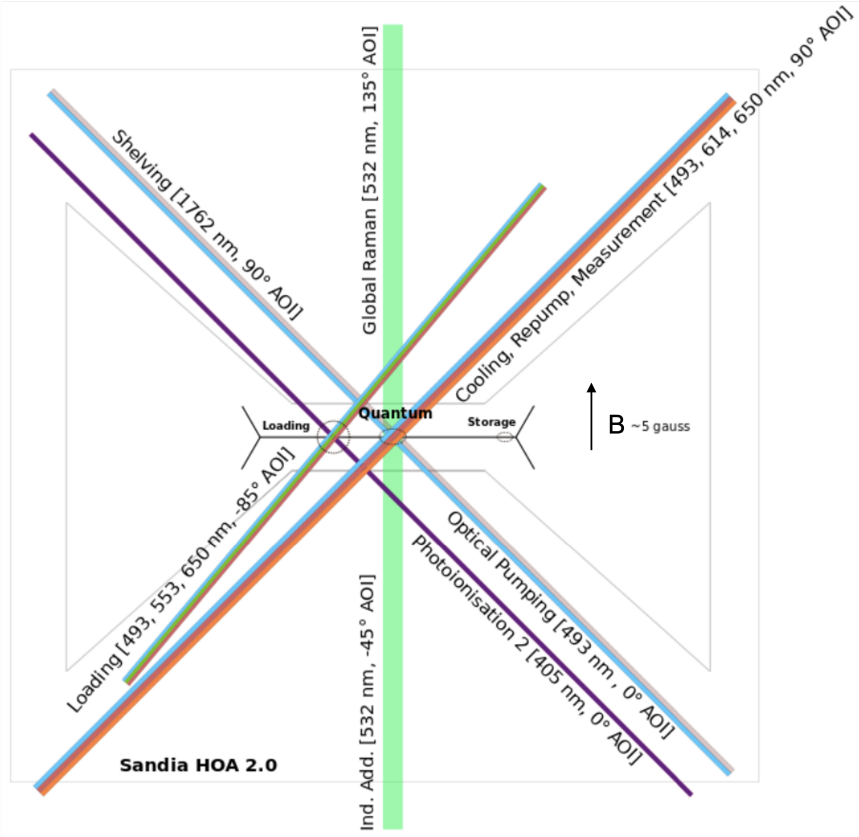

Figure 3.12: Diagram of the orientation of the planned laser beams relative to the surface trap in the QuantumIon apparatus [47]. The direction of the magnetic field is indicated with a vector. Laser beams are carefully oriented with respect to the magnetic field so that the photons have the appropriate polarizations for the required operations. Cooling lasers are also oriented to cool along both radial and axial directions. The 405 nm beam has been replaced with a 389 nm beam. The 532 nm Raman beams are not implemented. The 532 nm ablation laser is not shown. The *quantum zone* in the center is the primary locus of ion trapping and quantum operations. The *loading zone* to the side is an optional secondary region where ions may loaded without interfering with ions in the quantum zone and later shuttled to the quantum zone. All implemented lasers currently are aligned to the quantum zone.

The 493 nm, 650 nm, and 1107 nm lasers are all controlled by AOSense Integrated

Laser Controller and Servo (SILC) units[15]. The 389 nm laser is controlled by a MOGLabs Diode Laser Controller (DLC). The 532 nm ablation laser is triggered by a digital input signal from the real-time control signal (Section 4.1). Figure 3.13 shows the controllers for the lasers.

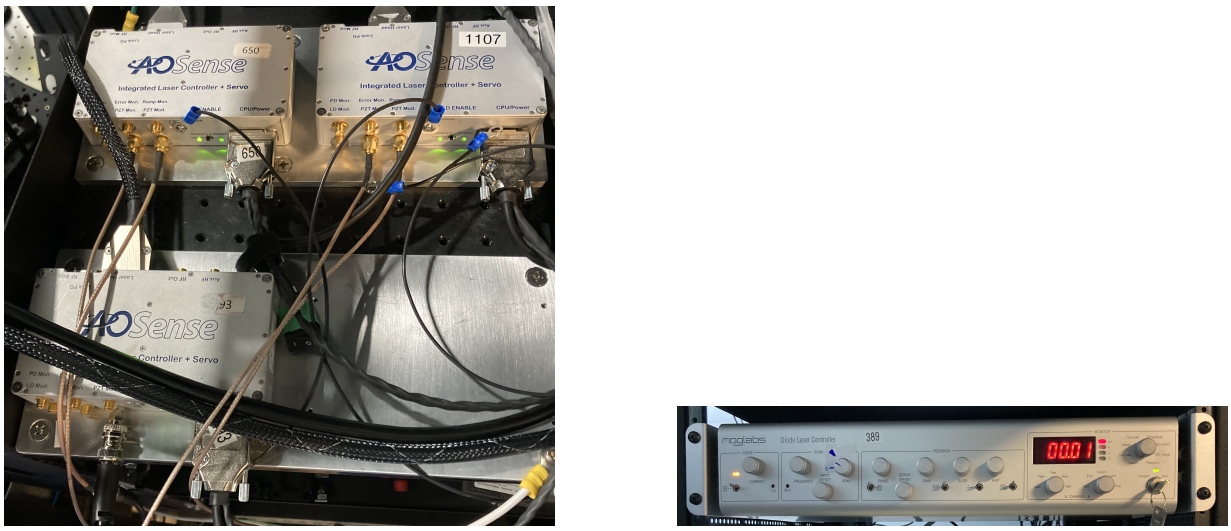

(a) AOSense SILC.

(b) MOGLabs DLC.

Figure 3.13: Photograph of the controllers for some CW lasers in the QuantumIon apparatus. 3.13a The AOSense SILC for the 493 nm, 650 nm, and 1107 nm lasers. 3.13b The MOGLabs DLC for the 389 nm laser.

All of the laser heads in the apparatus are located on the optics table for stability while locking the emission frequency. Later, the heads and beam preparation components will be moved to the optics rack to preserve space on the optical table. All laser controllers are mounted in the optics rack.

Laser heads and controllers do not interact directly with the quantum control system and always remain on and operational. In many cases, the controllers have independent control systems. The laser components are standalone systems that do not require additional electrical circuits to support them. The controllers indirectly interact with the control system via the wavemeter (Section 3.2.2). The laser heads and controllers are always operational while the apparatus is in use.

[15] https://aosense.com/products/electronics/integrated-laser-controller-servo/

3.2.2 Frequency Locking

Both the lasers and the energy level transitions in barium ions that they target have narrow linewidths. Quantum control requires that the frequency of all lasers that interact with ions remain as stable as possible. Frequency control is accomplished by a process called *locking*: activate feedback and control of the laser head enabled by precise measurement of the emitted light. The key component is the wavelength meter, colloquially known as the *wavemeter*, which performs the precise frequency measurement.

Wavemeter

The wavemeter in the QuantumIon apparatus is a HighFinesse WS8-2[16] (Figure 3.14). It can measure the frequency of laser light in the range $330 - 1180$ nm to 200 kHz frequency precision. The wavemeter then sends commands to the laser controllers based on the difference between the measured and desired laser frequencies. The wavemeter currently implements frequency locking for the 389 nm, 493 nm, 650 nm, and 1107 nm lasers.

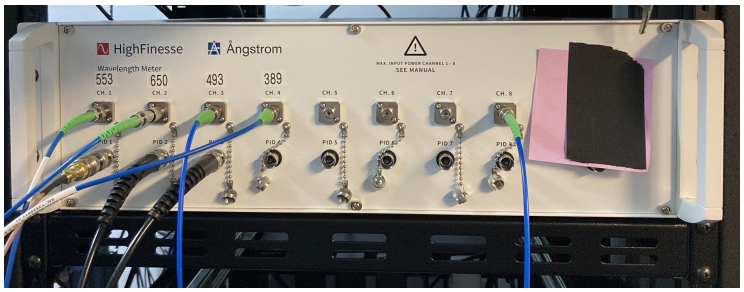

Figure 3.14: Photograph of the HighFinesse WS8-2 wavemeter.

The WS8-2 wavemeter is a peripheral component which receives non-real-time commands from the control system (Section 4.2.2). Computer control occurs via a Python wrapper over a vendor-supplied precompiled C library. The current control implementation is a Python package that solely offers a class that wraps the control library. Future implementation will control the wavemeter as a Network Device Support Package (NDSP), a format that better integrates with the ARTIQ control system (Section 4.2.1).

The wavemeter is a standalone component that does not require support from additional electrical circuits. It sits in the optics rack and is connected to the application server via Universal Serial Bus (USB). In addition to our fully-integrated control system, the

[16] https://www.highfinesse.com/en/wavelengthmeter/wavelengthmeter-ws-8-2.html

wavemeter has its own control application. The wavemeter is always operational while the apparatus is in use.

3.2.3 Frequency Doublers

A frequency doubler is an optical frequency multiplier that emits laser light at twice the frequency of the light that enters the component. The QuantumIon system uses a NTT Electronics WH-0554-000-F-B-C periodically poled lithium niobate (PPLN) frequency doubler[17] (Figure 3.15) with a Wavelength Electronics Model LFI-3751 temperature controller[18] (Figure 3.16). The temperature of the doubler must be controlled to stabilize the emitted light frequency. The doubler temperature controller is a standalone system that does not require additional electrical circuits. It is always operational while the apparatus is in use. The doubler temperature controller is currently held in the optics rack. In the future, it will be moved to an electrical rack.

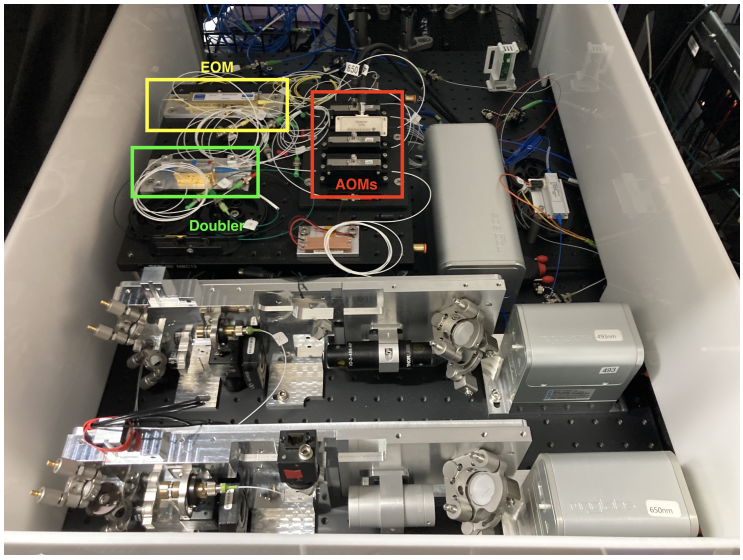

Figure 3.15: Photograph of select beam preparation optics for the 493 nm, 650 nm, and 1107 nm. The doublers and modulators are outlined. The grey laser heads and some passive optics are also visible.

[17] https://www.ntt-electronics.com/en/sensing_application/ppln_wavelength_conversion.html

[18] https://www.teamwavelength.com/product/lfi3751-5a-digital-temperature-control-instrument/

Figure 3.16: Photograph of the temperature controller for the doubler for the 1107 nm laser. Emitted light frequency stability depends on the stability of the doubler temperature.

3.2.4 Frequency Modulation

As discussed in Sections 2.4 and 2.5, the specific hyperfine energy levels that must be targeted for Doppler cooling and SPAM should have differences in transition energies that enable specific transitions to be selectively driven. Additionally, the transition energies are greater than the linewidths of the lasers in the apparatus. Therefore, different frequency sidebands of laser light must be generated to drive all of the transitions of interest. Rather than add additional lasers to the apparatus that are tuned to target the frequency sidebands of interest, we use optical components to *modulate* the laser light. The optical modulators in the apparatus are acousto-optic modulators (AOMs), which we use as ultrafast optical switches, and electro-optic modulators (EOMs), which modulate laser to drive specific transitions in the ions. For details on the behavior of AOMs and EOMs, see [21].

Acousto-Optic Modulators

Acousto-optic modulators (AOMs) are active optical components that map the wave characteristics of an RF signal on to an optical signal. Light that interacts with the driven AOM is diffracted with a shift in the frequency, phase, and amplitude. The diffraction angle is proportional to the wavelength of light and the frequency of the RF drive signal. The fre-

quency, phase, and intensity shifts of the diffracted light are proportional to the frequency, phase, and power of the RF drive signal, respectively. If the AOM is not driven, it is still and the light passes through the crystal undiffracted and unmodulated. The frequency of the light diffracted from the AOM is *shifted* with no light at the original frequency emitted along the diffracted beam path. The frequency shift must be accounted for when tuning laser frequencies, but may be neglected when calculating modulation frequencies applied by the EOMs because the shift is applied uniformly to all light beams.

In the QuantumIon apparatus, we leverage the controllable diffraction in the AOMs to implement ultra-fast switches for the laser beams. Fast switching for operations is important because some of the energy levels of $^{133}Ba^{+}$ have very short lifetimes and fast switching enables more operations within the coherence time of the qubit. The laser beam paths in the apparatus are aligned such that the diffracted beam interacts with the ions, while the unaffected beam goes to a beam stop. Thus, lasers beams enter the vacuum chamber and interact with the ions only when the AOM is driven by an RF signal. Since the rise/fall time of an RF synthesizer can be several orders of magnitude faster than a mechanical shutter ($< 1\ \mu s$ vs. $\approx 1\ ms$ for common components), the AOM acts as an extremely fast switch.

The design for the QuantumIon apparatus calls for AOMs as switches for all CW laser beams and on each channel of the individual addressing Raman interaction system. The AOMs in the individual addressing system are required for modulating light to drive entangling operations on qubits. Discussion of entangling operations is beyond the scope of this thesis. For details on the individual addressing system, see [9]. This section will focus on the requirements for the electrical circuits that drive the AOMs that act as switches, though similar circuits will also drive the AOMs in the individual addressing system.

The AOMs used in the QuantumIon apparatus for CW lasers are Gooch and Housego T-M200-0.4C2A-3-F2P[19] and S-M200-0.4C2E-3-F2P[20] AOMs tuned to 493 nm and 650 nm light, respectively (Figure 3.15). Additional AOMs support 554 nm light for photoionization and 614 nm light for the shelving repump operation, which is beyond the scope of this thesis. The eight AOMs specified to act as switches for CW laser beams in the final system design are shown in Table 3.5.

While the initial trapping experiments only requires two AOMs (one each for the 493 nm and 650 nm laser beams), we built the electrical circuits required to drive all of the CW

[19] https://gandh.com/products/fiber-optics/fiber-q-fiber-coupled-modulators/fiber-q-450-nm-200-mhz

[20] https://gandh.com/products/fiber-optics/fiber-q-fiber-coupled-modulators/fiber-q-633-nm-200-mhz-fiber-coupled-aom

Component	Laser (nm)	Purpose
T-M200-0.4C2A-3-F2P	493	Ion loading Cooling, repump, measurement Optical pumping
S-M200-0.4C2E-3-F2P-02	650	Ion loading Cooling, repump, measurement Micromotion detection
S-M200-0.4C2C-3-F2P-01 S-M200-0.4C2E-3-F2P-02	554 614	Photoionization Shelving repump

Table 3.5: AOMs used to implement fast on/off switching of laser beams in the QuantumIon apparatus. All AOMs are driven with an RF signal at frequency $f = 200$ MHz.

AOMs plus three extra channels (11 total), two for the eventual 532 nm Raman laser beams and one extra because an extra RF synthesizer channel was available (Section 4.1.1). The 554 nm AOM is not immediately required because 554 nm is not resonant with ion transitions (only neutral atomic transitions), so the light will not cause problems for the ions if it is not turned off quickly. The circuits all fit in two electrical rack drawers, and the minimal labor required to install the additional channels is worth the ability to quickly expand the capabilities of the apparatus once we have trapped the first ions.

All of the AOMs in the QuantumIon apparatus operate at 200 MHz and have a maximum input RF power threshold of $P_{max} = 1$ W $= 30$ dBm. Therefore, the circuits that drive AOMs must satisfy those requirements (summarized in Table 3.6). They should also avoid introducing frequency noise into the signal. The circuits must fit into electrical rack drawers and be connected to the signal source and the AOMs via a system of cable assemblies and patch panels.

Parameter	Value
Frequency f	200 MHz
Maximum power P_{max}	1 W = 30 dBm

Table 3.6: Summary of the electrical requirements for the RF circuits that deliver the RF drive signal to the AOMs in the apparatus.

The electrical circuits that drive the AOMs are all identical to each other and are similar to the circuit that drives the trap RF drive signal (Section 3.1.1). The AOM circuits are also driven by a Sinara Urukul DDS card. The rest of the circuits each consist of an amplifier, a directional coupler, RF power attenuators, a PSU, and low-loss coaxial

cable assemblies of a variety of lengths. All components and cable assemblies use SMA and/or BNC connectors. All of the electrical components reside in the electrical rack in two drawers. One drawer contains six circuits and the trap RF signal drive circuit. The other contains five circuits and the PSU. The AOMs driven by the circuits will eventually be housed in an optical rack inside the AHU. Currently, they are mounted on the optical table. Figure 3.17 shows a diagram of an AOM RF drive circuit and Figure 3.18 displays photographs of the as-built circuits. A component manifest for each AOM RF circuit is presented in Table 3.7.

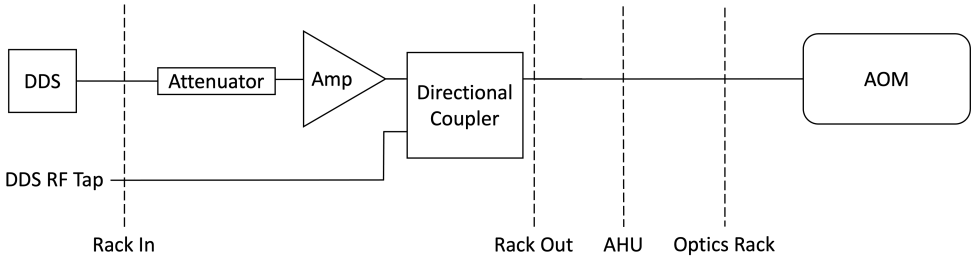

Figure 3.17: Diagram of the AOM RF drive electrical circuit (not to scale). The drive signal passes from left to right, while the tapped signals pass from right to left. Vertical dotted lines represent patch panels. A full electrical schematic of the circuit can be found in Appendix E.

Component	Gain (dB)	Insertion Loss (dB)
ZHL-03-5WFX+ RF power amplifier	30	-
ZDC-20-1+ directional coupler	-	0.1
HAT-15+ RF power attenuator	-	10
SMA connector	-	0.2
BNC connector	-	0.27
LMR-100A cable	-	10.9 (per 100 ft.)
LMR-240 cable	-	3.7 (per 100 ft.)

Table 3.7: RF power performance of the components in the circuits for driving the AOM RF drive switching signal at $f = 200$ MHz.

The Mini-Circuits ZHL-03-5WFX+ RF power amplifier[21] provides 30 dB of gain to account for signal attenuation over the > 6 m of coaxial cable that connects the Urukul to the AOMs. It is fan-cooled and draws $P \approx 67$ W of power from the same Acopian

[21] https://www.minicircuits.com/WebStore/dashboard.html?model=ZHL-03-5WFX%2B

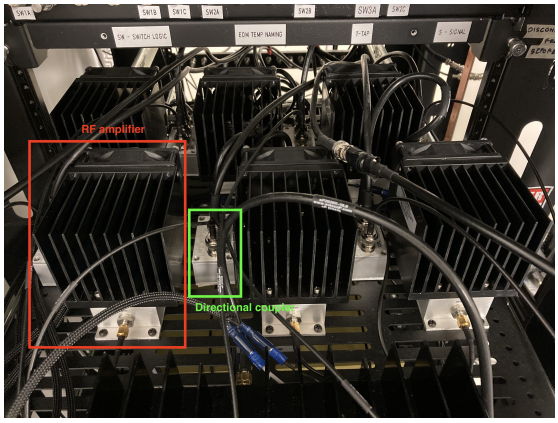

(a) AOM RF drive circuit drawer 1.

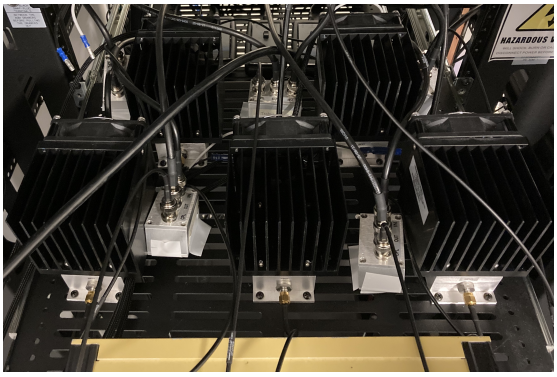

(b) AOM RF drive circuit drawer 2.

Figure 3.18: Photographs of the AOM RF drive circuits. 3.18a Six AOM RF drive circuits in AOM drawer 1. The heat sink for the trap RF drive amplifier is visible at the bottom of the picture. 3.18b Five AOM RF drive circuits in AOM drawer 2. The PSU is visible at the bottom of the picture.

W24GT50 24 V PSU that powers the trap RF drive circuit. The Mini-Circuits ZDC-20-1+ directional coupler[22] taps −20 dB of the signal emitted from the amplifier and returns the signal to the input patch panel for signal monitoring. Each circuit has a Mini-Circuits HAT-15+ RF power attenuator[23] which provides 15 dB of attenuation before the amplifier to protect the AOMs and the amplifier. LMR-100A and LMR-240 coaxial cable assemblies and some SMA-BNC adapters connect all the components and patch panels.

AOMs usually have a maximum operating frequency below 500 MHz, and so cannot satisfy all the laser modulation requirements for the QuantumIon apparatus. EOMs are used for higher-frequency modulation.

Electro-Optic Modulators

Similar to AOMs, electro-optic modulators (EOMs) map the characteristics of an RF signal on to laser light. Unlike an AOM, the path of the emitted light is not deflected and the carrier frequency of light is transmitted along with the modulated sidebands along the same path. EOMs are typically driven in the regime where the first order sidebands are

[22] https://www.minicircuits.com/WebStore/dashboard.html?model=ZDC-20-1%2B
[23] https://www.minicircuits.com/WebStore/dashboard.html?model=HAT-15%2B

have significant intensity and the higher order sidebands are negligible. EOMs can handle composite drive signals and generate sidebands for each frequency that is present in the RF drive signal.

EOMs have higher bandwidth than AOMs and are typically capable of modulating laser frequencies up $\approx 10\ GHz$. In the QuantumIon system, EOMs are used to modulate laser frequencies to drive transitions between specific hyperfine states in the ground, excited, and metastable states of $^{133}Ba^{+}$. The modulation frequencies chosen for Doppler cooling and SPAM operations as discussed in Sections 2.4 and 2.5, respectively, fall in the range $\omega = 0.2 - 9\ GHz$ (Table 2.2). These modulation frequencies, with additional frequencies chosen to support future implementation of the shelving repump laser, comprise the performance requirements for the electrical RF circuits that drive the EOMs. Additionally, the circuits must not exceed the maximum RF power that the EOMs can tolerate ($P_{max} = 1\ W = 30$ dBm), avoid excessive power loss, and prevent introduction of significant frequency noise into the signal. As with all other electrical circuits, the EOM RF drive circuits must fit into electrical rack drawers and connect to the RF signal source and EOMs with a system of cable assemblies and patch panels.

The apparatus includes three EOMs, one each for the 493 nm, 650 nm, and 614 nm lasers. The circuits that drive all three EOMs are identical. While the 614 nm shelving repump laser is not currently required, the overhead to assemble and test the circuit is low and building it now allows us to make efficient use of electrical rack space and quickly add shelving capability later. All of the components are ultrawide-bandwidth to support all the required modulation frequencies and keep all the circuits identical.

Sinara 4456 RF Synthesizer "Mirny" cards[24] and a Sinara 4457 "Almazny" high-frequency mezzanine card[25] from M-Labs supply the RF signals to drive the EOMs. The cards are RF synthesizers that operate at higher frequencies than the Urukul DDS cards that drive the trap RF and AOM circuits. The Almazny card is a *mezzanine* card that attaches to a Mirny card and increases the frequency of a signal generated by the Mirny card. With the Almazny mezzanine, these cards can generate RF signals with frequencies in the range $f = 53\ MHz - 13.6\ GHz$ with power output comparable to the Urukul card ($P_{max} \approx 10$ dBm).

Each EOM RF drive circuit consists of an RF power amplifier, a directional coupler, three RF switches with custom interface PCBs, an RF power combiner, and RF attenuators. Each circuit is also powered by three PSUs and connected by low-loss coaxial cables. All components interface with SMA connectors, which are suitable for higher frequencies

[24] https://github.com/sinara-hw/mirny/wiki
[25] https://github.com/sinara-hw/Almazny/wiki

than BNC connectors. The EOM and directional coupler are housed in a drawer in the optics rack inside the AHU. The remaining components are installed in an electrical rack drawer. Figure 3.19 shows a diagram of an EOM RF circuit and Figure 3.20 displays a photograph of the as-built circuits. A component manifest for each EOM RF circuit is presented in Table 3.8.

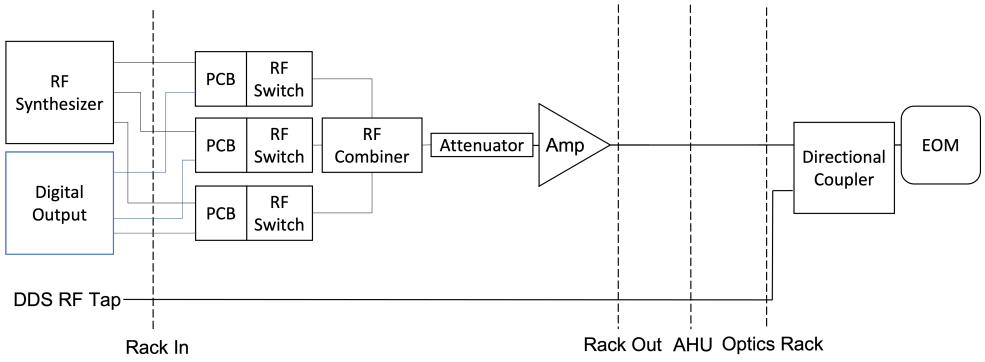

Figure 3.19: Diagram of the EOM RF drive electrical circuit (not to scale). The drive signal passes from left to right, while the tapped signals pass from right to left. Vertical dotted lines represent patch panels. A full electrical schematic of the circuit can be found in Appendix E.

Similar to the other RF circuits in the apparatus, the Mini-Circuits ZVA-1W-103+ RF power amplifier[26] is required to transmit the signal over the > 6 m of cable that connects the RF synthesizers to the EOMs. It provides $37 - 40$ dB of gain, is fan-cooled, requires a 15 V DC power supply, and draws $P = 12$ W of power. The Mini-Circuits ZUDC30-83-S+ directional coupler[27] provides a -30 dB signal tap to enable signal monitoring. RF power attenuators will protect the EOMs and circuit components from damage due to excess RF power. The attenuators have not yet been selected.

The RF drive signals for the EOMs must switch quickly between different frequencies to support fast switching between different operations on the ions. Unfortunately, the Mirny and Almazny cards emit pure tone signals and cannot make large frequency jumps sufficiently quickly and without introducing undesirable frequencies. A system of RF switches and combiners enables fast switching between different drive frequencies separated by several gigahertz. The DBWave PASA0100021800A RF switch[28] takes as inputs

[26] https://www.minicircuits.com/WebStore/dashboard.html?model=ZVA-1W-103%2B
[27] https://www.minicircuits.com/WebStore/dashboard.html?model=ZUDC30-83-S%2B
[28] https://www.DBWave.com/pdf/switchers/PASA0100021800A.pdf

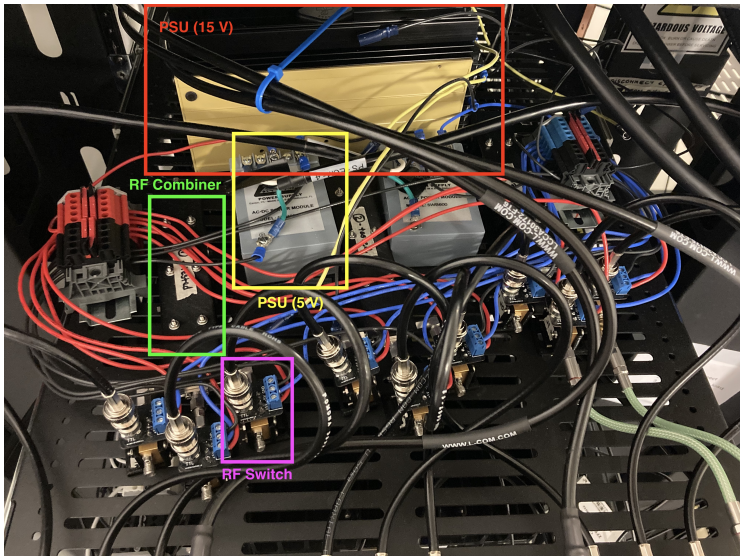

Figure 3.20: Photograph of the EOM RF drive circuit. The circuit components need to be arranged and fixed to the drawer. The RF combiners and RF switches are inside 3D printed mounts to align and connect the components. The RF power amplifiers are behind the 15 V PSU and are not shown. RF attenuators are not yet installed.

an RF signal and a digital input signal. When the digital input signal is high, the RF signal is transmitted. Otherwise, the signal is blocked. The switching time for the RF switch is $t = 250$ ns, sufficiently quick to support fast quantum operations. The RF switch requires DC power supplies of ± 5 V and draws ≈ 0.5 W of power. Each EOM drive circuit consists of three RF channels to support switching between and simultaneous input of up to three RF frequencies. The RF channels always emit signals and the digital channels control which signals reach the EOMs. The digital input signal are generated by Sinara 2128 8-channel isolated TTL cards[29] from M-Labs. The three RF signals are joined into a single channel by a Marki Microwave PD3-0R12 RF power combiner[30].

Two different kinds of PSUs are required to support the EOM RF drive circuits. The RF power amplifiers require a 15 V DC PSU and the RF switches require ± 5 V PSUs. Individual Acopian Model A15NT200 linear mode PSUs provides power to each RF power amplifier to suppress frequency noise. They supply up to $I = 2$ A of current at $V_{DC} = 15$ V. Two Acopian Model 5WB600 switching mode PSUs provide power to the RF switches. They supply up to $I = 6$ A each of current at $V_{DC} = 5$ V. One is oriented to provide

[29] https://github.com/sinara-hw/DIO_SMA/wiki
[30] https://www.markimicrowave.com/power-dividers/pd3-0r412.aspx

Component	Gain (dB)	Insertion Loss (dB)
ZVA-1W-103+ RF power amplifier	$37 - 40$	-
ZUDC30-83-S+ directional coupler	-	0.1
PASA0100021800A RF switch	-	$2 - 4$
PD3-0R12 RF power combiner	-	5
RF power attenuator	-	??
SMA connector	-	0.2
eP-ULL295 cable	-	15.2 (per 100 ft)
PE-300LL cable	-	17.9 (per 100 ft)
P142LL cable	-	27.4 (per 100 ft)
RG58C/U cable	-	1.4 (per 100 ft)

Table 3.8: RF power performance of the components in the circuits for driving the EOM drive RF signals at $\approx 1 - 10\ GHz$. RF power attenuator has not yet been selected. RG58C/U cable used for digital signals transmits in the kilohertz range.

positive voltage and the other provides negative voltage.

The interface to the RF switch is simply a set of four metal pins. We provide a more reliable connection to the power and signal pins with a custom PCB which we call the *DBWAVE_RF_SWITCH_BREAKOUT* (Figure 3.21). The PCB is soldered directly to the ground pin of the RF switch and has connector interfaces to the RF signal and digital signal inputs and terminal interfaces for the power supplies.

Ultra-low-loss coaxial cables are required for the EOM circuits because the signals are high-frequency. High-frequency RF signals naturally attenuate in coaxial cable assemblies more than low-frequency signals. The cable assemblies in the EOM RF drive circuits use evissaP eP-ULL295[31], Pasternack PE-300LL[32], and Pasternack PE-P142LL[33] low-loss coaxial cables. Digital signals signals are transmitted over RG58C/U[34] coaxial cable assemblies.

[31] https://www.evissap.com/cable-assemblies/low-loss-phase-stable-cables.html

[32] https://www.pasternack.com/pages/Featured_Products/low-loss-expanded-dielectric-pe-p300ll-flexible
html

[33] https://www.pasternack.com/50ohm-low-loss-flexible-pe-p142ll-coax-cable-triple-shielded-fep-jacke
aspx

[34] https://www.pasternack.com/flexible-0.195-rg58-50-ohm-coax-cable-pvc-jacket-rg58c-u-p.
aspx

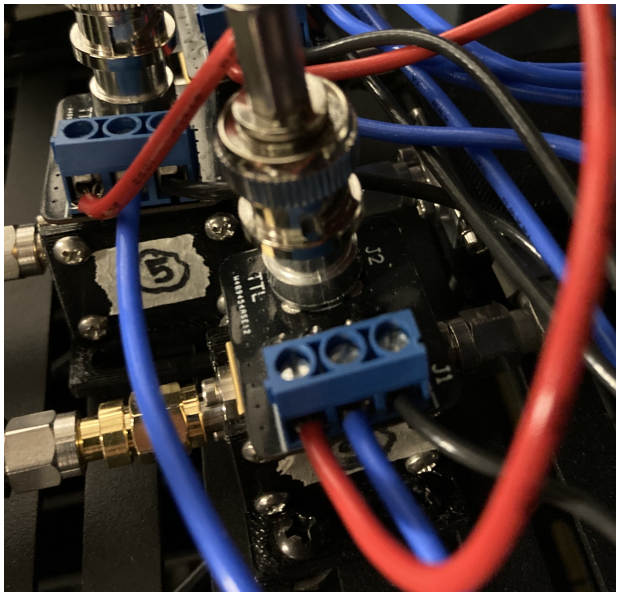

Figure 3.21: Photograph of an *DBWAVE_RF_SWITCH_BREAKOUT* PCB attached to an RF switch. The PCB provides a better, more secure interface to the switch electrical input pins. The red, blue, and black wires provide power and grounding, while the vertical BNC cable provides the digital input signal. The RF switch is beneath the PCB. A drawing of the PCB may be found in Appendix F.

3.2.5 Beam Preparation, Routing, and Monitoring

The optical systems that shape, filter, and route the laser beams from the laser heads to the vacuum chamber and into the trapping region are otherwise composed of passive optics such as polarizers, beam splitters, lenses, mirrors, filters, waveplates, etc. The design and implementation of the optical circuits built with those components are outside of the scope of this thesis and are discussed in detail in [10, 47, 120]. Several passive optical components are mounted on movable stages that can be controlled with computer commands via motor controllers or be driven directly with electrical signals. Remote control of the optical apparatus is important to maintain distance from the radioactive $^{133}Ba^{+}$ atomic source, achieve functional stability of individual components through real-time feedback, and build towards operational stability of the apparatus as a user facility. A list of the devices used for beam preparation, routing, and monitoring is given in Table 3.9.

Device	Purpose	Control
AG-PR100	Rotation stage	Controller
AG-LS25	Linear stage	Controller
8301NF	Linear actuator	Controller
8892-K	Mirror flipper	Direct
SA210-3B	Etalon	Direct
SA210-5B		Direct
K1S2P	Alignment mirror	Direct
K2S2P		Direct
SH05	Shutter	Direct
PDP90A	Alignment photodiode	Controller

Table 3.9: List of devices used for beam preparation, routing, and monitoring. Devices that will implement direct control via the real-time system are currently controlled via motor controllers.

Controller-Mediated Devices

Certain devices are driven by controllers, which are components that receive commands from a computer and translate them into the electrical signals required to control some device. They may control the motion of a stage or read detection information from a sensor. They may also implement feedback from the stages to stabilize motion and/or accurately determine the position of the stage. Controllers are used on devices that do not require real-time control during experiments and are controlled as peripheral devices (Section 4.2). The QuantumIon apparatus will integrate piezoelectric rotation stages and actuators, flipper mounts, etalons, positioning mirrors, shutters, and photodiodes driven by controllers. See Figure 3.22 for some examples of devices installed in the apparatus.

Select waveplates are mounted on Newport Agilis AG-PR100 piezoelectric rotation stages[35] to provide fine control over the polarization of laser beams. Certain lenses and telescope assemblies are mounted on Newport Agilis AG-LS25 piezoelectric translation stages[36] to provide fine control over beam path alignment. During prototyping and initial assembly, the stages are driven by a hand-held Newport Agilis AG-UC2 motor controller[37]. The final apparatus will integrate the Newport Agilis AG-UC8/PC[38] which features eight

[35] https://www.newport.com/p/AG-PR100
[36] https://www.newport.com/p/AG-LS25
[37] https://www.newport.com/p/AG-UC2
[38] https://www.newport.com/p/AG-UC8

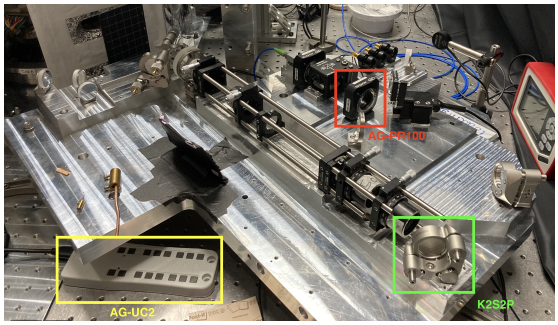

(a) Motion stages and controller.

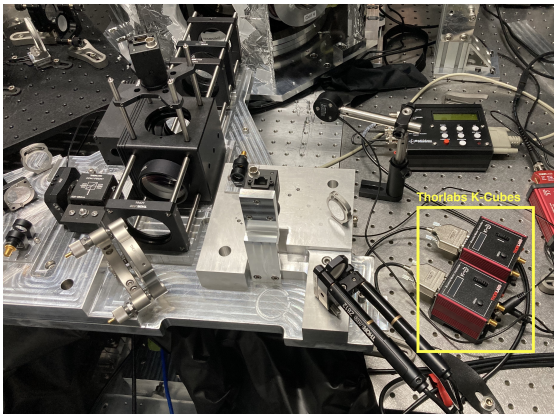

(b) Thorlabs controller for actuators.

Figure 3.22: Photographs of some controller driven stages and controllers installed on optical pegboards in the apparatus.

control channels each and computer control and power over Universal Serial Bus (USB). The objective lens in the imaging system (Section 3.3) is mounted on an assembly of seven Newport New Focus Picomotor 8301NF piezoelectric linear actuators[39] that control the objective position and orientation. The Picomotors are driven by Newport New Focus Picomotor 8742 motor controllers[40] featuring four control channels each and computer control via USB and Ethernet. Some mirrors are mounted on Newport New Focus 8892-K motorized flipper mounts[41] to control whether laser beams are diverted down diagnostic beam paths or propagate into the experiment. The flipper is controlled by a hand-held device with a switch that toggles the flipper motor.

Etalons that precisely measure the frequency of laser light feature motor controls to tune the cavity of the device. Thorlabs SA210-3B[42] and SA210-5B etalons[43] are driven by the Thorlabs SA201B voltage controller[44] which can connect to a computer via USB. Thorlabs POLARIS-K1S2P[45] and POLARIS-K2S2P[46] are mirror mounts with two piezoelectric actuators to control positioning and alignment. They are driven by Thorlabs KPZ101

[39] https://www.newport.com/p/8301NF
[40] https://www.newport.com/p/8742
[41] https://www.newport.com/p/8892-K
[42] https://www.thorlabs.com/thorProduct.cfm?partNumber=SA210-3B
[43] https://www.thorlabs.com/thorProduct.cfm?partNumber=SA210-5B
[44] https://www.thorlabs.com/thorproduct.cfm?partnumber=SA201B
[45] https://www.thorlabs.com/thorproduct.cfm?partnumber=POLARIS-K1S2P
[46] https://www.thorlabs.com/thorproduct.cfm?partnumber=POLARIS-K2S2P

controllers[47] which connect to a computer via USB. The Thorlabs SH05 optical shutter[48] blocks laser beams when they are not needed. It is driven by the Thorlabs KSC101 motor controller[49] which connects to a computer via USB. Finally, the Thorlabs PDP90A 2D lateral effect position sensor photodiode[50] helps determine if laser beams are aligned. It is read with a Thorlabs KPA101 controller[51] which connects to a computer via USB.

Directly Driven Devices

Some devices that interact with passive optics can be directly driven or read by electrical circuits. Devices that are directly driven by custom circuits are usually those that are involved in operating experiments and must be integrated into the real-time control system (Section 4.1). Single-photon detectors are the devices that primarily require direct control and are discussed in more detail in Section 3.3.1.

Devices that can be driven with motor controllers in some cases can be driven by custom circuits. Candidates for direct control are devices which we may want to control in real time. Other motivations for direct control are bypassing controllers that are large and/or expensive or have a complex or technologically incompatible control interface. Devices with motor controllers are only integrated into the real-time control system with custom electric circuits if the signal emitted by the controller is relatively simple and easily replicated.

Simply controlled devices that we plan to integrated into the control system include the Newport 8892-K flip mirror and Thorlabs SH05 shutter, which are driven with simple digital input signals, and the Thorlabs POLARIS piezoelectric alignment mirrors and etalons, which are driven with simple analog DC voltages. Bypassing the Thorlabs K-Cube controllers is also beneficial because those controllers are expensive, feature very few control channels, and require proprietary drivers.

3.3 Detection

The detection system collects photons scattered off of ions and atoms and sends signals to the computer. The photons scattered by the ions may be at any of the wavelengths that

[47] https://www.thorlabs.com/thorproduct.cfm?partnumber=KPZ101
[48] https://www.thorlabs.com/thorProduct.cfm?partNumber=SH05
[49] https://www.thorlabs.com/thorproduct.cfm?partnumber=KSC101
[50] https://www.thorlabs.com/thorProduct.cfm?partNumber=PDP90A
[51] https://www.thorlabs.com/thorproduct.cfm?partnumber=KPA101

correspond to the transitions of interest in $^{133}Ba^{+}$ as discussed in Section 2.1. In practice, the detection system primarily measures the $\lambda = 493$ nm photons that correspond to the Doppler cooling (Section 2.4) and SPAM operations (Section 2.5) because these operations yield information on whether ions are trapped, whether they are prepared in a known state, and what the ion state is after a experiment is performed. The system can also measure the $\lambda = 554$ nm photons scattered by the neutral barium atoms in a plume produced by ablation to help configure the ablation, photoionization, and detection systems. The imaging system is tuned to the plane of the RF null 68 μm above the surface of the Phoenix trap [10, 93].

The QuantumIon apparatus detection system has two operation modes: quantitative detection with single-photon detectors (SPDs) and qualitative detection with a camera. Light scattered by the ions is collected by an objective beneath the vacuum system in an imaging trench and transmitted towards the light sensors (Figure 3.23). A flip mirror enables remote toggling between the single-photon detector system and the camera detector system. The sensors used in the detection system are summarized in Table 3.10.

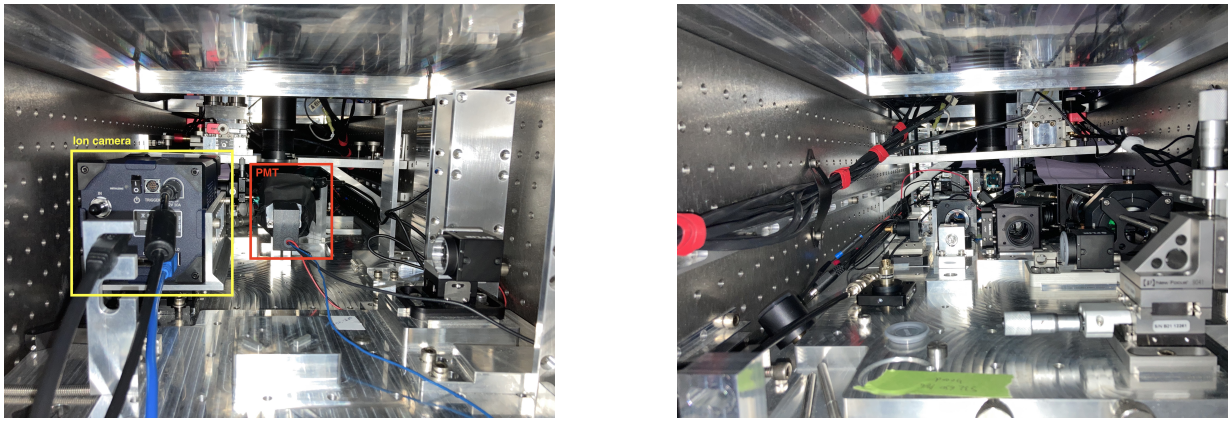

(a) 493 nm imaging trench.

(b) 554 nm imaging trench.

Figure 3.23: Photographs of the imaging trench beneath the vacuum chamber. 3.23a Side of the imaging trench that detects 493 nm light. 3.23b Side of the imaging trench that detects 554 nm light. A flip mirror toggles the system between using the two sides of the trench.

Component	Type	Purpose
H12775	PMT	Bulk ion/atom detection
C11202-100	APD	Individual ion detection
Prime BSI	sCMOS Camera	Image ions

Table 3.10: List of the sensors in the detection system. PMTs and APDs are forms of single-photon detectors. The ion camera takes pictures of trapped ions.

3.3.1 Single-Photon Detectors

Single-photon detectors (SPDs) are exactly what they sound like: sensors that detect single photons. A detection event is typically indicated by the emission of an electrical voltage pulse from the device. The proportion of photons incident on the sensor that are actually detected and yield a signal event is roughly given by the *quantum efficiency* of the device.

The QuantumIon apparatus uses two kind of single-photon detectors in the detection system: photomultiplier tubes (PMTs) and avalanche photodiodes (APDs).

Photomultiplier Tubes

The photomultiplier tubes (PMTs) in the detection system are used for quantitative bulk ion detection. The number of detection events, known as *counts*, is directly proportional to the number of ions or atoms in the region to which the PMT is attuned. The primary purpose of the PMTs is to determine whether ions or atoms are present in a given region of the trap.

The QuantumIon uses three Hamamatsu H12775 PMTs[52]. Two are in optical circuits configured to detect 493 nm light and one is to detect 554 nm light. Of the two PMTs detecting 493 nm light, one is aimed at the *quantum zone* of the trap and the other is aimed at the *loading zone* (Figure 3.12). The quantum zone is the region in the center of the trap where ions will be primarily trapped and to which most of the lasers and the detection system are aligned. The loading zone is a secondary zone off to the side where ions may be added to the trap without interfering with any ions already confined to the loading zone. After being trapped in the loading zone, the ions may be shuttled to the quantum zone. The 493 nm detection PMTs determine whether ions are trapped in the two regions. The 554 nm detection PMT determines whether neutral barium ions propagate through the

[52] https://www.hamamatsu.com/us/en/product/optical-sensors/pmt/pmt-module/photon-counting-head/H12775.html

loading or quantum zone during ablation and loading. Currently, our experiments focus on loading ions directly into the quantum zone to avoid implementing shuttling, so the 554 nm PMT is aligned to the quantum zone. In the future, the 554 nm PMT will be aligned to the loading zone.

The circuits that connect the PMTs to the real-time control hardware are very simple and identical for all PMTs. The PMTs emit simple digital output pulses upon detecting photons. The pulses are expected in the kilohertz range, so RG58U/C coaxial cable assemblies are sufficient as minimal signal loss is expected, even over a long cable run. The cables run through the system of patch panels and electrical racks back to a Sinara 2128 8-channel isolated TTL card which counts the number of counts within a given time window to determine whether ions are present.

Avalanche Photodiodes

The avalanche photodiodes (APDs) in the detection system are used for quantitative measurement of individual ions in a linear chain of multiple ions. They are at the end of an optical system that enables quantitative measurement of each ions individually [10]. The QuantumIon apparatus uses 16 Hamamatsu C11202-100 single-photon avalanche diodes (SPADs)[53], one for each qubit that the system will ultimately operate. The APDs are in optical circuits that detect 493 nm light, the wavelength scattered by the ions during SPAM (Section 2.5) and are aligned to the quantum zone of the trap.

Since the APDs generate digital output pulses upon photon detection just like the PMTs, the electrical circuits that connect the APDs to the real-time control system are identical to the electrical circuits that support the PMTs. RG58U/C coaxial cable assemblies connect the APDs to four Sinara 2128 8-channel isolated TTL cards. The APDs and their accompanying electrical circuits are not required for initial trapping experiments and therefore are not yet installed in the system.

3.3.2 sCMOS Ion Camera

The camera that captures images of the ions is a Teledyne Photometrics Prime BSI sCMOS camera[54]. It is a scientific Complementary Metal–Oxide–Semiconductor (sCMOS) camera that offers attractive capabilities: high quantum efficiency for wavelengths of interest,

[53] https://www.hamamatsu.com/eu/en/product/optical-sensors/mppc/photon-counting-module/C11202-100.html

[54] https://www.photometrics.com/products/prime-family/primebsi

6.5 μm pixels, multiple triggering and capture modes, low uncorrelated background noise, and options for limited automated image processing. We refer to this camera as the *ion camera* to distinguish it from proposed (and unimplemented) monitoring cameras. The QuantumIon imaging system is designed for the ions in the trap to have uniform 4 μm spacing between them and for the light emitted by a single ion to occupy a single pixel with multiple pixels of separation between each ion [10].

The ion camera connects to the control server via USB 3.0 standard connection with a SuperSpeed Type B connector [118]. The connection speed necessary to transmit image data requires the faster USB 3.0 standard. The cable assembly we use to connect the ion camera to the control server features several repeaters to compensate for signal degradation over the long length of cable required. The USB connection permits camera configuration and image collection as a peripheral control device (Section 4.2.3). The ion camera does allow external triggering, so future implementation may include a triggering circuit for real-time control.

The ion camera is installed in the apparatus and connected to the control server with computer control implemented. It is not currently in use as initial trapping experiments utilize single-photon detectors (Section 3.3.1).

3.3.3 Focus and Alignment Motors and Controllers

The detection system includes passive optics mounted on devices that can be controlled either via controllers or directly through the real-time control system. The optics control devices are the same used to prepare, route, and monitor the laser beams in the apparatus. See Section 3.2.5 for details.

3.4 Magnetic Field Coils

While the ground qubit encoding states in $^{133}Ba^{+}$ are not sensitive to magnetic field noise (Section 2.1), it is still beneficial to control the magnetic field that the ions experience in the ion trap. Magnetic field coils enable us to define the magnetization axis of the system and determine how laser beams should be oriented to achieve the photon polarization to drive important quantum operations (Section 2.5). Additionally, intentionally inducing a magnetic field allows us to control the Zeeman splitting of degenerate hyperfine states, preventing the possibility of coherent dark states [47]. The magnetic field in the QuantumIon apparatus is controlled with a system of Helmholtz coils.

3.4.1 Helmholtz Coils

Helmholtz coils are a simple method of generating a near-uniform magnetic field in a localized region of space. A uniform magnetic field is important because all ions should experience the same magnetic field so that they all have the same magnetization axis and perform the same in all quantum operations no matter where they are in the trap. We chose Helmholtz coils because they are simple to model and understand and easy to assemble and use.

The magnetic field coils in the QuantumIon apparatus consist of three pairs of Helmholtz coils, one for each spatial dimension. Each pair of coils is connected in series, separate from the other pairs, and mutually orthogonal to each other. Thus, each axis has an individually controllable, uniform magnetic field, permitting the creation of a magnetic field of arbitrary direction and strength in the middle of the coils. Further discussion of how Helmholtz coils generate magnetic fields may be found in Appendix C.

The coils are mounted on an assembly we refer to as the *castle*. It is an aluminum frame that sits around the vacuum chamber on the optics table in the AHU (Figure 3.24a). The mounts for the coils on the axes parallel to the optics table are aligned with viewports on the vacuum chamber. The final coil pair is larger and is oriented normal to the plane of the optics table. The coils on each axis are tightly wound of 14 AWG wire and are designed to generate a field of up to $B = 5$ G in an arbitrary direction from up to $I = 8$ A of current per coil pair.

The coils are connected to the PSU by a system of copper cables with banana and spade connectors. The system is modular such that the pairs of coils can be attached in series and driven by the same current or detached so that each individual coil may be by driven by its own current (Figure 3.24b). Individual coil control will permit creation of magnetic field gradients, if desired.

3.4.2 Power Supply Unit

The current for the magnetic field coils is provided by a BK Precision Model 9410 PSU[55]. It provides up to $I = 8$ A of current on three individually-controllable channels with a banana jack interface. The magnetic field coils will operate continuously at a constant setting, so there is no need for computer control. The PSU is housed in the optics rack. It will be moved outside the AHU to an electrical rack.

[55] https://l.bkprecision.com/products/power-supplies/9140-triple-output-multi-range-dc-power-supply-
html

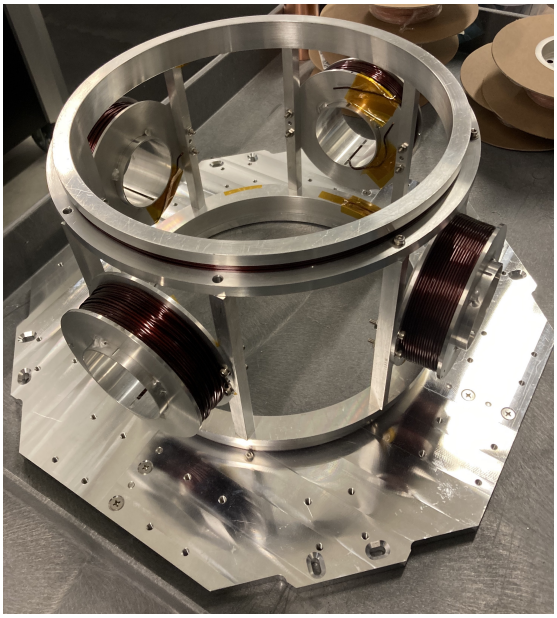

(a) Aluminum castle with Helmholtz coils.

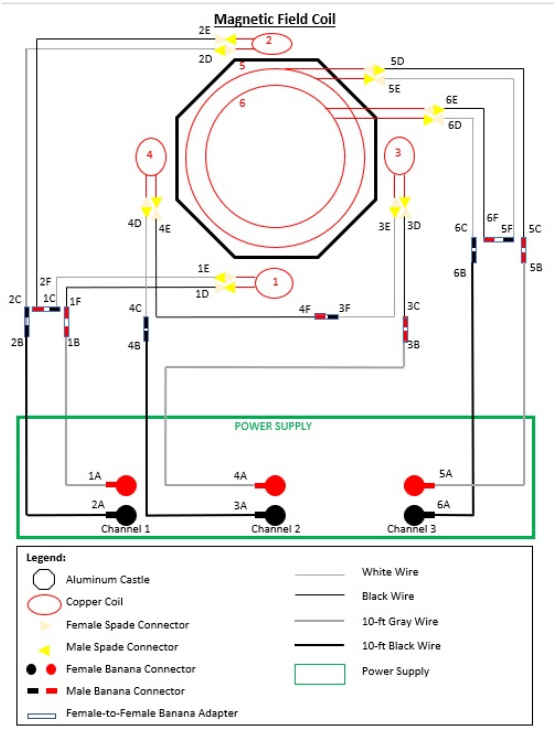

(b) Diagram of how the coils are connected.

Figure 3.24: Photograph and diagram of the Helmholtz coils that generate the controlled magnetic field for the ion trap. 3.24 The aluminum castle with Helmholtz coils mounted. The castle then sits around the vacuum chamber. 3.24b Diagram indicating how the coils are connected to each other and to the current source.

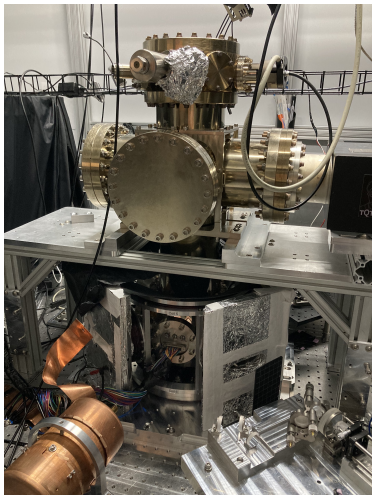

(a) Chamber from front.

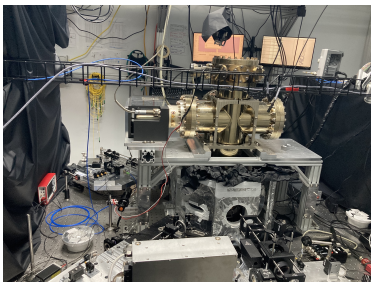

(b) Chamber from back.

(c) Pump, pressure monitors.

Figure 3.25: Photographs of the vacuum chamber as seen from two perspectives in the AHU and the pump and pressure monitors.

3.5 Vacuum Chamber System

The Phoenix trap and atomic source reside inside an vacuum chamber than maintains ultrahigh vacuum (UHV), which is necessary to prevent particles from colliding with the trapped ions and modifying their state uncontrollably or even ejecting them from the trap. The trap is a custom design and was manufactured by external commercial partners. The design prioritizes UHV, high numerical aperture (NA) viewports, and electrical feedthroughs that permit appropriate control of the ion trap. Figure 3.25 shows the vacuum chamber and monitors. For more details on the design and assembly of the vacuum chamber in the QuantumIon apparatus, see [47].

The pumps, getters, controllers, and sensors on the vacuum chamber operate constantly and do not require external controls. The vacuum chamber consistently achieves $P \leq 4e-11$ mbar of pressure.

3.6 Assembly Status

This section details the status of the assembly of the custom electrical circuits required to drive electrical components in the QuantumIon apparatus as of July 2023. Where

appropriate, integration test data demonstrating the performance of individual subsystems is reported.

During assembly, we perform unit tests on each individual component as quality assurance (QA) to ensure each component performs as specified. After assembly, we perform integration tests to ensure each circuit performs as intended.

3.6.1 Ion Trap

Initial versions of the circuits that drive the ion trap to produce the confining electric potential well for the ions have been built and tested.

Trap RF Pseudopotential Circuit

The apparatus currently has a prototype version of the trap RF drive circuit described in Section 3.1.1 installed to support initial trapping experiments on a non-radioactive $^{138}Ba^{+}$ atomic source.

We performed functional, power supply noise coupling, extinction ratio, and noise floor tests on all RF electrical circuits (trap RF drive, AOM RF drive, and EOM RF drive). The tests are designed to evaluate whether the circuits perform as designed. The tests all measure the circuit before the resonator, thus excluding the behavior of the resonator and the ion trap.

The functional test is an integration test that simply evaluates whether the circuit and its constituent components are connected correctly and installed properly. We send a signal through the RF circuit and measure the output circuit to determine whether the power and frequency content of the circuit is as expected. A DS Instruments SG6000X Signal Generator[56] is the signal source and a Keysight N9020A MXA Signal Analyzer[57] measures the signal. See Table 3.11 for a manifest of experimental materials. A photograph of the experimental setup is shown in Figure 3.26.

The procedure for the functional test is:

1. Calibrate expectations of the emitted signal by directly connecting the source to the spectrum analyzer and measuring the harmonic content and power of the RF signal without the intervening circuit.

[56] https://www.dsinstruments.com/product/rf-signal-generators/dual-channel-usb-6ghz-rf-signal-generat
[57] https://www.keysight.com/us/en/product/N9020A/mxa-signal-analyzer-10hz-26-5ghz.html

Instrument	Purpose
DS Instruments SG6000X Signal Generator	Generate RF electrical signal
Keysight N9020A MXA Signal Analyzer	Measure frequency and power of signal
Mini-Circuts FW-10+ RF attenuator $\times 2$	Protect components and instruments

Table 3.11: List of materials used in RF circuit functional tests to measure the frequency and power of transmitted RF electrical signals.

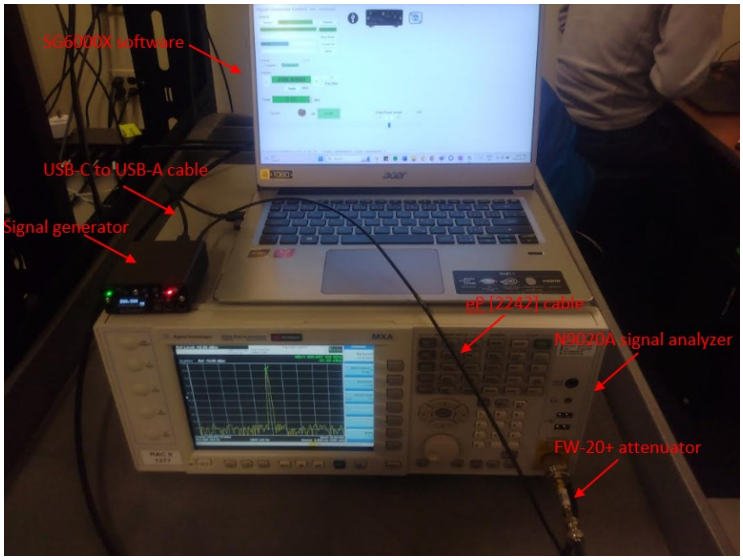

Figure 3.26: Photograph of the experimental setup for the RF circuit integration tests featuring signal generator and signal analyzer.

- Ensure that attenuators are used to avoid damaging the detector!

2. Physically check that the circuit is connected to the circuit load, the RF amplifiers are on, and the signal source is connected.

   - The following procedure *must* be followed when driving RF circuits to prevent damage to the RF amplifiers:
     (a) Connect the output load.
     (b) Turn on the power to the amplifier.
     (c) Turn on the RF input signal.
   - When disconnecting the circuit, follow the above instructions *in reverse*.

3. Turn on the signal source at appropriate power and frequency.
    - Protect delicate components and instruments with RF power attenuators.
4. Measure the spectrum of the emitted signal with the signal analyzer.
5. Measure the power of the emitted signal with signal analyzer.
6. Repeat for directional coupler taps.

The circuit should not introduce noise at frequencies other than the drive frequency. Some noise at the PSU switching frequency $f_s = 55$ kHz is expected. The expected power of the output and emitted signal are calculated from the input power of the signal generator, the gain and insertion loss of the individual components and cables, and the tap ratio of the directional coupler.

We found that the trap RF drive circuit performed as expected. No observable frequency noised was introduced and the signal was amplified and tapped at the expected powers. Figure 3.27 shows the spectrum analyzer trace for the RF circuit output from the circuit (before the resonator). Table 3.12 summarizes the expected and measured RF signal parameters. The functional test for the bidirectional coupler tap channel showed similar results. Thus, the results of subsequent tests are assumed with high confidence to apply to the coupler tap channels as well.

Parameter	**Expected Value**	**Measured Value**
Frequency peak (MHz)	200	200
Signal power (dBm)	16	14.46
Other noise peaks (kHz)	55	-

Table 3.12: Summary of the trap RF drive circuit functional test results. The measured parameters closely match the expected values. The minimal 55 kHz peak expected from the PSU switching was not detected.

The next test we performed was a channel *cross-talk* test. Since all the RF power amplifiers for the trap RF drive and AOM RF drive circuits are powered by the same switching PSU, we measured to see if the connection to a common component causes cross-talk between the signals: whether a signal passed through one circuit transmits across another circuit.

The materials and experimental setup for the cross-talk test are identical to those for the functional test. The procedure is similar, except that we measure the output of exclusively

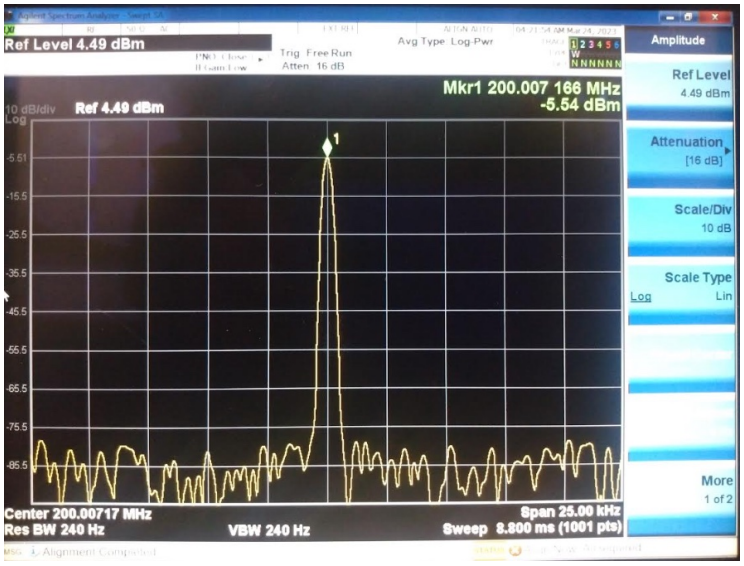

Figure 3.27: Photograph of the spectrum analyzer trace for the trap RF circuit functional test. A clean signal peak at $f = 200$ MHz is observed with no unexpected power attenuation. The peak power includes a -20 dB offset from the RF power attenuator.

different circuits than the one driven by the signal. Unmeasured signals are loaded with 50 Ω RF terminators.

An example signal analyzer trace for the extinction test is shown in Figure 3.27. Similar traces were collected for comparison against all 11 AOM RF drive channels which show similar data and are omitted. No cross-talk signal was detected when RF signals were turned on. Some minuscule RF power at the drive frequency was detected and was later determined to be caused by residual output from the Urukul DDS cards to which each channel was connected. The signal is sufficiently small to be neglected.

The final RF circuit test is an RF power noise floor test and extinction ratio test. The noise floor is the lowest possible power level that can be measured in the circuit in aggregate and across all frequencies and is determined by the environmental noise in the system and instruments. The extinction ratio is the difference between the power measured when the circuit is active and the noise floor. A low noise floor and large extinction ratio indicates that the circuit can reliably transmit a drive signal since the 'on' and 'off' behavior are distinct. In particular, when the signal source is off, no signal that could drive a component is transmitted.

The materials and instrumentation used for noise floor and extinction ratio tests are

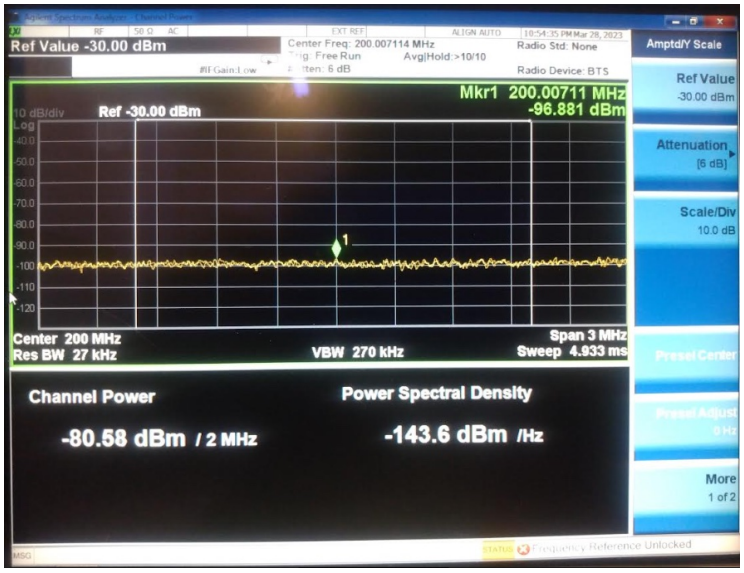

Figure 3.28: Photograph of spectrum analyzer trace for trap RF cross-talk test. No cross-talk was observed when AOM RF drive channel 1 was active, as concluded by the fact that the small peak did not change in power when an other drive signal was turned on. The small peak is residual output from the Urukul DDS channel.

the same as those used for the functional and cross-talk tests. The procedure for these tests is similar as those for the functional and cross-talk tests as well. The noise floor is measured by simply calculating an average of the RF power when the circuit is not driven over a suitable duration of time. The extinction ratio is calculated by making a similar measurement of the RF power when the circuit is driven and taking the difference between the driven power and the noise floor. Table 3.13 shows the results of the noise floor and extinction ratio measurements for the trap RF drive circuit. We find that the circuit has a more than suitably low noise floor and high extinction ratio to drive the ion trap RF.

Signal Power (dBm)	**Noise Floor (dBm)**	**Extinction Ratio (dB)**
14.45	-57.17	71.6

Table 3.13: Results of the trap RF drive circuit noise floor and extinction ratio tests. A noise floor of ≈ -57 dBm was measured regardless of the RF power attenuators used to protect the signal analyzer.

The current resonator is tuned to a frequency $\approx 33\%$ below the target RF drive frequency. We are currently designing and building a new resonator that will operate closer to

the target RF drive frequency of $f_{rf} \approx 44$ MHz to replace the one in the apparatus. Discussion of evaluations of the resonator and the circuit performance with the resonator included may be found in [10]. The loaded and unloaded resonant frequency of the resonator as well as the Q-factor are measured.

Trap DC Potential Circuits

A prototype version of the trap DC potential circuits described in Section 3.1.2 have been installed. Connectivity tests confirm that we understand which DAC pin in the control system ultimately connects to which pin on the DD100 cable that connects to the DD100 connector on the vacuum chamber feedthrough. We observed significant low-frequency noise in the trap DC electrodes circuits using a RIGOL DS1102E digital oscilloscope[58] (Figure 3.29) by directly connecting a simple probe to the circuit terminus. Electrical noise may introduce fluctuations into the confining potential, heating the ions. We plan to repeat this measurement more rigorously with a battery-operated oscilloscope to avoid potential ground loops and determine the true noise level. We will also upgrade the trap DC potential circuits with new PCBs to remove unnecessary features and move improved noise filters closer to the vacuum chamber.

The current iteration of the *HD68_TO_DB25_BREAKOUT* has been assembled and passes performance unit tests confirming that the pins in the HD68 connectors are connected to the pins in the DB25 connectors as expected. It will be housed in a shelf in the electrical racks, but is not yet installed in the apparatus. A previous version of the same PCB which contains low-pass filter circuits and conversion from double-ended to single-ended voltages is currently installed. We have since determined that the Zotino DAC card emits single-ended voltages and the filters should be closer to the vacuum chamber to reduce electrical noise from the environment.

The current iteration of the *DD100_TO_DB25_BREAKOUT* board is still under development. The low-pass filter and voltage limiter circuits have been designed, prototyped, and validated. The full PCB is currently being drawn. After design review, it will be ordered, assembled, tested, and installed. A previous version of the same PCB which contains no circuit elements and simply converts from four DB25 connectors to a single DD100 connector is currently installed. The versions of both of the PCBs described in this section will replace their previous iterations in the apparatus (Figure 3.30).

All of the cable assemblies and patch panels required to connect the components in the trap circuits are installed in the apparatus. The DD100 cable assembly will be replaced

[58] https://www.rigolna.com/products/digital-oscilloscopes/1000/

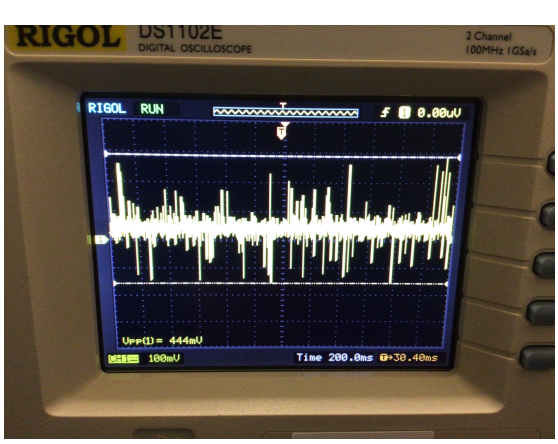

(a) Noise in trap DC electrodes circuit.

(b) Noise in ground bar.

Figure 3.29: Photographs of oscilloscope traces measuring significant noise in the trap DC electrodes circuits. 3.29a $\approx$ 400 mV low-frequency electrical noise measured in the trap DC electrodes circuits. This is about 4% of the maximum voltage that may be put on the electrodes. 3.29b We traced the source of the noise to building ground. Isolation and noise filtering are required on the circuits.

with a newer cable assembly that implements paired twisted conductors and improved shielding to protect from noise will be procured and replace the current version of the cable assembly (Figure 3.31).

The Phoenix trap in the apparatus is currently a 'mechanical sample' in which some of the DC electrodes are shorted to ground and/or each other, making them unusable. The remaining electrodes should allow us to create a suitable trapping potential. A fully functioning trap will replace the one currently installed in the vacuum chamber.

3.6.2 Lasers

The 532 nm pulsed ablation laser, 389 nm and 493 nm CW photoionization lasers, 493 nm CW Doppler cooling and SPAM laser, and 650 nm CW repump laser are all installed and frequency locked. The beam paths for each laser are installed and aligned to the appropriate location in the vacuum chamber as appropriate.

(a) Current PCB converting from HD68 to DB25 connectors.

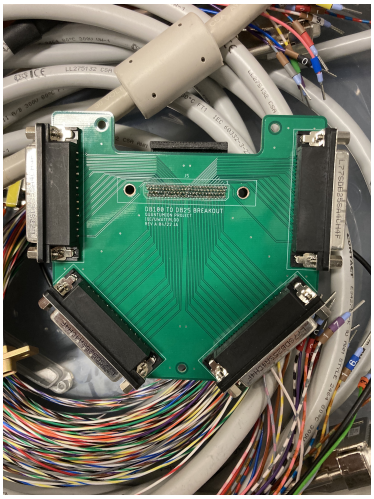

(b) Top view of the current PCB converting from DB25 to DD100 connectors.

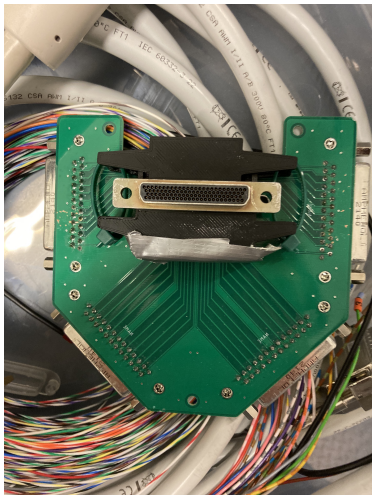

(c) Bottom view of the current PCB converting from DB25 to DD100 connectors.

Figure 3.30: Photographs of the current iterations of the custom trap DC electrodes circuits PCBs. 3.30a The *HD68_TO_DB25_BREAKOUT* PCB contains unnecessary circuits and will be simplified. 3.30b DB25 connectors on the *DD100_TO_DB25_BREAKOUT* PCB. The PCB requires addition of filter and voltage limiter circuits. 3.30c DD100 connector on the *DD100_TO_DB25_BREAKOUT* PCB.

3.6.3 Laser Modulation

The RF circuits driving the AOMs and EOMs have been built, installed, and tested.

AOM RF Drive Circuits

11 AOM RF drive circuits as described in Section 3.2.4 have been built, installed, and tested. We performed the functional, cross-talk, and noise floor/extinction ratio tests as described in Section 3.6.1 on all of the AOM RF drive circuits.

The circuits pass functional tests at $f = 200$ MHz. No significant noise at the PSU switching frequency nor any other frequencies are observed. The signal transmits with appropriate power. The signal analyzer trace of the measured signal for channel 1 is shown in Figure 3.32. Traces for the other circuits show similar results and are omitted. The functional test for the directional coupler tap channel showed similar results. Thus, the

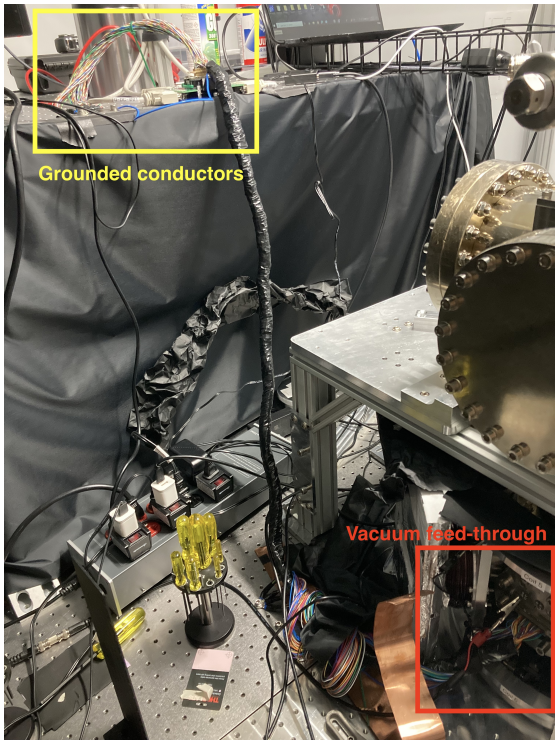

(a) Trap electrodes circuit on optics table.

(b) DD100 cable assembly.

Figure 3.31: Photographs of DD100 cable assemblies. 3.31a Test DD100 cable assembly used with the mechanical Phoenix test trap. Channels leading to shorted electrodes are grounded. 3.31b Candidate replacement DD100 cable assembly with all 100 channels intact. May be replaced with yet another cable assembly with paired conductors and additional shielding.

results of subsequent tests are assumed with high confidence to apply to the coupler tap channels as well.

The AOM RF drive circuits also pass cross-talk tests with the same results as the trap RF drive circuit. An example signal analyzer trace of the measured signal on AOM RF drive channel 2 when another channel was active is shown in Figure 3.33. As with the trap RF drive circuit, some residual signal from the DDS was observed. Traces for all other combinations of cross-talk tests for the AOM RF drive circuits and the trap RF drive circuit show similar results and are omitted.

Finally, the AOM RF drive circuits pass noise floor and extinction ratio tests with an

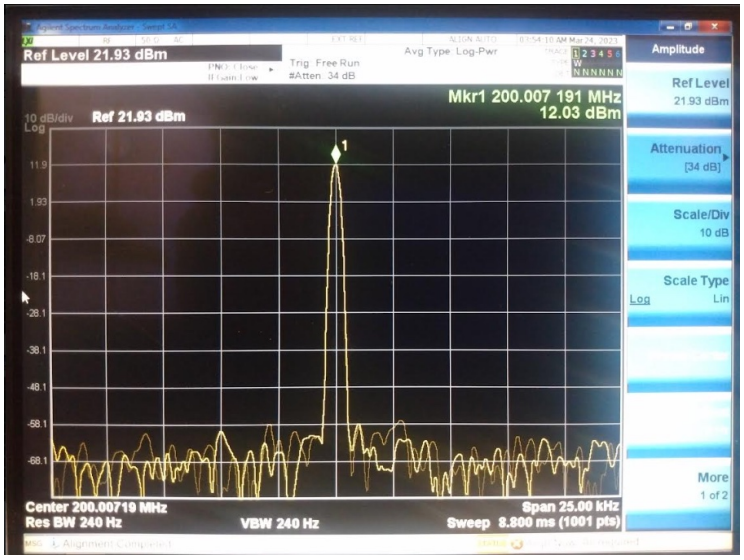

Figure 3.32: Photograph of an example signal analyzer trace for the AOM RF drive circuit functional test. The circuit tested for this trace was channel 1. A clean signal peak at $f = 200$ MHz is observed with no unexpected power attenuation. The peak power includes a -20 dB offset from the RF power attenuator.

average observed extinction ratio of ≈ 70 dB, similar to the trap RF drive circuit. Thus, the circuits are appropriate drivers for AOMs to act as fast switches.

In summary, the circuits transmit 200 MHz RF signals without excessive loss of power or introduction of frequency noise. The tests reported here were performed before attenuators were installed into the AOM circuits. We have installed the attenuators and are in the process of repeating the aforementioned integration tests.

EOM RF Drive Circuits

All three EOM RF drive circuits as described in Section 3.2.4 have been built and partially installed. All of the components in the circuits pass unit tests for functionally. Anecdotally, the circuits pass spot integration tests and successfully transmit gigahertz-range electrical signals without excessive loss of power or introduction of frequency noise. Once fully installed, we will perform full formal functional and noise floor/extinction ratio tests on all branches of the EOM RF drive circuits. The cross-talk test will likely be omitted because each RF power amplifier in the circuits is powered by its own linear PSU.

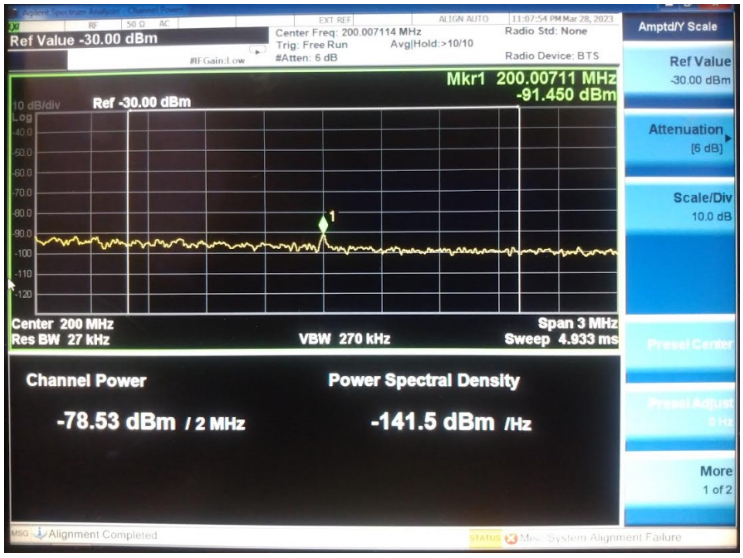

Figure 3.33: Photograph of an example spectrum analyzer trace for trap RF cross-talk test. No cross-talk was observed in AOM RF drive channel 2 when channel 3 was active, as concluded by the fact that the small peak did not change in power when an other drive signal was turned on. The small peak is residual output from the Urukul DDS channel.

When combined with the three PSUs and stiffer ultralow-loss coaxial cable assemblies, the circuits are difficult to install into a single rack drawer. We are currently working on installing the EOM circuits into a single electrical rack drawer. Circuit installation does not block experiments on the apparatus because current experiments use $^{138}Ba^{+}$, which has no nuclear spin ($I = 0$), resulting in no hyperfine splitting that requires laser frequency modulation. As-installed circuit performance will inform the selection of RF power attenuators to protect vulnerable circuit components.

3.6.4 Passive Optical Components, Stages, and Controllers

The passive optics described in Section 3.2.5 that must be mounted on or are integrated with movable stages are assembled and installed on to optical pegboards in the apparatus. Devices are connected to their motor controllers as needed for integration, alignment, and tuning the apparatus. The devices and controllers are not connected to the real-time control hardware or control server. The electrical circuits required to directly drive the beam preparation, routing and monitoring devices are under development. Integration into the real-time control system is low priority during initial trapping experiments because

control can be easily achieved as needed with the controllers and a laptop.

3.6.5 Detection

The detection system is partially set up for the minimal requirements of detecting whether ions are trapped.

Single Photon Detectors

Only the circuits for the 493 nm and 554 nm PMTs aligned to the quantum zone as described in Section 3.3.1 are implemented to support initial trapping experiments. During experiment, the control system receives counts proportional to the light to which the PMTs are exposed. No APDs or circuits that support them are installed.

Ion Camera

The ion camera is installed in the imaging trench and connected directly to the control server (Section 4.3) via a long USB 3.0 cable with signal repeaters. We plan to route the USB connection through patch panels to confirm with the overall system design if possible. Another solution may be to control the camera with a separate local control computer. We are considering adding a digital input signal to the ion camera to support real-time triggering. The control software that drives the camera has been developed and works as expected (Section 4.2.3).

3.6.6 Magnetic Field Coils

The magnetic field coils as described in Section 3.4 are currently wound and installed on the castle, which itself is installed on the optics table around the vacuum chamber. The cables that connect the coils in series and to the PSU have been installed. The PSU is housed in the optics rack inside the AHU and is connected directly to the magnetic field coils with no intervening patch panels.

The magnetic field coils individually passed unit tests for field generation immediately after being wound. The fields generated by the full assembly mounted on the castle has not yet been tested. Once we obtain a suitable gaussmeter, we will test the magnetic fields.

Testing the field generated by the magnetic field coils has been low priority during initial experiments to trap $^{138}Ba^{+}$, which has no hyperfine energy levels.

Future work on the magnetic field coils system will be to bring it into alignment with the design principles applied to the other electrical subsystems and modularize the coils. We will move the PSU outside the AHU so that it may be easily monitored and operated from an electrical rack. Additional cables will be installed so that the PSU can connect to the coils through the patch panel system that the rest of the electrical subsystems use. We also plan to install an electrical panel inside the AHU to permit quick reconfiguration of the the magnetic field coil system between connecting pairs of coils in series and controlling each coil individually. Finally, we are considering upgrading the PSU to enable active stabilization of the magnetic field to reduce the effect of magnetic field noise on the fidelity of quantum operations and support more control channels to drive each Helmholtz coil individually.

3.6.7 Vacuum Chamber

The vacuum chamber has the ion trap and a $^{138}Ba^{+}$ source installed. It holds vacuum as expected and is installed on the optics table.

We plan to break vacuum and open the chamber in the near future to make major upgrades to the system motivated by our challenges in trapping ions thus far. A broken pin on the feedthrough caused arcing between the resonator and the vacuum chamber and must be repaired or replaced. We plan to mechanically reinforce the feedthrough pins to prevent future breaks. While the vacuum chamber is open, we will replace the current mechanical sample trap with a fully functional Phoenix trap and check that the wiring harness correctly connects all signals from the feedthrough to the trap. Finally, we will install an atomic source of $^{133}Ba^{+}$ next to the existing $^{138}Ba^{+}$ and ensure that the sources are in the correct orientation with respect to the lasers for cooling the ions.

Chapter 4

Control System

All quantum computers are hybrid computing devices composed of quantum hardware and a classical computer that controls the apparatus and interaction with the quantum hardware. This paradigm fits the computation accelerator model [96, 115] with the classical computer as the host and the quantum hardware as the accelerator device. In the case of the QuantumIon system, the ion trap is the quantum hardware accelerator device. This chapter describes the control system for the ion trap and the classical computer that serves as the computation host. Figure 4.1 shows a diagram of the technology stack for the QuantumIon control system, the components of which will be detailed in this chapter.

While the coherence time of trapped ions is long, the physical phenomena of ions relevant to quantum information processing operations, such as relaxation from excited energy states and Rabi oscillations, occur on the order of microseconds and nanoseconds. Therefore, the control system must operate on the same time scale to effectively coordinate interactions with the ions to perform quantum operations. For the purpose of this chapter, *real-time* refers to controls and operations that occur on the time scale of atomic physics phenomena and require sub-microsecond precision. Non-real-time or *peripheral* controls refer to devices that perform operations with more relaxed time constraints.

Section 4.1 describes the real-time hardware and software that form the core of the quantum control system for the QuantumIon apparatus. Non-real-time peripheral devices and the method by which they communicate with the real-time control system are presented in Section 4.2. The characteristics of the host server for the control system are summarized in Section 4.3. Section 4.4 discusses the initial work on a full stack quantum control framework to be built on top of this control system. Finally, the assembly status of the control system is reported in Section 4.5.

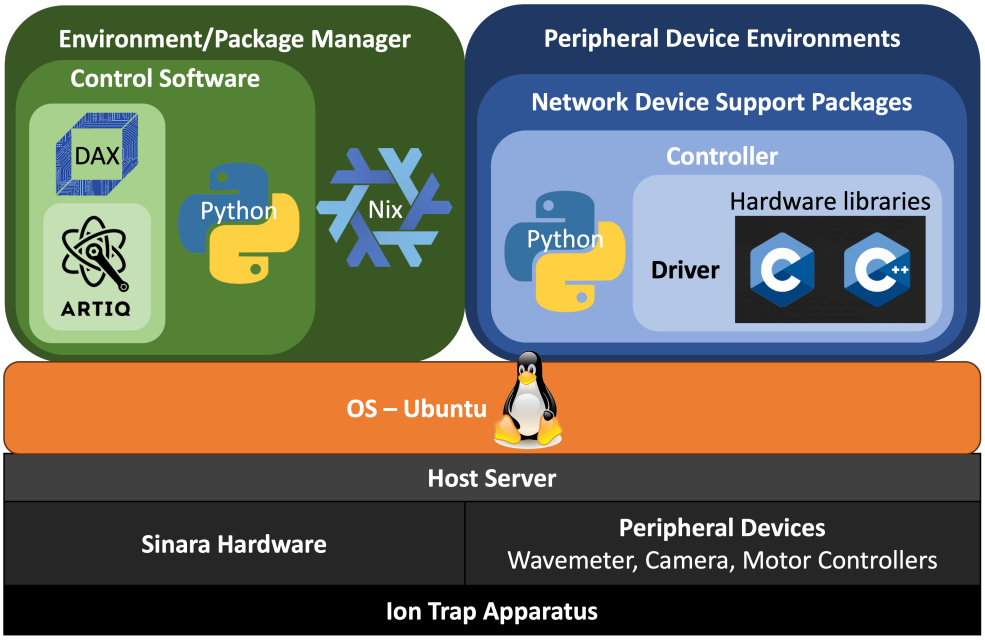

Figure 4.1: Diagram of the software and hardware technologies employed in the QuantumIon control system. The control flows from software at higher levels of abstraction at the top of the diagram to hardware operation at the bottom of the diagram. The left side of the diagram are broadly the real-time technologies, while the right side are the peripheral technologies.

4.1 Real-Time Quantum Controls

The core of the quantum control system for the QuantumIon apparatus is the real-time control system which coordinates all the elements of the apparatus described in Chapter 3. Real-time controls are accomplished using a custom-specified Sinara hardware system programmed with software based on Advanced Real-Time Infrastructure for Quantum Physics (ARTIQ) [13, 56, 57, 61].

Sinara hardware[1] and ARTIQ software[2] were chosen to implement the QuantumIon control system because they offer multiple advantages. The hardware and software are co-designed and tightly integrated, reducing potential software integration and deployment issues. Both Sinara hardware and ARTIQ software were originally designed by researchers

[1] https://github.com/sinara-hw
[2] https://github.com/m-labs/artiq

at the Ion Storage group at the National Institutes of Standards and Technology (NIST) in Boulder, Colorado, USA[3], and as such directly target control of ion trap apparatuses. Competing quantum control systems target either superconducting apparatuses or claim to control all quantum computing platforms, introducing some mismatches between the requirements of ion trap apparatuses and the capabilities of those control systems. Additionally, Sinara hardware and ARTIQ software are both open-source, in contrast to most commercially available control systems, which matches the design philosophy of an open source, open access quantum information processing platform. Finally, the modular nature of the Sinara hardware enables us to tailor a Sinara control system to the specific requirements of our particular apparatus.

While Sinara hardware is open-source, we obtained our system from M-Labs[4] to ensure high-quality construction and ongoing technical support.

4.1.1 Sinara Hardware

The Sinara hardware emits and detects a variety of electrical signals with nanosecond precision. It is composed of several control cards based on field-programmable gate array (FPGA) technology. FPGAs provide greater speed than central processing units (CPUs) in computers by executing operations directly in hardware circuits without intervening commands from an operating system. Crucially, FPGAs retain flexibility by allowing the user to reconfigure the gates and circuits on the hardware to perform different operations. The configuration is specified by a program called *gateware*. The process of putting new gateware on to an FPGA is colloquially called *flashing* the FPGA.

Sinara systems are composed of multiple different hardware cards that perform different functions in the QuantumIon apparatus. A central control card called a Sinara 1124 Carrier "Kasli"[5] receives the experiment instruction set and distributes control signals to other *daughter* cards that emit or detect electrical signals. The Kasli also implements a *softcore processor* that can perform basic computations on the device. Kasli cards communicate with daughter cards via Eurocard Extension Module (EEM) connections and communicate with the host server over Ethernet with an adapter to a Small Form-factor Pluggable (SFP) network interface module.

Each Kasli can directly control a limited number of daughter cards. If more control channels are required than can be controlled through a single Kasli card, multiple Kasli

[3] https://www.nist.gov/pml/time-and-frequency-division/ion-storage
[4] https://m-labs.hk/
[5] https://github.com/sinara-hw/Kasli

cards can be networked together via SFP to form a tree network topology where Kasli cards are internal nodes and signal cards are terminating leaves (Figure 4.3). In this configuration, the central Kasli card still performs all control operations and the downstream Kaslis act as signal routers. Future versions of the ARTIQ control framework plan to implement distributed controls across multiple Kasli cards.

Sinara control systems fit in rack-mountable chassis and are mounted in the electrical racks in our apparatus (Figures 3.1b, 4.2).

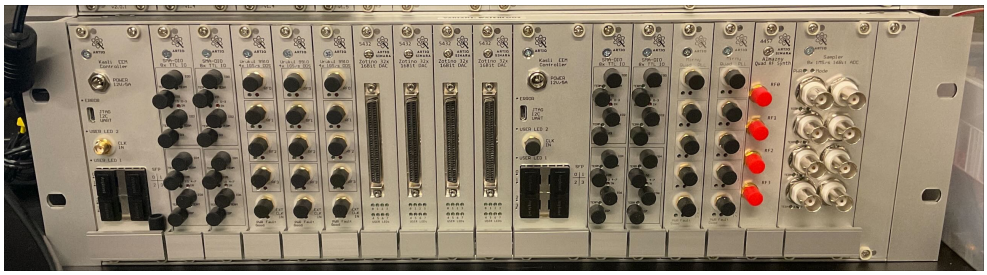

Figure 4.2: Photograph of the Sinara control system in the QuantumIon apparatus. Each Kasli control card directly controls the signal cards located to the right of the respective Kasli. The leftmost card is the master control Kasli which connects to the control server via Ethernet and connects to the auxiliary Kasli to the right via fiber optic cable assembly.

System Specification

The Sinara hardware is modular and may be specified by the user and tailored to a specific apparatus. The Sinara control system currently installed in the QuantumIon apparatus is specified to control the components required to trap, cool, and image $^{133}Ba^{+}$ ions. The control hardware will need to be augmented with additional control cards to implement full operations required for a quantum information processor.

The electrical components and circuits detailed in Chapter 3 are driven by and emit a variety of electrical signal types. Most of those circuits are controlled by Sinara control cards. RF signals are driven by Sinara 4410 DDS "Urukul"[6], Sinara 4456 microwave synthesizer "Mirny"[7], or Sinara 4457 high-frequency RF synthesizer "Almazny" mezzanine cards[8], depending on the frequency of the signal. DC voltages are supplied by the Sinara

[6] https://github.com/sinara-hw/Urukul
[7] https://github.com/sinara-hw/mirny
[8] https://github.com/sinara-hw/Almazny

5432 DAC "Zotino" cards[9]. DC signals emitted by components are detected by the Sinara 5108 "Sampler" ADC card[10]. Digital input and output signals are detected and emitted by Sinara 2128 8-channel isolated TTL/DIO cards[11].

Table 4.1 presents a manifest of components driven by the real-time Sinara control hardware and the channels required to control them. Table 4.2 shows how many of each Sinara card are necessary to satisfy the number of required channels. Finally, Table 4.3 summarizes the specification of the Sinara system obtained to satisfy the control requirements. The as-built system differs in capability slightly from the requirements for the full control system. The differences account for the realities of near-term integration and testing of the apparatus to trap the first ions. We plan to expand the control system in the future to implement a full trapped ion quantum information processor.

There are slightly fewer digital input/output (DIO) channels than specified because of limited performance requirements for the ion detection system (Section 3.3) in the near future. We do not plan to use all of the APDs to detect a full chain of 16 ions immediately. Instead, we currently use PMTs and, soon, the ion camera, so less digital input channels are required. Each SMA TTL/DIO card has eight DIO channels that can be configured for input or output in blocks of four with gateware. Therefore, we allocated available space in the Sinara chassis to implement all the digital output channels required for the initial trapping experiments and may allocate more channels for digital input later as necessary.

The system has an extra Urukul card to support not only the current requirements for trapping and global quantum operations, but to rapidly build future capabilities. Specifically, the extra card allows for another AOM channel for a 614 nm shelving repump laser in the future and supports the EOM modulation frequencies for $^{133}Ba^{+}$ and $^{137}Ba^{+}$.

The number of cards required for the apparatus in the near term is greater than the number that can be controlled by a single Kasli card. Therefore, multiple Kasli cards are included in the system. The system design balanced the number of signals required against a near-term preference to contain the entire real-time control hardware in a single rack crate. Figure 4.3 diagrams the control topology of the as-built Sinara hardware system.

The Sinara real-time control system described in this section has been delivered and installed in the apparatus. We currently use it for ion trapping experiments. The system will require expansion to at least one more crate to support full quantum operations. More DIO and RF signals are required for the shelving repump laser and Raman individual

[9] https://github.com/sinara-hw/Zotino
[10] https://github.com/sinara-hw/Sampler
[11] https://github.com/sinara-hw/DIO_SMA

Subsystem	Component	Function	Signal Type	Quantity
Ion trap	Trap DC electrodes	Static DC potential	DC (out)	96
	Trap RF electrodes	RF pseudopotential	RF @ MHz	1
Ion loading	Laser trigger	Laser ablation	Digital (out)	1
	Shutter		Digital(out)	2
	AOM	Photoionization	RF (MHz)	1
	Shutter		Digital (out)	2
Laser cooling	EOM	Doppler cooling	RF (GHz)	3
	RF switch		Digital (out)	3
	AOM		RF (MHz)	3
	Shutter		Digital (out)	2
	EOM	Repump	RF (GHz)	3
	RF switch		Digital (out)	3
	AOM		RF (MHz)	3
	Shutter		Digital (out)	1
Ion Detection	PMT	Singe photon detection	Digital (in)	3
	APD		Digital (in)	16
Laser preparation	Piezo mirror	Laser alignment	DC (out)	12
	Photodiode		DC (in)	4
	Etalon	Tune laser frequency	DC (in)	2
	Flip mirror	Laser routing	Digital (out)	6

Table 4.1: Manifest of the components driven by the Sinara hardware. These components are sufficient for trapping ions, but not for full quantum operations. Peripheral components are not listed.

addressing system. Additional DC input signals are necessary for fully monitoring the entire optical system as designed.

4.1.2 Advanced Real-Time Infrastructure for Quantum Physics

The Sinara hardware is controlled with software scripts using Advanced Real-Time Infrastructure for Quantum Physics (ARTIQ) [13]. ARTIQ is a software technology that enables users to control quantum experiments by scripting in the Python programming language[12] [119]. It compiles instructions from the script to commands for the real-time

[12] https://www.python.org/

Signal Type	Channels	Sinara Card	Card Capacity	Required Cards
Digital (out)	20	SMA TTL/DIO	8	3
Digital (in)	19	SMA TTL/DIO	8	3
RF @ MHz	8	Urukul	4	2
RF @ GHz	6	Mirny	4	2
		Almazny	4	1
DC (out)	108	Zotino	32	4
DC (in)	6	Sampler	8	1

Table 4.2: Requirements for electrical signals and Sinara cards for the real-time control system. These requirements are drawn from the components that demand real-time control (Table 4.1). One of the EOM modulation frequencies is greater than the Mirny can generate, so an Almazny is required for that single frequency.

Sinara Card	Signal Type	Card Quantity	Total Channels
SMA TTL/DIO	Digital (in/out)	4	32
Urukul	RF @ MHz	3	12
Mirny	RF @ GHz	2	8
Almazny	RF @ GHZ	1	4
Zotino	DC (out)	4	128
Sampler	DC (in)	1	8
Kasli	Control	2	-

Table 4.3: Specification for the Sinara real-time control hardware in the QuantumIon apparatus. The number of cards requires at least two Kasli cards to control. The control system will be expanded to add capabilities in the future.

hardware to execute and mediates synchronous and asynchronous communication between the host (server) and devices (Sinara real-time hardware and peripherals). For an excellent overview of how ARTIQ is structured and can be used to define and execute quantum information experiments on trapped ion systems, see [97].

All ARTIQ experiments are formatted as Python *classes* that perform experiment steps through *methods* of the class. The methods must implement a `build()` method that defines which *devices* (channels on Sinara cards and peripherals) will be used in the experiment. The available devices are detailed in a mandatory `devicedb.py` file that describes all of the cards and channels in the specific Sinara hardware system and their capabilities. The devices selected for use in the experiment are loaded and saved as class attributes in a

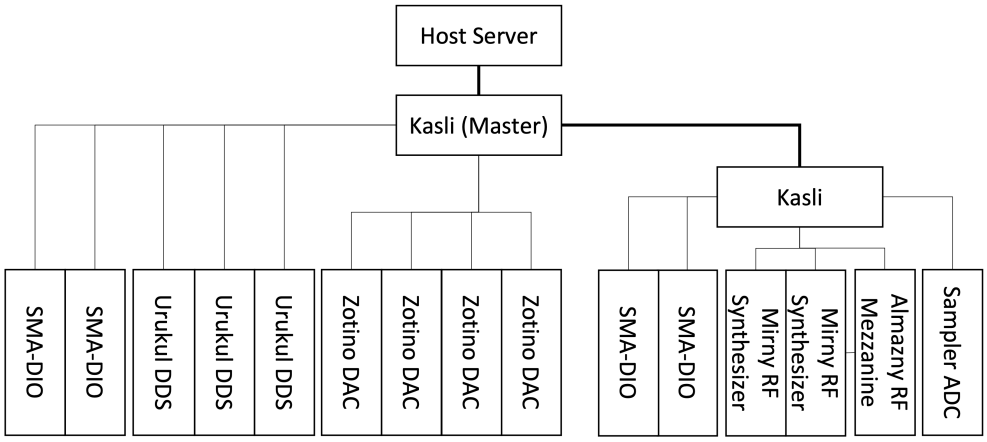

Figure 4.3: Diagram of the control topology of the Sinara control hardware. Experiment controls originate in the host server as user-written ARTIQ experiment software scripts. The commands are send to the master Kasli card, which executes commands by sending control signals to daughter cards and reading signals returned by those cards. Some cards are directly controlled by the master Kasli. Others are controlled by signals relayed through an auxiliary Kasli card.

`build()` method. The class must also implement a `run()` method which contains the main experiment commands that run on the Sinara hardware and host.

The experiment class may optionally implement a `prepare()` method for data pre-processing and set up and/or an `analyze()` method for post-processing. Both methods are required to execute on the host. Mandatory execution on the host enables *pipelining* experiments. While an experiment is executing on the device, the previous experiment may be analyzed and the next experiment may be prepared simultaneously. See Listing 4.1 for a toy example of an ARTIQ experiment definition.

ARTIQ achieves real-time performance by preparing commands with specific timestamps that dictate when the command should be executed. The system maintains a *timeline* of experiment commands with specific execution timings that is checked against a *wall clock* that evaluates time since the experiment began[13] (Figure 4.4). New commands are added at the position of the timeline *cursor*, which then moves forward by the duration of the command that has been added. When the wall clock reaches a command on the timelines, the command is executed on the hardware. The difference between the cursor and the wall clock is known as *slack*. Commands may be added dynamically during experiments,

[13] https://www.m-labs.hk/artiq/manual/rtio.html

```
from artiq.experiment import *

class ExampleExperiment(EnvExperiment):
    """Experiment classes must subclass from ARTIQ EnvExperiment"""
    def build(self):
        """Define devices used in the experiment"""
        self.setattr_device("core") # required in all experiments
        self.setattr_device("ttl0") # digital output channel
        self.setattr_device("ttl1")

    def prepare(self):
        """Set up on host"""
        pass

    def run(self):
        """Execute experiment"""
        self.core.reset()
        self.ttl0.pulse(1*us)
        self.ttl1.pulse(1*us)

    def analyze(self):
        """Data post-processing"""
        pass
```

Listing 4.1: Example simple ARTIQ experiment class definition.

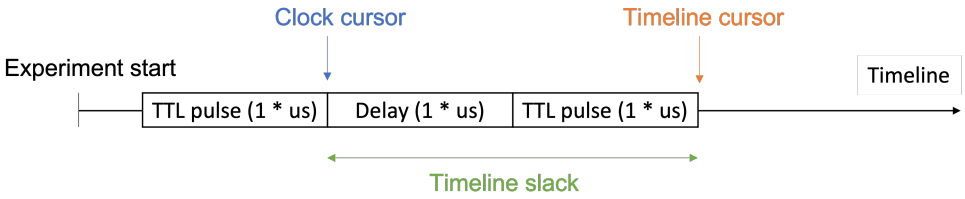

Figure 4.4: Diagram of the ARTIQ command timeline. The timeline and cursors proceed from left to right. Commands are added to the timeline at the position of the cursor, advancing the cursor along the timeline by the duration of the command. Once the clock reaches a command, it is executed in real-time on the hardware.

but the cursor must stay ahead of the wall clock during execution. Otherwise, commands will be added to the timeline after the wall clock has passed, resulting in an error. The timeline and clock are counted on a 125 MHz clock on the Sinara hardware. Alternatively, an external clock that operates at a different rate may be used. The increments at which the timelines are divided are known as *machine units*. The time at which commands begin and their duration may be expressed in either machine units or International Standard of Units (SI) time units.

A core ARTIQ concept is the difference between *host* and *kernel* methods. Host methods are executed on the computer on which the script is run and kernel methods are executed on the Sinara hardware. All methods are host methods by default. Kernel methods are designated by the `@kernel` *decorator*[14]. Additional decorators explicitly require the method to execute on the host (`@host_only`), execute on the host with modifications such as specifying an asynchronous call (`@rpc`), or execute on the same device as its caller (`@portable`)[15].

Kernel methods are compiled to the real-time hardware. Therefore, they must be written with a strict subset of the Python language defined by ARTIQ[16]. The subset implements specific data types and a restricted set of basic Python data structures and functions. Kernel methods must run on the real-time hardware, which motivates the restriction for storage and performance optimization of the language subset. Kernel methods may make remote procedure calls (RPCs) to perform more expensive operations on or send/retrieve data to/from the host. RPCs are not guaranteed to obey real-time restrictions.

[14] https://peps.python.org/pep-0318/

[15] https://m-labs.hk/artiq/manual/core_language_reference.html#module-artiq.language.core

[16] https://m-labs.hk/artiq/manual/compiler.html

Experiments often require two or more channels on the control system to emit or detect signals simultaneously. ARTIQ supports parallel operations on the Sinara hardware with context managers using the `parallel` keyword. All operations within a `parallel` context begin simultaneously. The `parallel` context lasts as long on the timeline as the longest command within the context. If some commands must be executed sequentially while others operate in parallel, a context manager with the `sequential` keyword may be used to describe which commands occur sequentially within a `parallel` context. See Listing 4.2 for an example of how the `parallel` and `sequential` contexts work[17].

ARTIQ also provides multiple tools for managing the real-time hardware. A key tool is the dashboard[18] which provides a graphical user interface (GUI) to control the apparatus (Figure 4.5). The dashboard allows users to select scripts to run, change important experimental parameters without modifying the source code, set multiple jobs to run in sequence, and plot and display data acquired as part of the experiment. A graphical interface makes operation of the apparatus simpler and more approachable.

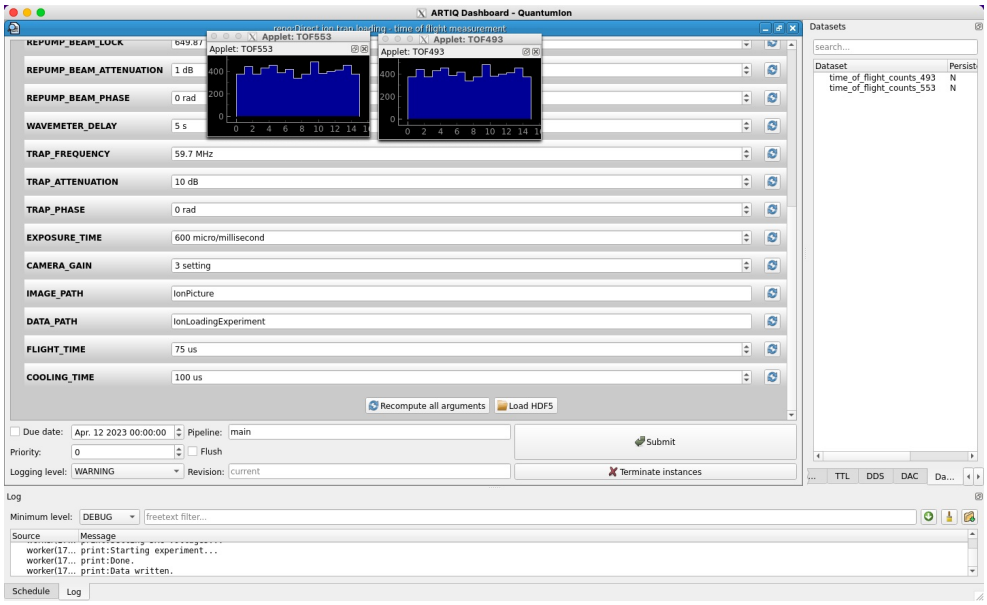

Figure 4.5: Screenshot of the ARTIQ dashboard application. The dashboard provides a graphical interface to the control system.

[17] https://m-labs.hk/artiq/manual/getting_started_core.html?highlight=parallel#parallel-and-sequential-blocks

[18] https://m-labs.hk/artiq/manual/management_system.html#dashboard

```
from artiq.experiment import *

class ParallelExample(EnvExperiment):
    def build(self):
        self.setattr_device("core")
        self.setattr_device("ttl0")
        self.setattr_device("ttl1")

    def run(self):
        # emit two sequential 1 microsecond pulses on the same channel
        self.ttl0.pulse(1*us)
        delay(1*us)
        self.ttl0.pulse(1*us)

        # two sequential 1 microsecond pulses on different channels
        self.ttl0.pulse(1*us)
        delay(1*us)
        self.ttl1.pulse(1*us)

        # two simultaneous 1 microsecond pulses on different channels
        with parallel:
            self.ttl0.pulse(1*us)
            self.ttl1.pulse(1*us)

        # one 3 microsecond pulse simultaneous with
        # two sequential 1 microsecond pulses on a different channel
        with parallel:
            self.ttl0.pulse(3*us)
            with sequential:
                self.ttl1.pulse(1*us)
                delay(1*us)
                self.ttl1(1*us)
```

Listing 4.2: Example usage of sequential and parallel blocks in ARTIQ.

Duke ARTIQ Extensions

ARTIQ provides a very low-level interface to the control system. All operations must be expressed in terms of which channel on which card must activate with precise timing. The user must recall and/or manually record the mapping of signal channels to experimental components, which becomes difficult for large apparatuses and complex experiments.

The Duke ARTIQ Extensions (DAX)[19] are a set of software packages that seamlessly extend the capabilities of ARTIQ control systems to make programming and using them more user-friendly [94]. DAX allows users to raise the level of abstraction of the control system by introducing *modules* and *services*. Modules are collections of signal channels that collectively implement a single conceptual component of an apparatus. An example of a module is a class that encapsulates the RF and DC control channels to create a trapping potential with the ion trap. Services are functions that implement high-level procedures that are common on ion trap by controlling one or modules. An example of a service is laser cooling one or more ions.

DAX also implements additional packages that provide other helpful tools for ARTIQ control systems. The packages include tools for expressing experiments, such as a scheduler, a scanning experiment framework, and a gate-level interface for quantum circuit experiments. Also included are tools for better controlling hardware, such as servo motor control and a Sinara hardware simulator [95].

The QuantumIon apparatus currently implements a vanilla ARTIQ control system. Experiments are all expressed as ARTIQ scripts controlling signal channels directly. We use the DAX Sinara hardware simulator to prototype experiment scripts. Future iterations of the control system will use DAX to implement modules and services for better apparatus control and quicker experiment design and scripting.

4.2 Peripheral Device Control

Several devices in the ion trap apparatus do not need to be controlled with real-time precision. A subset of those devices operate constantly with the same or seldom-changing parameters and are not integrated into the control system all. The vacuum chamber pumps and the magnetic field coils are examples of such devices. Other devices require computer control through the control system for convenience, monitoring, or because they

[19] https://gitlab.com/duke-artiq/dax

have no other control interface, but execute processes with more relaxed time requirements. Those devices are integrated into ARTIQ-based control software through an ARTIQ defined-paradigm called the Network Device Support Package (NDSP)[20]. The devices in the QuantumIon apparatus that fit this control paradigm are the wavemeter, ion camera, and select motor controllers.

4.2.1 Network Device Support Packages

Network Device Support Packages (NDSPs) are programs that wrap non-ARTIQ hardware devices in software layers that allow ARTIQ experiment scripts to call and control those devices just like a Sinara device. The controllers implement direct communication with and expose remote procedure call (RPC) interfaces for the hardware devices, allowing the ARTIQ scripts to communicate with a known interface. The NDSPs must be entered into the `devicedb.py` just like the Sinara devices. The open-source community that supports ARTIQ maintains a list of NDSPs that have been developed and shared by the community[21].

The advantages of NDSPs are numerous. The interface allows the peripheral hardware to be controlled in the same manner as Sinara devices, simplifying the task of programming experiments in ARTIQ (Listing 4.3). The RPC interface (implemented with the SiPyCo package[22]) enables communication between the ARTIQ control software and NDSPs over a network. Thus, NDSPs need not be installed in the same environment, or even on the same computer as the control program. The networking capability simplifies software implementation by allowing each NDSP to run in its own environment, reducing integration issues and software dependency conflicts. Hardware implementations can also be simplified by removing the requirement that all devices be directly connected to a single host computer as long as all computers are networked together. NDSPs can be executed individually, or invoked by ARTIQ scripts.

An NDSP includes at minimum a *driver* which implements control over a hardware devices and a *controller* which invokes the driver and handles communication over the network with the ARTIQ control software. Optionally, a *client* may expose the driver as a general too with a command line interface (CLI) and/or a *mediator* may integrate limited real-time control or otherwise expand the interface or capability of the NDSP.

[20] https://m-labs.hk/artiq/manual/developing_a_ndsp.html
[21] https://m-labs.hk/artiq/manual/list_of_ndsps.html
[22] https://github.com/m-labs/sipyco

```
from artiq.experiment import *

class PeripheralExample(EnvExperiment):
    def build(self):
        self.setattr_device("core")
        self.setattr_device("ttl0") # Sinara device
        self.setattr_device("wavemeter") # peripheral device

    def run(self):
        self.core.reset()
        self.ttl0.pulse(1*us)
        self.wavemeter.get_frequency(channel=1)
```

Listing 4.3: Example of how a device implemented in an NDSP is added to an ARTIQ script. The Sinara hardware device and the peripheral NDSP use the same declaration syntax. The NDSP configuration information is read from the device database.

4.2.2 Wavemeter

The HighFinesse WS8-2 wavemeter (Section 3.2.2) has two control methods. The vendor ships a standalone GUI control application that runs on Windows[23] and Linux[24] operating systems. We use this program for initial setup, calibration, and testing of the wavemeter. It includes information displays that are very informative during initial experiments (Figure 4.6). The vendor also provides a compiled C programming language library [58] (for both Windows and Linux) that handles connecting to the wavemeter over the network and exposes the application programming interface (API) for the wavemeter hardware. Additionally, the vendor delivered a compatibility layer for calling the control library from Python scripts. We favor the Python interface because it allows us to control the wavemeter from an ARTIQ experiment script.

The Python compatibility layer for the control library is rudimentary and directly exposes the C API, which uses concepts such as pointers and error codes that are inimical to Python programming. The API also includes unused arguments in functions and obsolete functions. To promote ease of use in experiment scripts, we developed a Python wrapper package that the mediates connection and provides a more Pythonic interface to the wavemeter.

The first implementation was a simple package that required integration into the en-

[23] https://www.microsoft.com/en-ca/windows
[24] https://www.linux.org/

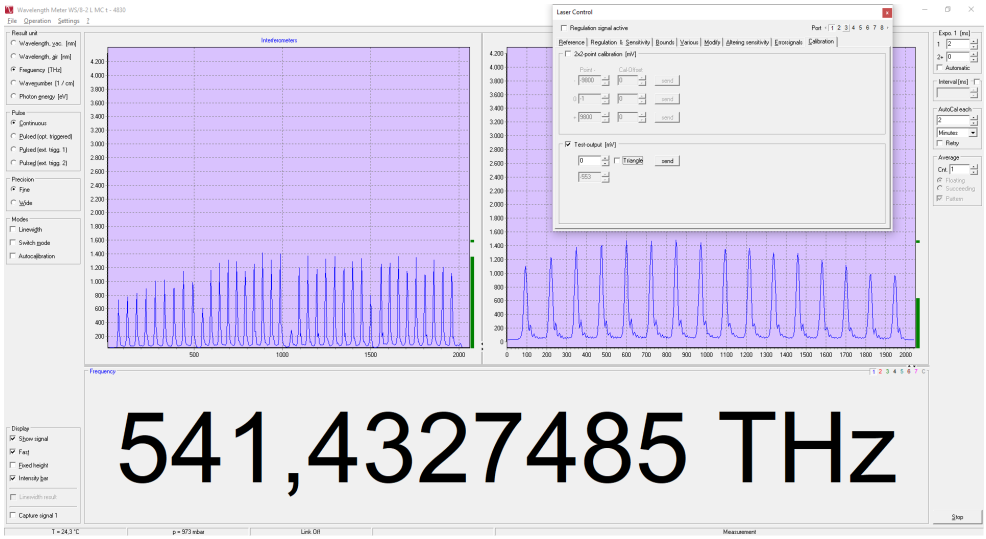

Figure 4.6: Screenshot of the display for the control program for the WS8-2 wavemeter. The wavemeter can also be controlled from custom control software.

vironment that encompasses the ARTIQ software and experiment scripts. The wavemeter package must be separately imported and a class must be instantiated in experiment scripts in a manner distinct from other Sinara devices. Challenges with the wavemeter package have motivated a greater commitment to using NDSPs for peripheral devices and we now have a wavemeter NDSP under development. Alternately, a potential open-source implementation may be available[25].

Laser Controllers

The AOSense laser controllers with which the wavemeter communicates to lock the lasers (Section 3.2.2) also have their own standalone control application. That control application provides a GUI to monitor and control laser parameters (Figure 4.7). When set up to lock the lasers with feedback from the wavemeter, this control program need not be used, though it may provide helpful monitoring capability. Similarly, the laser controllers do not need to be controlled directly from an ARTIQ control script because control is mediated by the wavemeter.

[25] https://github.com/quartiq/highfinesse-net

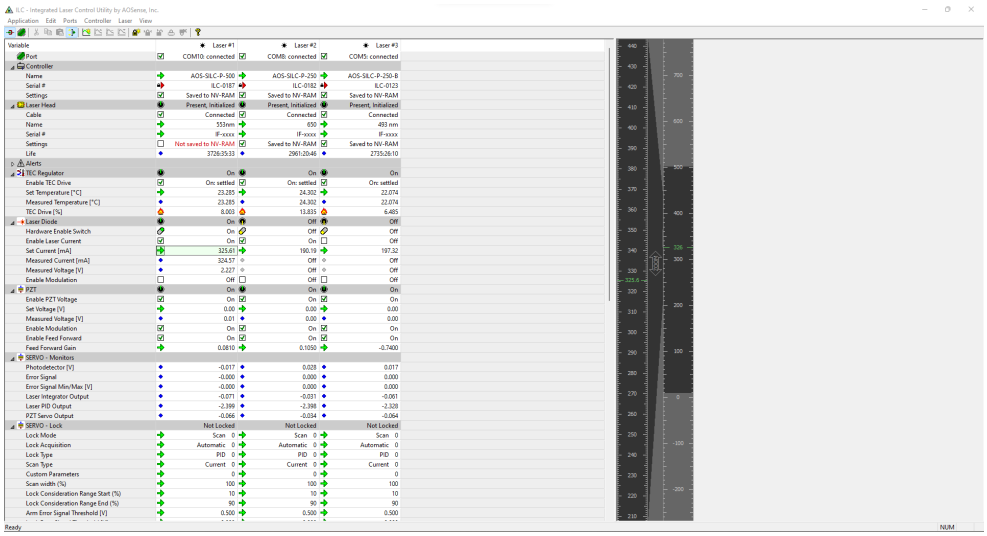

Figure 4.7: Screenshot of the AOSense laser controller control system display. Additional control is possible via the wavemeter.

4.2.3 sCMOS Ion Camera

Similarly to the wavemeter, the ion camera (Section 3.3.2) ships with both a GUI application and a compiled library (in the C++ programming language [116]) for controlling the device. Full official support is provided for Windows versions of both control methods, though the vendor also provides Linux-compatible versions with limited support. Additionally, the vendor provides an open-source Python wrapper for the control library called PyVCam[26] which requires a software development kit (SDK)[27] that the vendor provides upon request. The SDK requirement leads to an odd manual installation process that makes automated deployment of the package difficult, further motivating implementation of an NDSP for the ion camera.

The PyVCam package very nearly provides an appropriate driver for an NDSP. Unfortunately, the use of `@property`[28] decorators in PyVCam turns out to be incompatible with SiPyCo procedures. Therefore, we implemented an NDSP with a driver and controller for the ion camera that wraps PyVCam and exposes a simpler interface.

[26] https://github.com/Photometrics/PyVCAM

[27] https://www.photometrics.com/support/download/pvcam-sdk

[28] https://docs.python.org/3.8/library/functions.html#property

4.2.4 Motor Controllers

Motor controllers (Section 3.2.5) usually come with vendor-provided control applications with GUIs and often control libraries as well. In many cases, motor controller interfaces are restricted to the Windows operating system.

Open-source NDSP packages are available for the Newport New Focus 8742 Picomotor controller[29] and the Newport Agilis AG-UC8 motor controller[30]. Control implementations for Thorlabs instruments that are controlled by K-Cubes are under consideration. Open-source packages that control T-Cubes[31] may be adaptable to K-Cubes. We plan to use the available programs and adapt them as necessary to our apparatus.

4.3 Application Server

The host computer for the QuantumIon apparatus is a server mounted in an electrical rack of the apparatus. We chose a server architecture to provide the processing power to coordinate the experiment and analyze data, provide storage for calibration and experimental data, and so that the computer would fit into an electrical rack with the rest of the control system and electrical infrastructure. The server should also be more robust than a desktop and eventually enable remote access and operation of the apparatus as a service center.

4.3.1 Hardware

The control server is a Dell PowerEdge R750xs rack server[32]. It was chosen to provide the power and storage necessary for initial implementation of the QuantumIon apparatus. The key specifications for the processing, storage, networking, and administration capabilities of the server are:

- Public-facing server
- Intel Xeon Silver 12C/24T processor
- 2 Rack Unit height

[29] https://github.com/quartiq/newfocus8742
[30] https://github.com/OregonIons/AGUC8
[31] https://github.com/m-labs/thorlabs_tcube
[32] https://www.dell.com/en-ca/shop/cty/pdp/spd/poweredge-r750xs

- 64 GB RAM
- 16 GB/sec Fibre Channel HBA card
- 2x 10GBe Ethernet ports via SFP+ or QSFP+
- 1x GBe Ethernet
- At least 6 drive bays
- 3 drives with carriers, 7200K min, 900GB min, SATA or SAS
- USB 3.1 card
- iDRAC or similar out-of-band console
- At least 1 full size/full height empty slot for OSS PCIe3.0 fibre extender
- At least 2 consecutive full size/full height slot for future GPU
- RAID 5 card

Corresponding technical details for the server are listed in Table 4.4. The server does not currently satisfy all requirements, but supports later addition of components to do so.

Component	**Part**
Chassis	2 rack units
CPU	Intel Xeon Silver 4310 2.1G
RAM	16GB RDIMM, 3200MT/s, Dual Rank
Storage	1.2TB Hard Drive 12Gbps 2.5in with 3.5in HYB CARR, no RAID
Capacity	3.5” Chassis with up to 8 Hard Drives (SAS/SATA), 1 CPU
Networking	Emulex LPE 35002 Dual Port 32 Gb Fibre Channel HBA, PCIe Low Profile
Administration	iDRAC9, Enterprise 15G
Expansion space	Riser config 4, Half Length, Low Profile, 1x16 + 1x4 slots, 1 CPU
Heatsink	Standard

Table 4.4: Key components of the Dell PowerEdge R750xs host server.

4.3.2 Software

The control server is both the main operation platform and main development environment for the control system for the QuantumIon apparatus control system. It currently has a provisional configuration that we expect to iterate on during control system development and freeze once the QuantumIon apparatus is made available as a service center. Development of the system will proceed on a different platform and deploy to the server as required. Table 4.5 summarizes the software technologies and tools used in (the development of) the QuantumIon control system.

Technology	Purpose	Version
Linux	Kernel	5.19.0-46-generic x86_64
Ubuntu	OS	22.04.2 Jammy Jellyfish LTS
ARTIQ	Quantum control system	7.8160.81dbbd0
Nix	Environment, package manager	2.12.0
Git	Source code version control	2.34.1

Table 4.5: Summary of the software technologies and tools used to develop the quantum control system for the QuantumIon apparatus.

Operating System

We chose a Linux distribution as the operating system (OS) for the control server because Linux OSs have numerous advantages for computational systems. Linux OSs are more configurable, lightweight, scalable, and controllable than Windows, which has resulted in Linux being adopted as the OS for numerous cloud services, high-performing computing platforms and service servers. Windows systems (at least on desktops) are known to push mandatory updates which require system reboots, potentially interrupting experiments and breaking software dependencies. In contrast, Linux systems only update and reboot on command from the administrator. Finally, most common software development tools (Section 4.3.2) are native to and work more straightforwardly on Linux.

The control server current runs Ubuntu 22.04.2 Jammy Jellyfish LTS[33] OS (desktop) built on the GNU/Linux 5.19.0-46-generic x86_64 kernel. We chose Ubuntu during the development cycle because it is easy for users new to Linux distributons to install, configure, and operate, and it has both desktop and server configurations. During development, we

[33] https://www.releases.ubuntu.com/jammy/

use the desktop version of the OS because it comes with tools designed to easily operate the computer, primarily featuring a GNOME GUI[34]. Later, we will redeploy the system on the server version of Ubuntu so that we can take advantage of server architecture optimizations with (hopefully) minimal integration issues.

Development Technologies

We employ several industry standard software development tools and technologies in building the QuantumIon control system software. The choice of technologies is partially mandated by the use of ARTIQ software. ARTIQ is deployed as a Python package with the Nix environment and package manager[35]. Git[36] is the standard tool for version control on software projects. See [97] for an excellent discussion of the application of these software engineering tools to scientific computing, in particular when developing TIQC apparatuses. We follow similar procedures when developing the code for the control system.

4.4 Full Stack Quantum Controls Framework

Control systems for quantum computers are usually quite complicated and difficult for non-expert users to operate. The difficulty arises from the inherent complexity of the control requirements of quantum information processing devices and the fact current quantum hardware is sufficiently new to not be standardized. As a result, each device has near-unique capabilities and control requirements. A standardized and appropriately abstracted quantum controls framework would improve the quality and speed of laboratory work and make quantum hardware accessible to non-expert users. Therefore, we are in the early stages of designing a full stack quantum controls framework for the QuantumIon Project and, hopefully, wider adoption.

The traditional software stack for an application often distinguishes between the components that primarily implement the user interface and experience (UI/UX) and those that primarily implement the main computational logic. The user-facing components are known as the *front end* while the main logic components are known as the *back end*. A program (and/or programmer) that implements both parts of the system is referred to as *full stack*. Thus, a full stack quantum control program provides a mature user interface

[34] https://www.gnome.org/
[35] https://nixos.org/
[36] https://git-scm.com/

to the quantum hardware, often in the form of a high-level programming language, and translates the commands given in the control interface to operate the quantum hardware.

The quantum control system for the QuantumIon Project must satisfy two core design requirements:

1. Expose experimental control at multiple levels of abstraction to allow users to interact with the system at their level of expertise
2. Easily port between different TIQC apparatuses with minimal configuration

A major barrier to research in the field of quantum information is access to high-quality quantum hardware. A control system that allows users at varying levels of expertise in quantum computing and ion trapping to easily operate our apparatus will enable our current and future collaborators to run exciting physics and computing experiments. The system will also accelerate our lab work by allowing us to define and express experiments at the level of abstraction most native to the experiment. Thus, the front end must expose experimental control at multiple levels of abstraction.

Early-stage quantum computers are all prototype devices with slightly different capabilities and therefore slightly different control requirements. Building a new custom control program from scratch for each system is onerous. We aim to build a system that can be quickly installed on new TIQC apparatuses with minimal configuration. Thus, the back end must be a framework that is straightforwardly configurable to a specific TIQC while providing a stable interface for hardware control.

The requirements indicate that our control system must be a full stack quantum control framework that implements novel capabilities in experiment abstraction and hardware control. Additionally, we intend for this full stack quantum control framework to be provided to the wider quantum computing community as an open source project.

Many other organizations developing quantum computing hardware and software have built and distributed quantum control software targeting various levels of the quantum computing stack. A non-exhaustive list of available control programs is presented in Table 4.6. Unfortunately, none of these control programs satisfies all of our requirements. Several systems do not adequately fulfill the control requirements for TIQCs, others are tightly bound to specific control hardware and/or are not entirely open source, and most only provide a single level of abstraction that is too high (quantum gate layer) or too low (individual hardware channel) for our needs. Therefore, we are designing our own full stack quantum control framework.

Quantum Control Program	Developer
Qiskit[37]	IBM
Cirq[38]	Google
TKET[39]	Quantinuum
Bloqade[40]	QuEra
ARTIQ[41]	M-Labs
DAX[42]	Duke Quantum Center
JAQAL[43]	Sandia National Laboratories
Pennylane[44]	Xanadu
Boulder Opal[45]	Q-CTRL
Qua[46]	Quantum Machines
QCS[47]	Keysight
Quil[48]	Rigetti

Table 4.6: A non-exhaustive survey of quantum control programs available for use. Many have convenient features, but none fulfill all needs for our control program. We will borrow open-source technologies as possible.

While we are building a new system, we intend to learn and borrow from other successful programs. Our framework will be developed on top of the ARTIQ and DAX technologies and we hope to integrate JAQAL [62, 70, 82] as is appropriate. Additionally, we plan to replicate and/or support syntax from successful systems such as Qiskit [19, 28, 29].

The preliminary design of the full stack quantum control framework features four layers of abstraction: the gate layer, the Hamiltonian layer, the atomic physics layer, and the bare metal layer (Figure 4.8). Each layer defines its own syntax for describing experiment control and flow, so each represents a possible entry point for the user. The higher layers are

[37] https://qiskit.org/
[38] https://quantumai.google/cirq
[39] https://www.quantinuum.com/developers
[40] https://www.quera.com/bloqade
[41] https://m-labs.hk/experiment-control/artiq/
[42] https://gitlab.com/duke-artiq/dax
[43] https://www.sandia.gov/quantum/quantum-information-sciences/projects/qscout-jaqal/
[44] https://xanadu.ai/products/pennylane/
[45] https://q-ctrl.com/boulder-opal
[46] https://www.quantum-machines.co/technology/qua-universal-quantum-language/
[47] https://www.keysight.com/ca/en/products/modular/pxi-products/quantum-control-system.html
[48] https://docs.rigetti.com/qcs/guides/quil

more abstract and enable better ease of use while sacrificing degree of control. The lower layers, conversely, enable finer control but are more difficult or inaccessible to non-expert users.

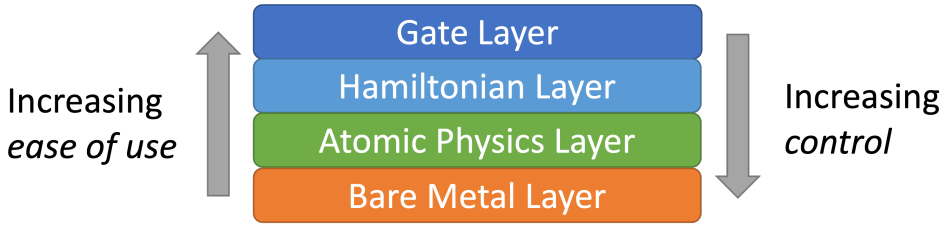

Figure 4.8: Conceptual design of the full stack quantum control framework. Multiple layers enable multiple methods for controlling the apparatus. Experiment abstraction requires a trade-off between experiment control and ease of use.

The top gate layer exposes an interface that implements the well-known quantum circuit model [84]. It is the simplest interface at the highest level of abstraction. The user may specify a number of qubits, apply a set of predefined (potentially parameterized) quantum gates to the qubits, then measure the qubits. The target user is anyone with an interest in quantum computing.

The Hamiltonian layer provides an interface for defining semi-arbitrary operators for quantum dynamics on trapped ion qubits. The operators must be able to be implemented on trapped ions and may be time independent over a user-set duration or time-dependent. The target user is an informed physicist interested in quantum simulation of quantum many-body dynamics.

The atomic physics layer has an interface defined in terms of atomic behavior and dynamics. The parameters will be properties such as the Rabi flopping rate and will be specific to the ion species used in the underlying ion trap. The target user is an expert atomic and molecular optics physicist performing specific atomic physics experiments or performing diagnostics, calibrations, and/or implementing improvements on the apparatus.

Finally, the bare metal layer provides direct control to the hardware of the ion trap. The parameters are physical properties such as voltages in circuits or intensities of layers. This is the most complicated and dangerous control layer. The target user is a trained member of the laboratory team physically in the lab with the apparatus building new capabilities into the system.

Definition of multiple control interfaces at multiple levels of abstraction accomplishes exposing appropriate control to users with different levels of expertise. The gate, Hamilto-

nian, and atomic physics layers should all be easily portable between different apparatuses. The bare metal layer will require configuration for each individual apparatus, accomplishing significant portability between apparatuses.

Significant work remains on the definitions of the interfaces for all layers and the underlying architecture of the program. The four interfaces described above all constitute front end components. While the higher layers of the framework are all conceptually subsets of the lower layers, we do not anticipate translating between the layers. Instead, each layer will compile to an intermediate representation which will then be fed to the bare metal layer or to the quantum hardware directly. The bare metal layer will assume that the underlying control hardware technology for the apparatus is ARTIQ/DAX.

4.5 Assembly Status

This section describes the status of the assembly of the control system for the QuantumIon apparatus as of July 2023. The Sinara hardware (Section 4.1) and control server (Section 4.3) are set up and installed in the apparatus. The hardware passes simple functionality tests according to scripts distributed by M-Labs[49].

The server has the Ubuntu OS, ARTIQ, and all necessary software development tools installed. Initial versions of the wavemeter and ion camera NDSPs are installed on the server and behave as expected. Development of the ARTIQ control system with DAX modules and services and the NDSPs for the wavemeter, ion camera, and motor controllers remain ongoing. The full stack quantum control framework is in its preliminary design stage with limited working prototypes.

[49] https://github.com/m-labs/artiq/blob/master/artiq/frontend/artiq_sinara_tester.py

Chapter 5

Concluding Remarks

The development of the QuantumIon apparatus continues with the focus on trapping the first $^{138}Ba^{+}$ ions in the apparatus. Success will mark the achievement of trapping barium ions in a surface ion trap, a novel capability.

We are currently working on improvements to the electrical systems that will help trap the first ions. The trap RF drive circuits must be repaired by replacing the RF feedthrough pin on the vacuum chamber and tweaking the resonator so its resonance frequency matches our desired trap RF drive frequency. The trap DC circuits will be improved with the addition of new PCBs that will filter the DC electrical signals, creating a more stable confining electric potential well for the ions. While the vacuum chamber is open to repair the feedthrough, we will verify the electrical connections for the trap DC electrodes. Both the trap RF and DC circuits will connect to a fully functional Phoenix trap that we are installing in the vacuum chamber. We expect that these modifications will help us trap $^{138}Ba^{+}$ ions.

Once we have trapped the first $^{138}Ba^{+}$ ions, we are well positioned to advance to trapping $^{133}Ba^{+}$ ions as well. We plan to install a $^{133}Ba^{+}$ atomic source while the vacuum chamber is open. Combined with final installation and testing of the EOM RF drive circuits and the magnetic field coils, we will have all the capabilities necessary to trap $^{133}Ba^{+}$. With atomic sources of both $^{133}Ba^{+}$ and $^{138}Ba^{+}$ installed in the chamber, we anticipate performing dual-species ion experiments.

Significant additional capabilities are required to transform the QuantumIon apparatus from an ion trap into an trapped ion information processor. We will install a microwave horn to perform our first global single qubit rotations, followed by pulsed 532 nm Raman lasers and the planned individual addressing system to implement entangling gates [9]. The

addition of 1762 nm shelving and 614 nm shelving repump lasers will allow us to implement shelving operations, opening the door to improved SPAM protocols for $^{133}Ba^{+}$ [25] and measurement of $^{137}Ba^{+}$. All of these capabilities will require robust electrical infrastructural support and additional control system performance.

Finally, we will continue building the systems to support operation of the apparatus as a service center. The controllable devices and stages will be integrated into the control system and automated monitoring of all instruments and the apparatus environment will be implemented. We will continue to develop a full stack quantum control system interface to expose full control of the apparatus to users of different levels of technical expertise at appropriate levels of abstraction. The first priorities are defining the interfaces for each layer of abstraction and determining how to pass instructions from our program to a control system based on ARTIQ/DAX. There is much exciting work to do!

References

[1] *Chemistry: The Alkaline Earth Metals (Group 2)*. LibreTexts, jul 4 2022. [Online; accessed 2023-06-09].

[2] DTC Allcock, WC Campbell, J Chiaverini, IL Chuang, ER Hudson, ID Moore, A Ransford, C Roman, JM Sage, and DJ Wineland. Omg blueprint for trapped ion quantum computing with metastable states. *Applied Physics Letters*, 119(21):214002, 2021.

[3] E Arimondo and G Orriols. Nonabsorbing atomic coherences by coherent two-photon transitions in a three-level optical pumping. *Nuovo Cimento Lettere*, 17:333–338, 1976.

[4] Michael N R Ashfold and Colin M Western. Multiphoton Spectroscopy, Applications. In John C Lindon, editor, *Encyclopedia of Spectroscopy and Spectrometry*, pages 1424–1433. Elsevier, Oxford, 1999.

[5] CJ Ballance, TP Harty, NM Linke, MA Sepiol, and DM Lucas. High-fidelity quantum logic gates using trapped-ion hyperfine qubits. *Physical review letters*, 117(6):060504, 2016.

[6] SR Bastin and Tony E Lee. Ion crystals in anharmonic traps. *Journal of Applied Physics*, 121(1):014312, 2017.

[7] Ville Bergholm, Josh Izaac, Maria Schuld, Christian Gogolin, Shahnawaz Ahmed, Vishnu Ajith, M Sohaib Alam, Guillermo Alonso-Linaje, B AkashNarayanan, Ali Asadi, et al. Pennylane: Automatic differentiation of hybrid quantum-classical computations. *arXiv preprint arXiv:1811.04968*, 2018.

[8] DJ Berkeland, JD Miller, James C Bergquist, Wayne M Itano, and David J Wineland. Minimization of ion micromotion in a paul trap. *Journal of applied physics*, 83(10):5025–5033, 1998.

[9] Ali Binai-Motlagh, Matthew Day, Nikolay Videnov, Noah Greenberg, Crystal Senko, and Rajibul Islam. A guided light system for agile individual addressing of ba^+ qubits with 10^{-4} level intensity crosstalk. *arXiv preprint arXiv:2302.14711*, 2023.

[10] Binai-Motlagh, Ali. Robust optical engineering for a trapped ion quantum computer. Master's thesis, University of Waterloo, 2022.

[11] Rainer Blatt and Christian F Roos. Quantum simulations with trapped ions. *Nature Physics*, 8(4):277–284, 2012.

[12] Matthew J Boguslawski, Zachary J Wall, Samuel R Vizvary, Isam Daniel Moore, Michael Bareian, David TC Allcock, David J Wineland, Eric R Hudson, and Wesley C Campbell. Raman scattering errors in stimulated-raman-induced logic gates in ba+ 133. *Physical Review Letters*, 131(6):063001, 2023.

[13] Sébastien Bourdeauducq, Robert Jördens, Peter Zotov, Joe Britton, Daniel Slichter, David Leibrandt, David Allcock, Aaron Hankin, Florent Kermarrec, Yann Sionneau, Raghavendra Srinivas, Ting Rei Tan, and Justin Bohnet. Artiq 1.0, May 2016.

[14] Bramman, Brendan. Measuring trapped ion qudits. Master's thesis, University of Waterloo, 2019.

[15] Samuel M Brewer, J-S Chen, Aaron M Hankin, Ethan R Clements, Chin-wen Chou, David J Wineland, David B Hume, and David R Leibrandt. Al+ 27 quantum-logic clock with a systematic uncertainty below 10- 18. *Physical review letters*, 123(3):033201, 2019.

[16] Kenton R Brown, Andrew C Wilson, Yves Colombe, C Ospelkaus, Adam M Meier, Emanuel Knill, Dietrich Leibfried, and David J Wineland. Single-qubit-gate error below 10- 4 in a trapped ion. *Physical Review A*, 84(3):030303, 2011.

[17] Lowell S Brown and Gerald Gabrielse. Geonium theory: Physics of a single electron or ion in a penning trap. *Reviews of Modern Physics*, 58(1):233, 1986.

[18] Colin D Bruzewicz, John Chiaverini, Robert McConnell, and Jeremy M Sage. Trapped-ion quantum computing: Progress and challenges. *Applied Physics Reviews*, 6(2):021314, 2019.

[19] Lauren Capelluto and Thomas Alexander. Openpulse: Software for experimental physicists in quantum computing. *Bulletin of the American Physical Society*, 65, 2020.

[20] Y Castin, H Wallis, and Jean Dalibard. Limit of doppler cooling. *JOSA B*, 6(11):2046–2057, 1989.

[21] IC Chang. Acousto-optic devices and applications. *Handbook of optics*, 2:12–1, 1995.

[22] G Chen. On the physics of purple-plague formation, and the observation of purple plague in ultrasonically-joined gold-aluminum bonds. *IEEE Transactions on parts, materials and packaging*, 3(4):149–153, 1967.

[23] John Chiaverini, R Brad Blakestad, Joe Britton, John D Jost, Chris Langer, Dietrich Leibfried, Roee Ozeri, and David J Wineland. Surface-electrode architecture for ion-trap quantum information processing. *arXiv preprint quant-ph/0501147*, 2005.

[24] Justin E Christensen. *High-Fidelity Operation of a Radioactive Trapped-Ion Qubit, 133 Ba+*. PhD thesis, University of California, Los Angeles, 2020.

[25] Justin E Christensen, David Hucul, Wesley C Campbell, and Eric R Hudson. High-fidelity manipulation of a qubit enabled by a manufactured nucleus. *npj Quantum Information*, 6(1):35, 2020.

[26] Juan I Cirac and Peter Zoller. Quantum computations with cold trapped ions. *Physical review letters*, 74(20):4091, 1995.

[27] Susan M Clark, Daniel Lobser, Melissa C Revelle, Christopher G Yale, David Bossert, Ashlyn D Burch, Matthew N Chow, Craig W Hogle, Megan Ivory, Jessica Pehr, et al. Engineering the quantum scientific computing open user testbed. *IEEE Transactions on Quantum Engineering*, 2:1–32, 2021.

[28] Andrew Cross. The ibm q experience and qiskit open-source quantum computing software. In *APS March meeting abstracts*, volume 2018, pages L58–003, 2018.

[29] Andrew Cross, Ali Javadi-Abhari, Thomas Alexander, Niel De Beaudrap, Lev S Bishop, Steven Heidel, Colm A Ryan, Prasahnt Sivarajah, John Smolin, Jay M Gambetta, et al. Openqasm 3: A broader and deeper quantum assembly language. *ACM Transactions on Quantum Computing*, 3(3):1–50, 2022.

[30] Andrew J. Daley, Martin M. Boyd, Jun Ye, and Peter Zoller. Quantum computing with alkaline-earth-metal atoms. *Phys. Rev. Lett.*, 101:170504, Oct 2008.

[31] Yvette de Sereville. Towards dual-isotope entangling gates for trapped-ion quantum computing. Master's thesis, University of Waterloo, 2022.

[32] Hans Dehmelt. Experiments with an isolated subatomic particle at rest. *Reviews of modern physics*, 62(3):525, 1990.

[33] Hans G Dehmelt. Monoion oscillator as potential ultimate laser frequency standard. *IEEE transactions on instrumentation and measurement*, (2):83–87, 1982.

[34] K Deng, YL Sun, WH Yuan, ZT Xu, J Zhang, ZH Lu, and J Luo. A modified model of helical resonator with predictable loaded resonant frequency and q-factor. *Review of Scientific Instruments*, 85(10):104706, 2014.

[35] L Deslauriers, M Acton, BB Blinov, K-A Brickman, PC Haljan, WK Hensinger, D Hucul, S Katnik, RN Kohn Jr, PJ Lee, et al. Efficient photoionization loading of trapped ions with ultrafast pulses. *Physical Review A*, 74(6):063421, 2006.

[36] David Deutsch. Quantum theory, the church–turing principle and the universal quantum computer. *Proceedings of the Royal Society of London. A. Mathematical and Physical Sciences*, 400(1818):97–117, 1985.

[37] F Diedrich, JC Bergquist, Wayne M Itano, and DJ Wineland. Laser cooling to the zero-point energy of motion. *Physical review letters*, 62(4):403, 1989.

[38] MR Dietrich, N Kurz, T Noel, Gang Shu, and BB Blinov. Hyperfine and optical barium ion qubits. *Physical Review A*, 81(5):052328, 2010.

[39] David P DiVincenzo. The physical implementation of quantum computation. *Fortschritte der Physik: Progress of Physics*, 48(9-11):771–783, 2000.

[40] Samuel Earnshaw. On the nature of the molecular forces which regulate the constitution of the luminiferous ether. *Transactions of the Cambridge Philosophical Society*, 7:97, 1848.

[41] Richard P Feynman et al. Simulating physics with computers. *Int. j. Theor. phys*, 21(6/7), 1982.

[42] Michael Foss-Feig, Stephen Ragole, Andrew Potter, Joan Dreiling, Caroline Figgatt, John Gaebler, Alex Hall, Steven Moses, Juan Pino, Ben Spaun, et al. Entanglement from tensor networks on a trapped-ion quantum computer. *Physical Review Letters*, 128(15):150504, 2022.

[43] Virginia Frey, Richard Rademacher, Elijah Durso-Sabina, Noah Greenberg, Nikolay Videnov, Matthew L Day, Rajibul Islam, and Crystal Senko. A quantum computing programming language for transparent experiment descriptions. In *2021 IEEE*

International Conference on Quantum Computing and Engineering (QCE), pages 244–254. IEEE, 2021.

[44] Daniel Gottesman. Theory of fault-tolerant quantum computation. *Physical Review A*, 57(1):127, 1998.

[45] Noah Greenberg and Crystal Senko. Microgram barium chloride ablation targets for trapped ion experiments. *Manuscript in preparation*, 2023.

[46] Noah Greenberg, Brendan M. White, Pei Jiang Low, and Crystal Senko. Utilizing an autoionizing resonance to trap ba^+. *Manuscript in preparation*, 2023.

[47] Greenberg, Noah. Vacuum and optical designs for an open-access trapped ion quantum processor. Master's thesis, University of Waterloo, 2020.

[48] Lov K Grover. A fast quantum mechanical algorithm for database search. In *Proceedings of the twenty-eighth annual ACM symposium on Theory of computing*, pages 212–219, 1996.

[49] Hartmut Häffner, Christian F Roos, and Rainer Blatt. Quantum computing with trapped ions. *Physics reports*, 469(4):155–203, 2008.

[50] L-W He, CE Burkhardt, M Ciocca, JJ Leventhal, and ST Manson. Absolute cross sections for the photoionization of the 6s6p 1 p excited state of barium. *Physical review letters*, 67(16):2131, 1991.

[51] Jonathan P Home, David Hanneke, John D Jost, Dietrich Leibfried, and David J Wineland. Normal modes of trapped ions in the presence of anharmonic trap potentials. *New Journal of Physics*, 13(7):073026, 2011.

[52] David Hucul, Justin E Christensen, Eric R Hudson, and Wesley C Campbell. Spectroscopy of a synthetic trapped ion qubit. *Physical review letters*, 119(10):100501, 2017.

[53] Ismail V. Inlek. *Multi-species trapped atomic ion modules for quantum networks*. PhD thesis, University of Maryland, College Park, 2016. Copyright - Database copyright ProQuest LLC; ProQuest does not claim copyright in the individual underlying works; Last updated - 2023-03-03.

[54] DFV James. Quantum dynamics of cold trapped ions with application. *Quantum Computation and Quantum Information Theory: Reprint Volume with Introductory*

Notes for ISI TMR Network School, 12-23 July 1999, Villa Gualino, Torino, Italy, 66:345, 2000.

[55] Ali Kalyar and Muhammad Mazhar. *Two-step Laser Excitation Studies of Bound and Autoionizing States in Barium*. PhD thesis, Quaid-i-Azam University Islamabad, Pakistan, 2008.

[56] Grzegorz Kasprowicz, Thomas Harty, Sébastien Bourdeauducq, Robert Jördens, David Allcock, David Nadlinger, Joseph W Britton, Ana Sotirova, and Dorota Nowicka. Urukul: Open-source frequency synthesizer module for quantum physics. *International Journal of Electronics and Telecommunications*, 68, 2022.

[57] Grzegorz Kasprowicz, Paweł Kulik, Michal Gaska, Tomasz Przywozki, Krzysztof Pozniak, Jakub Jarosinski, Joseph W Britton, Thomas Harty, Chris Balance, Weida Zhang, et al. Artiq and sinara: Open software and hardware stacks for quantum physics. In *Quantum 2.0*, pages QTu8B–14. Optica Publishing Group, 2020.

[58] Brian W Kernighan and Dennis M Ritchie. The c programming language. 2002.

[59] D Kielpinski, BE King, CJ Myatt, Cass A Sackett, QA Turchette, Wayne M Itano, Christopher Monroe, David J Wineland, and Wojciech H Zurek. Sympathetic cooling of trapped ions for quantum logic. *Physical Review A*, 61(3):032310, 2000.

[60] David Kielpinski, Chris Monroe, and David J Wineland. Architecture for a large-scale ion-trap quantum computer. *Nature*, 417(6890):709–711, 2002.

[61] Tomasz Kuczerski and Włodzimierz Mikke. Hardware for quantum computations. *Issues of Armament Technology*, 158(3-4):49–63, 2021.

[62] Andrew J Landahl, Daniel S Lobser, Benjamin CA Morrison, Kenneth M Rudinger, Antonio E Russo, Jay W Van Der Wall, and Peter Maunz. Jaqal, the quantum assembly language for qscout. *arXiv preprint arXiv:2003.09382*, 2020.

[63] DJ Larson, James C Bergquist, John J Bollinger, Wayne M Itano, and David J Wineland. Sympathetic cooling of trapped ions: A laser-cooled two-species nonneutral ion plasma. *Physical review letters*, 57(1):70, 1986.

[64] Regina Lechner, Christine Maier, Cornelius Hempel, Petar Jurcevic, Ben P Lanyon, Thomas Monz, Michael Brownnutt, Rainer Blatt, and Christian F Roos. Electromagnetically-induced-transparency ground-state cooling of long ion strings. *Physical Review A*, 93(5):053401, 2016.

[65] Dietrich Leibfried, Rainer Blatt, Christopher Monroe, and David Wineland. Quantum dynamics of single trapped ions. *Reviews of Modern Physics*, 75(1):281, 2003.

[66] Günther Leschhorn, T Hasegawa, and T Schaetz. Efficient photo-ionization for barium ion trapping using a dipole-allowed resonant two-photon transition. *Applied Physics B*, 108:159–165, 2012.

[67] G-D Lin, S-L Zhu, Rajibul Islam, Kihwan Kim, M-S Chang, Simcha Korenblit, Christopher Monroe, and L-M Duan. Large-scale quantum computation in an anharmonic linear ion trap. *Europhysics Letters*, 86(6):60004, 2009.

[68] Wei Liu, Shu-Ming Chen, Ping-Xing Chen, and Wei Wu. Design optimization for anharmonic linear surface-electrode ion trap. *Chinese Physics Letters*, 31(11):113701, 2014.

[69] Seth Lloyd. Universal quantum simulators. *Science*, 273(5278):1073–1078, 1996.

[70] Daniel Lobser, Joshua Goldberg, Andrew J Landahl, Peter Maunz, Benjamin CA Morrison, Kenneth Rudinger, Antonio Russo, Brandon Ruzic, Daniel Stick, Jay Van Der Wall, et al. Jaqalpaw: A guide to defining pulses and waveforms for jaqal. *arXiv preprint arXiv:2305.02311*, 2023.

[71] Pei Jiang Low. Tolerable experimental imperfections for a quadrupole blade ion trap and practical qudit gates with trapped ions. Master's thesis, University of Waterloo, 2019.

[72] WW Macalpine and RO Schildknecht. Coaxial resonators with helical inner conductor. *Proceedings of the IRE*, 47(12):2099–2105, 1959.

[73] Yuri Manin. Computable and uncomputable. *Sovetskoye Radio, Moscow*, 128:28, 1980.

[74] Irene Marzoli, JI Cirac, R Blatt, and P Zoller. Laser cooling of trapped three-level ions: Designing two-level systems for sideband cooling. *Physical Review A*, 49(4):2771, 1994.

[75] Peter Lukas Wilhelm Maunz. High optical access trap 2.0. Technical report, Sandia National Lab.(SNL-NM), Albuquerque, NM (United States), 2016.

[76] David Lynn Moehring, Clark Highstrete, D Stick, Kevin Michael Fortier, R Haltli, C Tigges, and Matthew Glenn Blain. Design, fabrication and experimental demonstration of junction surface ion traps. *New Journal of Physics*, 13(7):075018, 2011.

[77] Klaus Mølmer and Anders Sørensen. Multiparticle entanglement of hot trapped ions. *Physical Review Letters*, 82(9):1835, 1999.

[78] Ch Monroe, DM Meekhof, BE King, Steven R Jefferts, Wayne M Itano, David J Wineland, and P Gould. Resolved-sideband raman cooling of a bound atom to the 3d zero-point energy. *Physical review letters*, 75(22):4011, 1995.

[79] Chris Monroe, David M Meekhof, Barry E King, Wayne M Itano, and David J Wineland. Demonstration of a fundamental quantum logic gate. *Physical review letters*, 75(25):4714, 1995.

[80] Christopher Monroe, Wes C Campbell, L-M Duan, Z-X Gong, Alexey V Gorshkov, Paul W Hess, Rajibul Islam, Kihwan Kim, Norbert M Linke, Guido Pagano, et al. Programmable quantum simulations of spin systems with trapped ions. *Reviews of Modern Physics*, 93(2):025001, 2021.

[81] Christopher Monroe, Robert Raussendorf, Alex Ruthven, Kenneth R Brown, Peter Maunz, L-M Duan, and Jungsang Kim. Large-scale modular quantum-computer architecture with atomic memory and photonic interconnects. *Physical Review A*, 89(2):022317, 2014.

[82] Benjamin CA Morrison, Andrew J Landahl, Daniel S Lobser, Kenneth M Rudinger, Antonio E Russo, Jay W Van Der Wall, and Peter Maunz. Just another quantum assembly language (jaqal). In *2020 IEEE International Conference on Quantum Computing and Engineering (QCE)*, pages 402–408. IEEE, 2020.

[83] W Neuhauser, M Hohenstatt, P Toschek, and H Dehmelt. Optical-sideband cooling of visible atom cloud confined in parabolic well. *Physical Review Letters*, 41(4):233, 1978.

[84] Michael A Nielsen and Isaac L Chuang. *Quantum computation and quantum information*. Cambridge university press, 2010.

[85] Steven Olmschenk, DN Matsukevich, P Maunz, D Hayes, L-M Duan, and C Monroe. Quantum teleportation between distant matter qubits. *Science*, 323(5913):486–489, 2009.

[86] M Palmero, S Martínez-Garaot, UG Poschinger, A Ruschhaupt, and JG Muga. Fast separation of two trapped ions. *New Journal of Physics*, 17(9):093031, 2015.

[87] Wolfgang Paul. Electromagnetic traps for charged and neutral particles. *Reviews of modern physics*, 62(3):531, 1990.

[88] Juan M Pino, Jennifer M Dreiling, Caroline Figgatt, John P Gaebler, Steven A Moses, MS Allman, CH Baldwin, M Foss-Feig, D Hayes, K Mayer, et al. Demonstration of the trapped-ion quantum ccd computer architecture. *Nature*, 592(7853):209–213, 2021.

[89] Ivan Pogorelov, Thomas Feldker, Ch D Marciniak, Lukas Postler, Georg Jacob, Oliver Krieglsteiner, Verena Podlesnic, Michael Meth, Vlad Negnevitsky, Martin Stadler, et al. Compact ion-trap quantum computing demonstrator. *PRX Quantum*, 2(2):020343, 2021.

[90] John Preskill. Fault-tolerant quantum computation. In *Introduction to quantum computation and information*, pages 213–269. World Scientific, 1998.

[91] Rademacher, Richard. Design of a real-time embedded control system for quantum computing experiments. Master's thesis, University of Waterloo, 2020.

[92] MG Raizen, JM Gilligan, James C Bergquist, Wayne M Itano, and David J Wineland. Ionic crystals in a linear paul trap. *Physical Review A*, 45(9):6493, 1992.

[93] Melissa C Revelle. Phoenix and peregrine ion traps. *arXiv preprint arXiv:2009.02398*, 2020.

[94] Leon Riesebos, Brad Bondurant, Jacob Whitlow, Junki Kim, Mark Kuzyk, Tianyi Chen, Samuel Phiri, Ye Wang, Chao Fang, Andrew Van Horn, et al. Modular software for real-time quantum control systems. In *2022 IEEE International Conference on Quantum Computing and Engineering (QCE)*, pages 545–555. IEEE, 2022.

[95] Leon Riesebos and Kenneth R Brown. Functional simulation of real-time quantum control software. In *2022 IEEE International Conference on Quantum Computing and Engineering (QCE)*, pages 535–544. IEEE, 2022.

[96] Leon Riesebos, Xiang Fu, Ahmed A Moueddenne, Lingling Lao, Savvas Varsamopoulos, Imran Ashraf, J Van Someren, Nader Khammassi, Carmen G Almudever, and Koen Bertels. Quantum accelerated computer architectures. In *2019 IEEE International Symposium on Circuits and Systems (ISCAS)*, pages 1–4. IEEE, 2019.

[97] Andrew Russ Risinger. *Engineering a Control System for a Logical Qubit-Scale Trapped Ion Quantum Computer*. PhD thesis, University of Maryland, College Park, 2023.

[98] Daniel Rotter. *Quantum feedback and quantum correlation measurements with a single Barium ion.* na, 2008.

[99] J. A. Rushton, M. Aldous, and M. D. Himsworth. Contributed Review: The feasibility of a fully miniaturized magneto-optical trap for portable ultracold quantum technology. *Review of Scientific Instruments*, 85(12):121501, 12 2014.

[100] JD Sankey and AA Madej. The production of ions for single-ion traps. *Applied Physics B*, 49:69–72, 1989.

[101] Peter DD Schwindt, Yuan-Yu Jau, Heather Partner, Adrian Casias, Adrian R Wagner, Matthew Moorman, Ronald P Manginell, James R Kellogg, and John D Prestage. A highly miniaturized vacuum package for a trapped ion atomic clock. *Review of Scientific instruments*, 87(5), 2016.

[102] Signe Seidelin, John Chiaverini, Rainer Reichle, John J Bollinger, Didi Leibfried, Joe Britton, JH Wesenberg, RB Blakestad, RJ Epstein, DB Hume, et al. Microfabricated surface-electrode ion trap for scalable quantum information processing. *Physical review letters*, 96(25):253003, 2006.

[103] X Shi, SL Todaro, GL Mintzer, CD Bruzewicz, J Chiaverini, and IL Chuang. Ablation loading of barium ions into a surface electrode trap. *arXiv preprint arXiv:2303.02143*, 2023.

[104] Peter W Shor. Algorithms for quantum computation: discrete logarithms and factoring. In *Proceedings 35th annual symposium on foundations of computer science*, pages 124–134. Ieee, 1994.

[105] Peter W Shor. Fault-tolerant quantum computation. In *Proceedings of 37th conference on foundations of computer science*, pages 56–65. IEEE, 1996.

[106] James D Siverns and Qudsia Quraishi. Ion trap architectures and new directions. *Quantum Information Processing*, 16:1–42, 2017.

[107] JD Siverns, LR Simkins, Seb Weidt, and WK Hensinger. On the application of radio frequency voltages to ion traps via helical resonators. *Applied Physics B*, 107:921–934, 2012.

[108] Anders Sørensen and Klaus Mølmer. Quantum computation with ions in thermal motion. *Physical review letters*, 82(9):1971, 1999.

[109] Anders Sørensen and Klaus Mølmer. Entanglement and quantum computation with ions in thermal motion. *Physical Review A*, 62(2):022311, 2000.

[110] A Steane. The ion trap quantum information processor. *Applied Physics B: Lasers & Optics*, 64(6), 1997.

[111] Andrew Steane. Quantum computing. *Reports on Progress in Physics*, 61(2):117, 1998.

[112] Andrew M Steane. Efficient fault-tolerant quantum computing. *Nature*, 399(6732):124–126, 1999.

[113] Andrew M Steane and David M Lucas. Quantum computing with trapped ions, atoms and light. *Fortschritte der Physik: Progress of Physics*, 48(9-11):839–858, 2000.

[114] Daniel Lynn Stick. Fabrication and characterization of semiconductor ion traps for quantum information processing. *Ph. D. Thesis*, 2007.

[115] John E Stone, David Gohara, and Guochun Shi. Opencl: A parallel programming standard for heterogeneous computing systems. *Computing in science & engineering*, 12(3):66, 2010.

[116] Bjarne Stroustrup. An overview of c++. In *Proceedings of the 1986 SIGPLAN workshop on Object-oriented programming*, pages 7–18, 1986.

[117] QA Turchette, CS Wood, BE King, CJ Myatt, D Leibfried, WM Itano, C Monroe, and DJ Wineland. Deterministic entanglement of two trapped ions. *Physical Review Letters*, 81(17):3631, 1998.

[118] Usb 3.2 revision 1.1 - june 2022. Standard, USB 3.0 Promoter Group, Jun 2022.

[119] Guido Van Rossum, Fred L Drake, et al. *Python reference manual*, volume 111. Centrum voor Wiskunde en Informatica Amsterdam, 1995.

[120] Videnov, Nikolay. Optical design for an open access trapped ion quantum processor. Master's thesis, University of Waterloo, 2021.

[121] Andreas Walther, Frank Ziesel, Thomas Ruster, Sam T Dawkins, Konstantin Ott, Max Hettrich, Kilian Singer, Ferdinand Schmidt-Kaler, and Ulrich Poschinger. Controlling fast transport of cold trapped ions. *Physical review letters*, 109(8):080501, 2012.

[122] Yong Wan, Daniel Kienzler, Stephen D Erickson, Karl H Mayer, Ting Rei Tan, Jenny J Wu, Hilma M Vasconcelos, Scott Glancy, Emanuel Knill, David J Wineland, et al. Quantum gate teleportation between separated qubits in a trapped-ion processor. *Science*, 364(6443):875–878, 2019.

[123] Brendan M White, Pei Jiang Low, Yvette de Sereville, Matthew L Day, Noah Greenberg, Richard Rademacher, and Crystal Senko. Isotope-selective laser ablation ion-trap loading of ba+ 137 using a bacl 2 target. *Physical Review A*, 105(3):033102, 2022.

[124] B Willke and M Kock. Measurement of photoionization cross sections from the laser-excited ba i (6s6p) 1p10 state. *Journal of Physics B: Atomic, Molecular and Optical Physics*, 26(6):1129, 1993.

[125] Daniel J Wineland, Christoper Monroe, Wayne M Itano, BE King, Dietrich Leibfried, DM Meekhof, C Myatt, and Chris Wood. Experimental primer on the trapped ion quantum computer. *Fortschritte der Physik: Progress of Physics*, 46(4-5):363–390, 1998.

[126] David J Wineland, Robert E Drullinger, and Fred L Walls. Radiation-pressure cooling of bound resonant absorbers. *Physical Review Letters*, 40(25):1639, 1978.

[127] David J Wineland, C Monroe, Wayne M Itano, BE King, Dietrich Leibfried, C Myatt, and Chris Wood. Trapped-ion quantum simulator. *Physica Scripta*, 1998(T76):147, 1998.

[128] Jannes B Wübbena, Sana Amairi, Olaf Mandel, and Piet O Schmidt. Sympathetic cooling of mixed-species two-ion crystals for precision spectroscopy. *Physical Review A*, 85(4):043412, 2012.

[129] Dahyun Yum, Debashis De Munshi, Tarun Dutta, and Manas Mukherjee. Optical barium ion qubit. *JOSA B*, 34(8):1632–1636, 2017.

APPENDICES

Appendix A

Atomic Physics Symbols

Chemical Symbols

Elements, ions, and molecules are represented in the form

$$ {}^{A}_{Z}Ee^{C\pm}_{N} $$

where

- A is the atomic mass number representing the total number of *nucleons* in the isotope nucleus (protons and neutrons).
- Z is the atomic number representing the total number of *protons* in the isotope nucleus.
- Ee is a unique one- or two-letter identifier for the element.
- $C\pm$ is the net charge of the particle.
- N is the number of atoms of that element in a molecule.

Z is often omitted because each element has a constant number of protons, so the same information is represented by the letter identifier. A therefore represents the specific isotope of the element with differing numbers of neutrons. C indicates the difference between the number of protons and neutrons in the element. It is omitted in the case of neutral atoms/molecules and in the case of single ionization, only the $\pm$ symbol is shown. N is omitted in the case that $N = 1$. Molecules may consist of multiple elements and/or multiple atoms of the same element.

Term Symbols

The energy levels of electrons in atoms and ions are represented in terms of their angular momenta in the form

$$^{2S+1}L_J$$

where

- S is the total spin quantum number
- L is the total orbital quantum number
- J is the total angular momentum quantum number

Additionally, for isotopes with nuclear spin $I > 0$

- I is the nuclear spin
- F is the total atomic spin

In this thesis, all term symbols refer to a single valence electron. Additional quantum numbers are thus irrelevant and omitted.

Appendix B

Electronic Energy Levels

The energy levels of electrons bound in atoms and ions have many sublevels arising from interactions between the particles that constitute the atoms. The *principle energy level* n describes the orbital in which the electron resides. *Fine structure* is the splitting of otherwise degenerate principle energy level states with non-zero angular momentum into two states due to interaction between the spin and angular momentum of the electron. *Hyperfine structure* is the further splitting of energy levels into degenerate states that results from interaction between the electron spin and nuclear spin. The degenerate hyperfine states can be separated into distinct energies by the application of an external magnetic field. The observed energy splitting is known as the *Zeeman effect*.

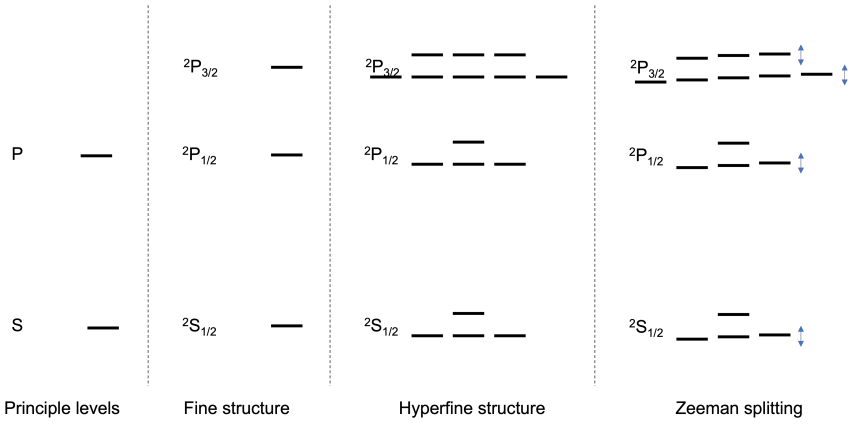

Figure B.1: Diagram illustrating different degrees of structure in the energy levels of an electron bound to an atom. The differences in energy levels get smaller from left to right.

Appendix C

Helmholtz Coils

Helmholtz coils consist of two identical coils of electrically conducting wire radially parallel to each other and axially aligned. Current of the same magnitude and direction flows through the coils, generating a uniform magnetic field at the midpoint between the coils along the coil axis (Figure C.1).

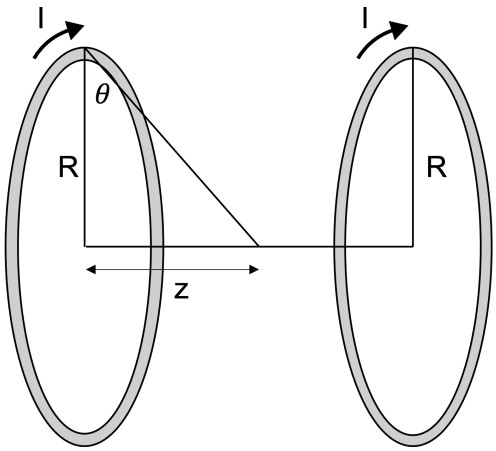

Figure C.1: Diagram of Helmholtz coils. The magnetic field generated between the coils along the center of the coil axis is uniform and simple to calculate.

The magnetic field given by current flowing through a wire is given by the Biot-Savart Law:

$$\mathbf{B}(\mathbf{r}) = \frac{\mu_0}{4\pi} \int_C \frac{Id\ell \times \mathbf{r}'}{|\mathbf{r}'|^3} \tag{C.1}$$

where $\mathbf{r}$ is the distance from the current, I is the current, C is the path over which the line integral is evaluated, $d\mathbf{l}$ is a path vector along C, $\mathbf{r}' = \mathbf{r} - \ell$ is the displacement vector from the wire, and μ_0 is the magnetic permeability of the vacuum. For the case of the magnetic field measured axially from the center of a single circular loop of constant current, the radial magnetic field components cancel out and the axial magnetic field field is

$$B(z) = \frac{\mu_0}{4\pi} I \int_C \frac{d\ell}{|r|^2} \tag{C.2}$$

where z is the axial distance from the center of the loop and θ is the angle between the plane of the loop and the vector pointing from the loop to the position at which the magnetic field is measured. When integrated over a single circular loop of wire, the Biot-Savart Law in this formulation is evaluated to

$$\begin{aligned} B(z) &= \frac{\mu_0 I R^2}{2(z^2 + R^2)^{3/2}} = \zeta(z) \frac{\mu_0 I}{2R} \\ \zeta(z) &= \left(1 + \frac{z^2}{R^2}\right)^{-3/2} \end{aligned} \tag{C.3}$$

where R is the radius of the loop. For a wire coil with n loops, the magnetic field increases linearly with the number of loops:

$$B(z) = \zeta(z) \frac{\mu_0 n I}{2R} \tag{C.4}$$

Thus, the magnetic field at the midpoint of two coils is

$$B(z) = \frac{\mu_0 n I}{2R} (\zeta(z) + \zeta(-z)) \tag{C.5}$$

In the case that the Helmholtz coils are separated exactly by a distance equal to the radius of the coils ($z = \pm R$), Equation C.5 evaluates via Taylor expansion to exactly

$$B = \left(\frac{4}{5}\right)^{3/2} \frac{\mu_0 n I}{R} \tag{C.6}$$

In the QuantumIon apparatus, this condition does not necessarily hold and the magnetic field must be calculated using Equation C.5.

This derivation implicitly assumes that all n coils occupy the same physical space. It holds near enough to true for well-wound coils that are neither too long nor too thick. It is sufficiently accurate for design purposes. The model may be enhanced by integrating over the length and thickness of a coil.

Appendix D

Modulators

Acousto-Optic Modulators

An AOM is composed of a transparent crystal with a transducer attached. When the transducer receives an RF signal, it vibrates the crystal, creating local fluctuations in the index of refraction of the crystal that acts as a diffraction grating rapidly propagating through the crystal [21] (Figure D.1). Light that interacts with the driven AOM is diffracted with a shift in the frequency, phase, and amplitude of the light at an angle according to

$$2\Lambda \sin\theta = m\lambda \tag{D.1}$$

where Λ is the wavelength of the sound wave in the crystal from the transducer, θ is the diffraction angle, m is the diffraction order of the emitted light, and λ is wavelength of light. The light diffracted by the AOM is modulated in frequency by

$$\omega_{out} = \omega_{in} + 2\pi m f \tag{D.2}$$

where $m \in \mathbb{Z}$ is the diffraction order of the emitted light and f is the frequency of the RF signal driving the AOM. Therefore, the angular frequency of the sound wave produced by the transducer in the crystal is $\Omega = 2\pi f$. The phase and intensity of the diffracted light are proportional to the phase and power of the driving RF signal, respectively.

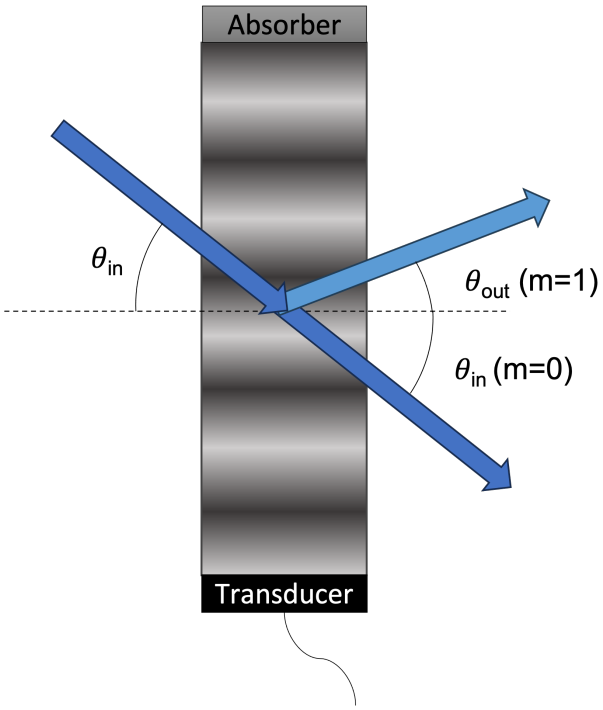

Figure D.1: Diagram of an AOM device and its behavior. When driven by an RF signal, the AOM crystal vibrates and diffracts light. The diffracted light is frequency-shifted relative to the input light by the RF drive signal.

Electro-Optic Modulators

In an EOM, an input RF signal modulates the electric field across a crystal material that exhibits an electro-optic effect, modifying the absorption and/or index of refraction of the material [21]. The frequencies of the sidebands emitted by the EOM are given by Equation D.2 where m is the harmonic order. The intensity of the sidebands are calculated with Bessel functions and the EOM is typically driven in the regime where the first order ($m = 1$) sidebands are have significant intensity and the higher order sidebands ($m \geq 2$) are negligible. The incident light is also transmitted without modulation.

Appendix E

Electrical Schematics

Select schematics for a subset of the electrical circuits that received the most focus in this thesis are shown here.

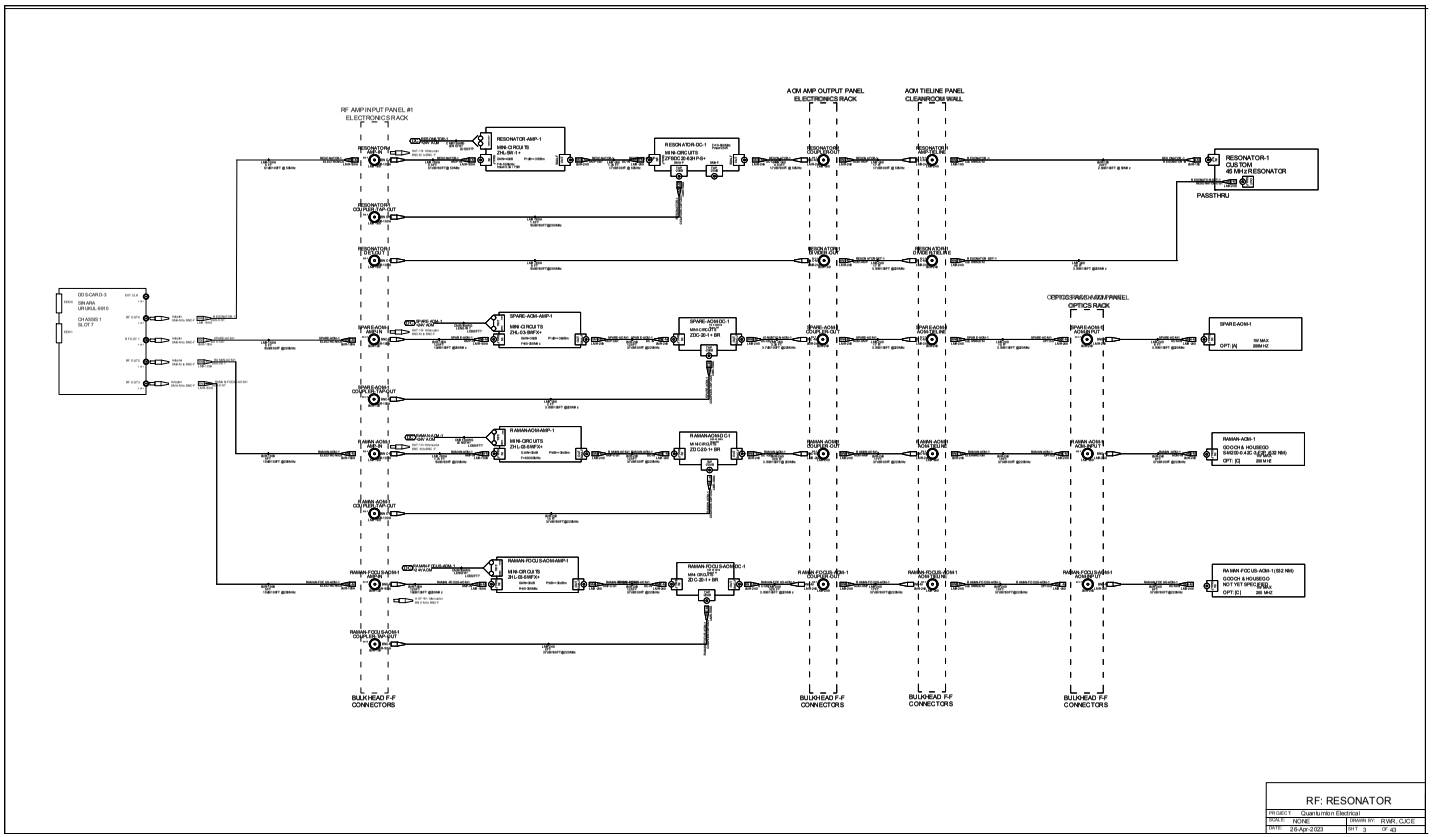

Figure E.1: Electrical schematics for the trap RF drive circuit. Extra AOM RF drive channels are also shown.

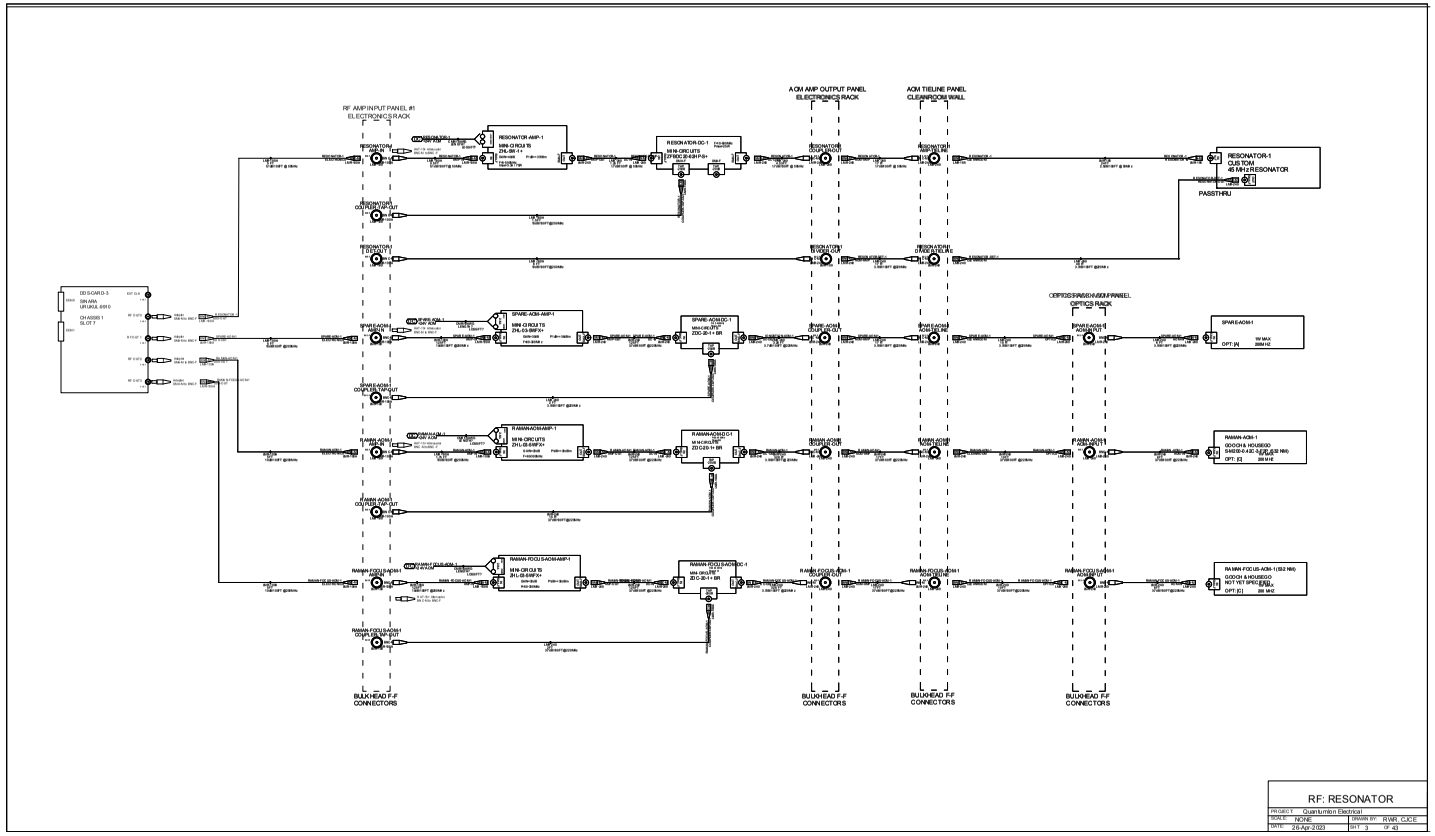

Figure E.2: Electrical schematics for trap DC voltage circuits.

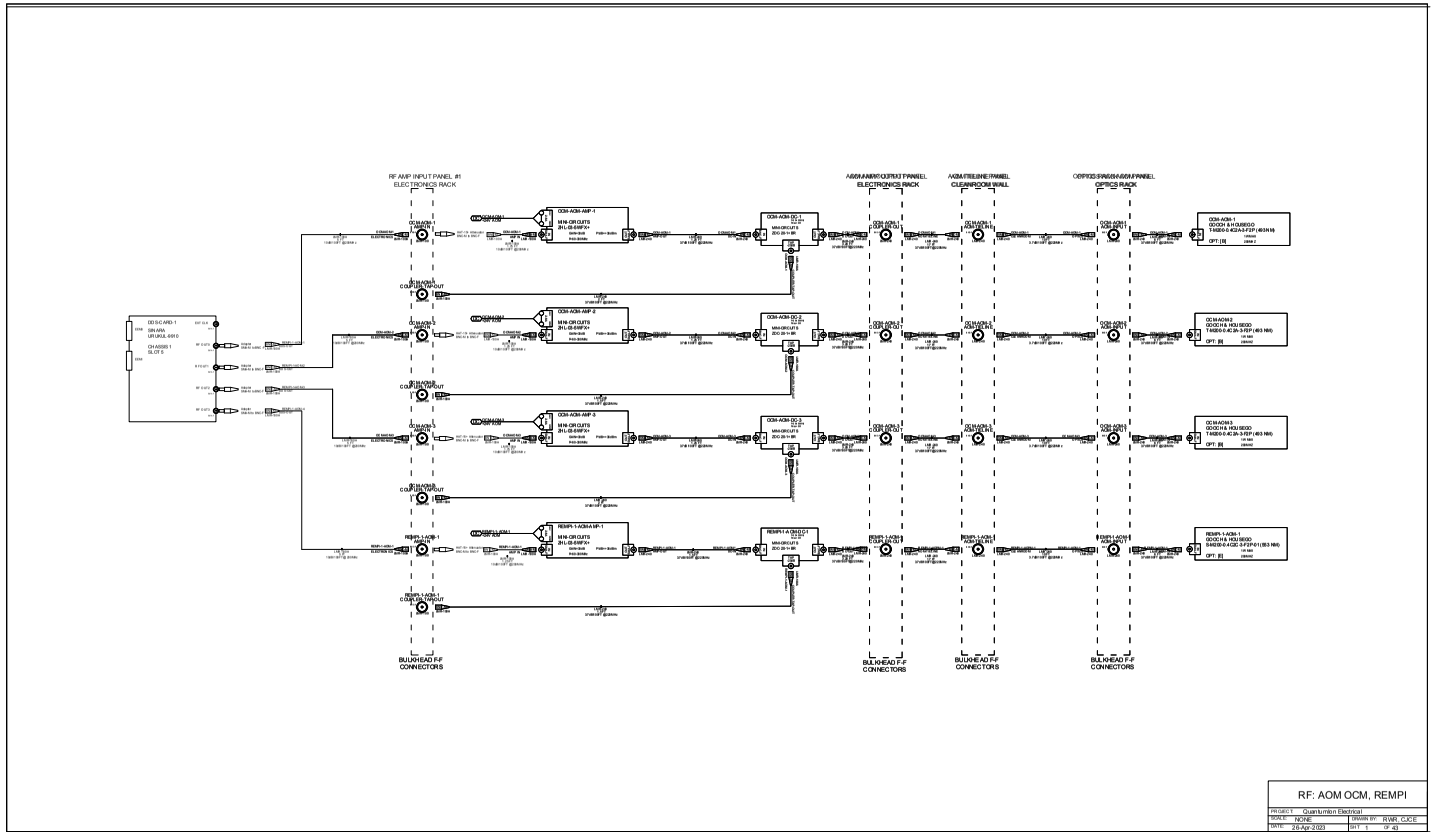

Figure E.3: Electrical schematics for AOM RF drive circuits for the 493 nm and 553 nm lasers.

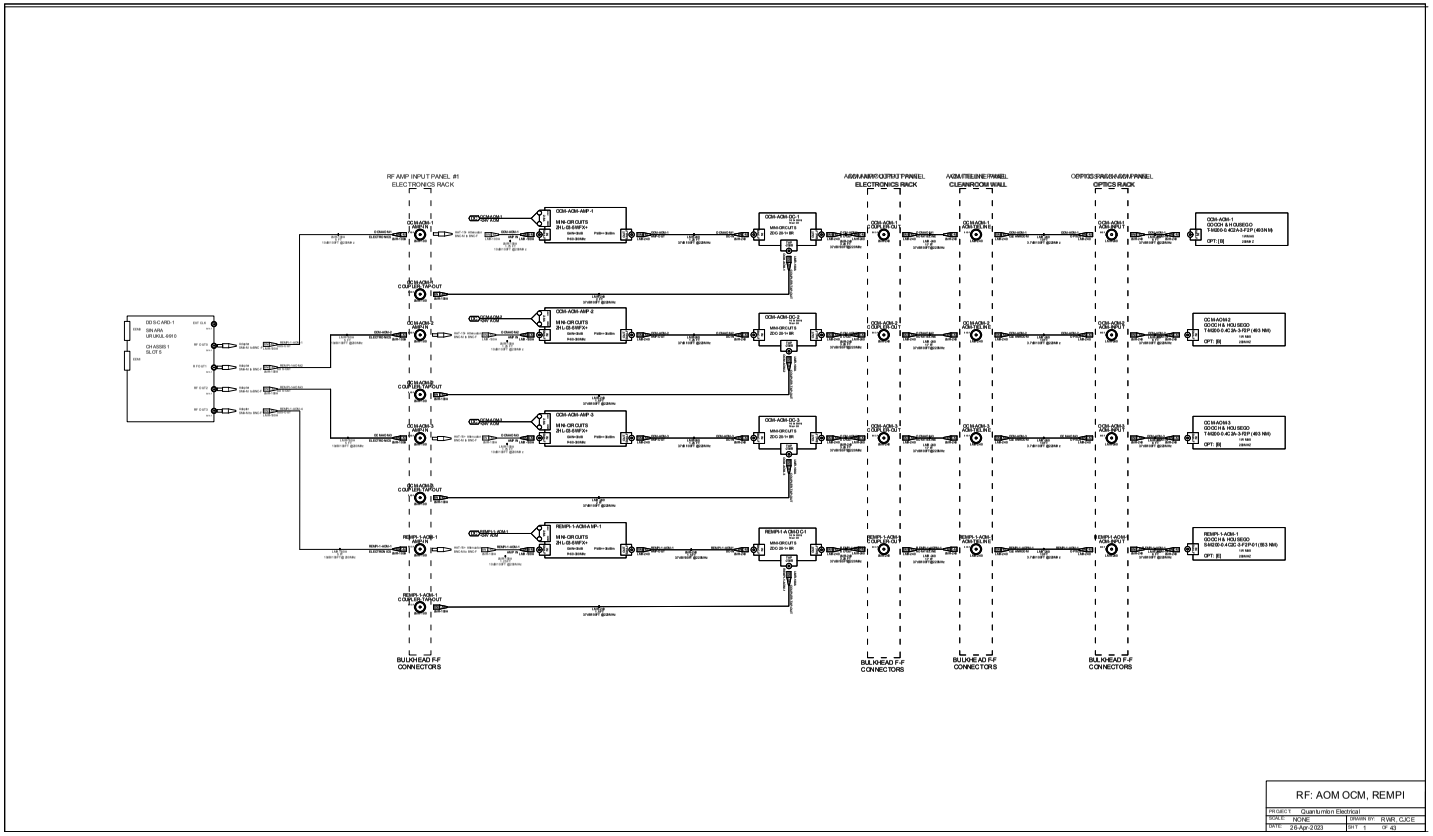

Figure E.4: Electrical schematics for AOM RF drive circuit for the 650 nm and 614 nm lasers.

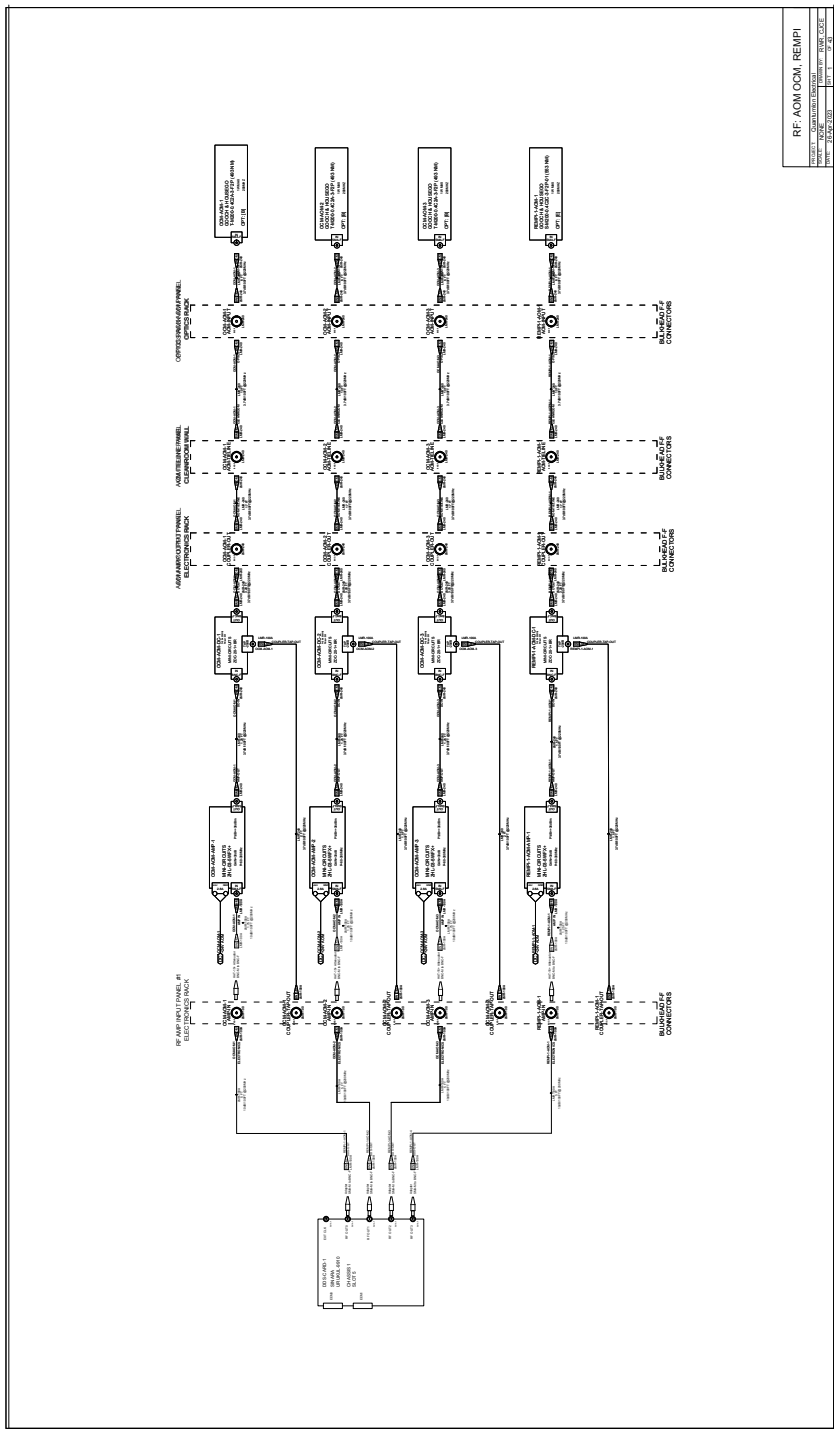

Figure E.5: Electrical schematics for the EOM RF drive circuits.

Appendix F

Printed Circuit Board Schematics

Select schematics for a subset of the PCBs that received the most focus in this thesis are shown here.

Connector Pinouts

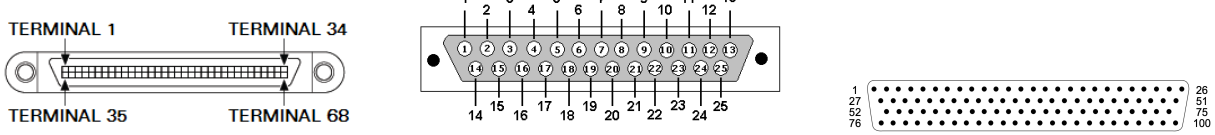

(a) HD68 connector pinout. (b) DB25 connector pinout. (c) DD100 connector pinout.

Figure F.1: Pinout diagrams for the connectors used in circuits that deliver DC voltages to the trap electrodes.

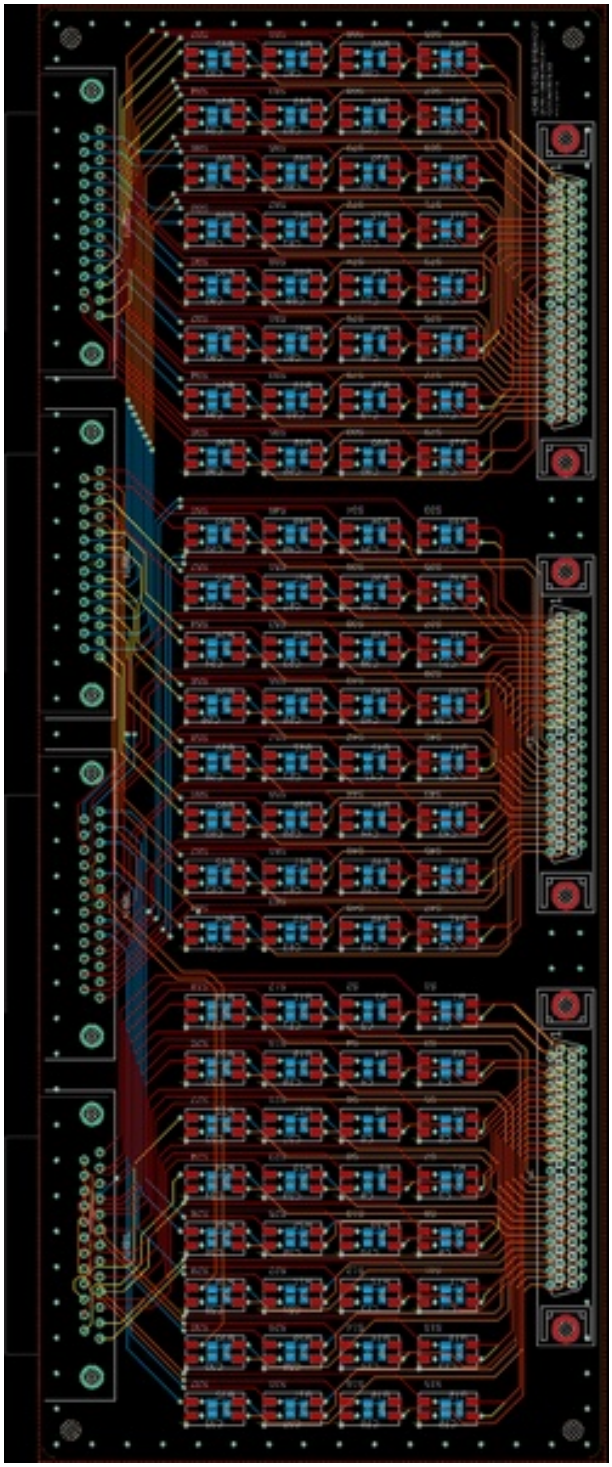

Figure F.2: Schematic of the initial version of the *HD68_TO_DB25_BREAKOUT* PCB.

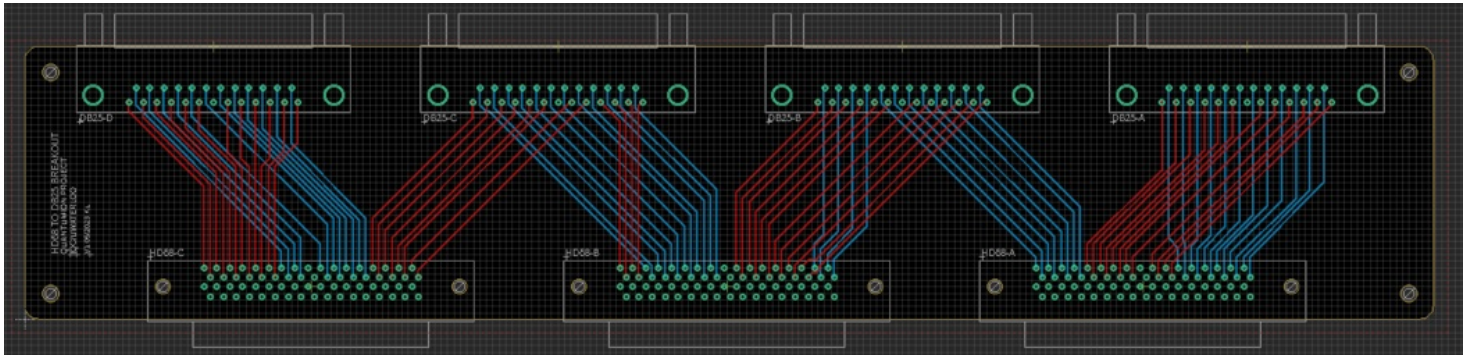

Figure F.3: Schematic of the newer version of the *HD68_TO_DB25_BREAKOUT* PCB. It will replace v1 in the apparatus.

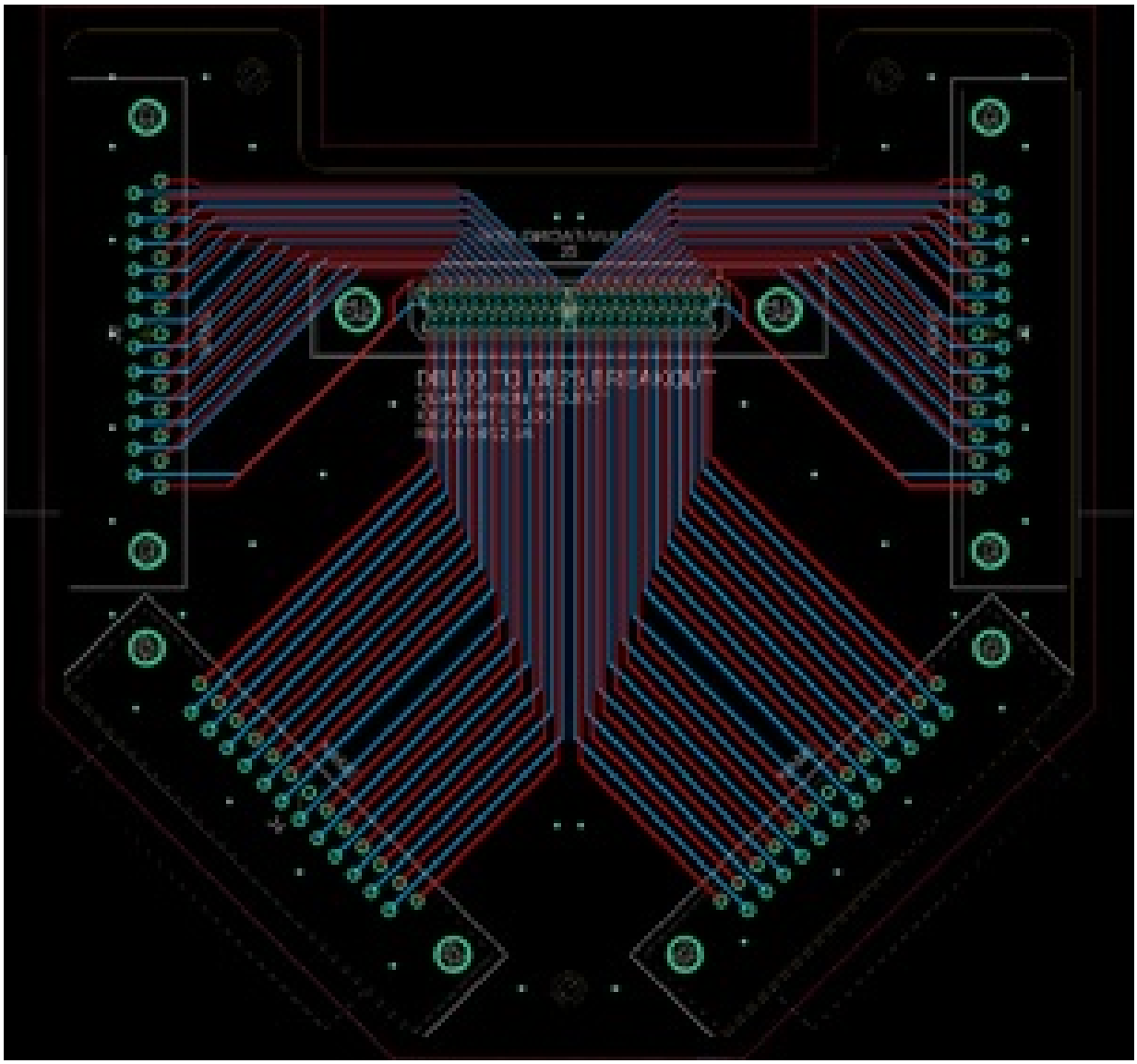

Figure F.4: Schematic of the initial version of the *DD100_TO_DB25_BREAKOUT* PCB.

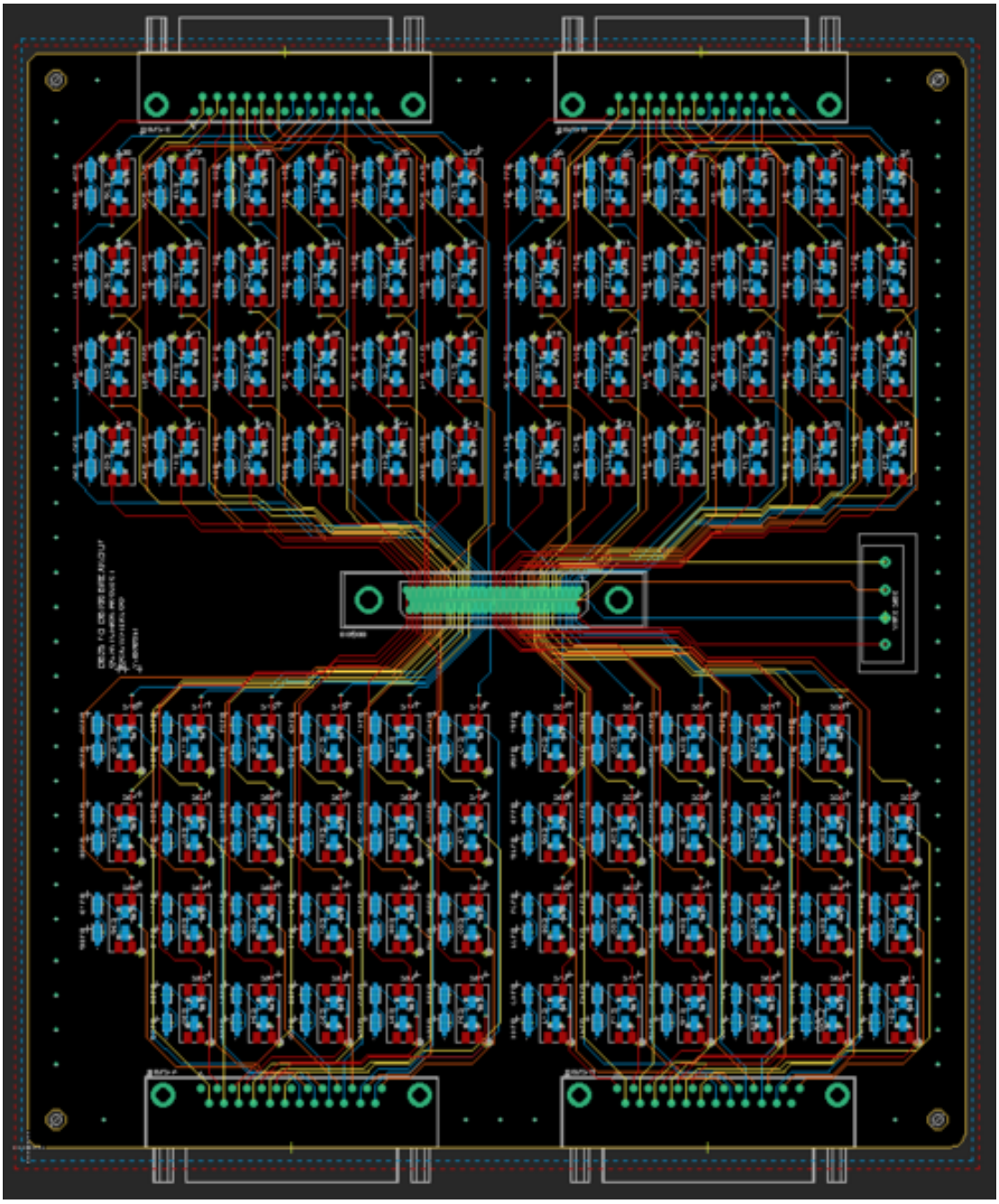

Figure F.5: Schematic of the newer version of the *DD100_TO_DB25_BREAKOUT* PCB. It will replace v1 in the apparatus.

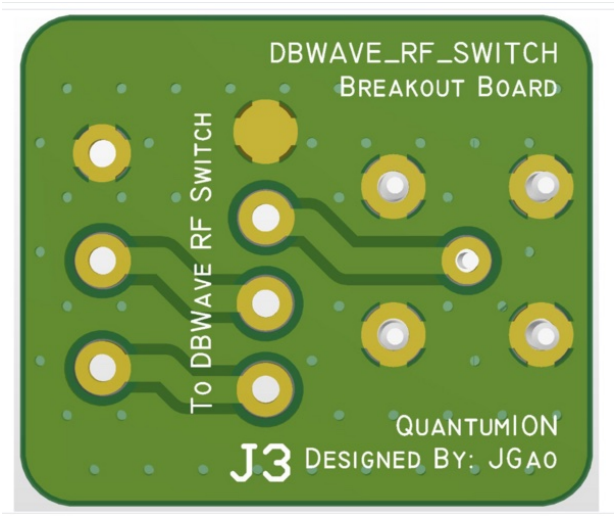

Figure F.6: Schematic of the *DBWAVE_RF_SWITCH_BREAKOUT* PCB.

Appendix G

Radio Frequency Electronics

Power Calculations

The decibel (dB) is a logarithmic scale unit that represents relative differences in power. Power measurements in this thesis are reported in decibel-milliwatt (dBm) units. It is an absolute power unit that indicates that the power is expressed in dB referenced to one milliwatt (1 mW). The benefit of this system is that it allows simple calculations of large differences of power through linear addition. For example, 10 dBm + 5 dB = 15 dBm

The conversion between between P in dBm and W in mW is

$$P = 10 \log_{10} W \tag{G.1}$$

$$W = 10^{P/10} \tag{G.2}$$

RF Connectors

RF connectors are appropriate for different frequency ranges. The typical frequency ranges permitted for the RF connectors discussed in this thesis are summarized in Table G.1.

Connector	**Frequency Range (GHz)**
BNC	$0 - 4$
SMA	$0 - 18$
N-type	$0 - 11$

Table G.1: Summary of the supported frequency ranges for RF connectors. An advantage of the N-type and BNC connectors is that they are more mechanically stable.